UNIVERSIDAD NACIONAL AUTONOMA DE MEXICO

Unidad Académica de los Ciclos Profesional y Posgrado del
Colegio de Ciencias y Humanidades
Instituto de Geofísica
Posgrado en Geofísica

SISMICIDAD Y ESTRUCTURA DE LA ZONA DE SUBDUCCION DE KAMCHATKA

TESIS
PARA OPTAR AL GRADO DE DOCTOR EN GEOFISICA
(SISMOLOGIA Y FISICA DEL INTERIOR DE LA TIERRA)

PRESENTA

ALEXEI VLADIMIROVICH GORBATOV

Ciudad Universitaria **Mayo, 1997.**

INDICE

Seismicity and structure of the Kamchatka subduction zone

Abstract

Kamchatka subduction zone (KSZ) was studied using the seismic data registered by regional and teleseismic networks. The configuration of the Wadati-Benioff seismic zone, its velocity structure, stress distribution in the descending plate, and relation between volcanic activity and subduction process, were investigated in the present work.

Only events presented in a catalog of the Kamchatka Regional Seismic Network (KRSN) from 1964 to 1990 M_W>3.8 with a formal error of hypocentral determination less than 10 km were utilized in the analysis. Moreover, 12 focal mechanism solutions estimated from P-wave first motions, the 21 formal inversions of long-period waveforms, and 11 centroid moment tensor solutions were used in order to determine the stress distribution in the KSZ.

To the south of ~55°N, the slab shows an approximately constant dip angle of ~55°. To the north of ~55°N, the dip of the slab becomes shallower reaching ~35°. The focal mechanism solutions and earthquake hypocentral distribution reveal the presence of the double-planned seismic zone in the area between ~50°N to ~55°N that probably extends to ~56°N. The maximum depth of the double seismic zone is 170-180 km. The two planes of seismicity are separated by 40 km at a depth of 50 km, and by 10-15 km at 180 km depth. The focal mechanism solutions of shallow earthquakes show an abrupt change from the thrust events to down-dip compressional events at approximately 60 km depth at the upper boundary of the descending slab. Within the descending slab, the earthquakes with down-dip tensional axis form the lower plane of the double-planed deep seismic zone. Several earthquakes with down-dip tensional axis are discovered in a narrow area of the upper seismic zone at the depth of about 50 km. The maximum depth of seismicity, D_m, varies from ~500 km depth near 50°N to ~300 km depth at ~55°N. The volcanic front is almost linear along the main part of the KSZ whereas it is sharply shifted landward to the north of ~55°N. The variation of D_m is apparently consistent with the standard empirical relation $D_m = f(\varphi)$, where φ is the thermal parameter of the subducted slab. To the north of ~55°N, the slab is shifted to the northwest and it is sharply deformed in a narrow contorted zone which is ~30 km wide (~56°N, ~161°E). To the north of this contortion zone, D_m decreases up to ~100 km. The landward shift of the northern part of the slab conformes a deviation of the volcanic front to the northwest which follows the ~90-160 km isodepth range of the subducted slab. The observed value of D_m in the northern segment significantly diverges from the global relation $D_m = f(\varphi)$. We interpret this as an effective decrease of the thermal thickness of the subducted lithosphere.

Apparent correlation between the location of the volcanic front and the configuration of the subducted slab may be disclosed by a study of velocity structure of the KSZ. A total of 5270 shallow and intermediate-depth earthquakes registered by the 32 stations of the KRSN were used to assess the P-wave velocity structure beneath the Kamchatka peninsula in the western Pacific. The tomographic inversion was carried out in three steps. First, a one-dimensional (1D) tomographic problem was solved in order to obtain an initial velocity model. Based on that 1D velocity model, 3D tomographic inversions with homogeneous and heterogeneous starting models were obtained. The Conrad (15 km depth) and the Moho (35 km depth) discontinuities determined from 1D tomographic inversion, and the upper boundary of the subducting slab are taken into account in the heterogeneous starting model for the travel times and ray path determinations. Both, the velocity structure and the hypocentral locations are determined simultaneously in the inversion. The spacing of the grid nodes is one half of a degree in the horizontal direction and 20 to 50 km in depth. A detailed P-wave tomographic image was determined down to a depth of 200 km. The resulting tomographic image presents a prominent low-velocity anomaly that shows a maximum decrease in P-wave velocity of ~6% at 30 km depth beneath the chain of active volcanoes. At depth, low-velocity anomalies are also observed in the mantle wedge extending down to a depth of ~150 km. These anomalies apparently are associated with the volcanic activity. The sedimentary basin of the Central Kamchatsky graben, to the west of the volcanic front, and the accretionary prism at the trench correlate with shallow, low-velocity anomalies. High-velocity anomalies observed at a depth of 10 km may be associated with the location of metamorphic basements in the Ganalsky-Valaginskoe uplift and upper crust of Shipunsky cape. The results also suggest that the subducted Pacific plate has P-wave velocities ~2-7% higher than that of the surrounding mantle and a thickness of ~70 km.

RESUMEN

La zona de subducción de la península de Kamchatka (ZSK) fue estudiada usando los sismos registrados por redes sísmicas regionales y telesísmicas. En este trabajo se determinó la configuración de la zona Wadati-Benioff, la relación entre el volcanismo y los procesos de subducción, el estado de esfuerzos en el interior de la placa en subducción y la estructura de velocidades de las ondas sísmicas en la región.

La estructura y configuración de la zona Wadati-Benioff fue estudiada con los hypocentros de los eventos reportados en el catálogo de la Red Sísmica Regional de Kamchatka, entre 1964 y 1990. Solamente se utilizaron los eventos con magnitud M_w>3.8 y con un error de determinación hipocentral menor de 10 km. Además, se determinaron 44 mecanismos focales para estudiar la distribución de esfuerzos en la zona de subducción de Kamchatka, 21 mecanismos focales fueron determinados por medio de la modelación de ondas de cuerpo registradas telesísmicamente, y doce mecanismos focales más fueron obtenidos con las primeras llegadas de la onda P. Además, se incluyeron once mecanismos reportados por la Universidad de Harvard.

Los resultados indican que el ángulo de subducción de la placa Pacífico por debajo de la península Kamchatka es de ~55° entre los ~50°N y ~55°N. Al norte de ~55°N, la placa sufre una abrupta flexión en una zona de ~30 km. de ancho y el ángulo de subducción disminuye hasta ~35°. La profundidad máxima de la sismicidad, D_m, varia de ~500 km. (~50°N) a ~300 km. (~55°N). Al norte de la zona de deformación, D_m disminuye abruptamente a ~100 km. (~56°N). Esta configuración de la placa subducida permite dividir la ZSK en dos partes: la principal de ~50°N a ~55°N y la parte norte de ~55°N a ~56°N.

La zona de deformación entre la parte principal de la placa y la parte norte se caracteriza, en un corte transversal, por la separación de la sismicidad en dos bandas. La distancia entre estas dos bandas aumenta en función de la profundidad. Esta separación ocurre desde una profundidad de ~80 km. La presencia de un mecanismo focal cuyos planos nodales son paralelos a la zona de deformación sugiere que la deformación de la placa podría ocurrir por medio de una falla tipo tijeras.

La distribución de la sismicidad y de los mecanismos focales muestran que existe una zona sísmica doble que se revela claramente entre los ~50°N y ~55°N, y probablemente se extiende hasta ~56°N. La separación especial entre los planos de la zona sísmica doble es de ~50 km, a una profundidad de ~50 km, y de ~20 km a una profundidad de ~180 km. En la parte superior de la zona sísmica doble, los mecanismos focales cambian, a ~60 km de profundidad, del tipo cabalgadura, reflejando el movimiento relativo de subducción, a los

compresionales a lo largo de la placa subducida. Aparentemente, esto significa que el contacto sismogénico entre las placas se extiende hasta una profundidad máxima de ~60 km.

El frente volcánico es lineal a lo largo de la parte principal de ZSK (de ~50°N a ~55°N) y se proyecta sobre las isosistas de la placa subducida de ~90 a 140 km de profundidad. Al norte de ~55°N, el frente volcánico se desvía hacia el noroeste siguiendo las líneas de isoprofundidad de ~90-140 km. de la parte norte de la placa subducida. Esto indica que la configuración de la placa subducida influye fuertemente en la configuración espacial del arco volcánico de ZSK.

La profundidad máxima de la sismicidad parece estar relacionada con el parámetro térmico de la placa, φ, el cual depende del ángulo de subducción, la edad de la placa subducida y la velocidad de convergencia. Para analizar la relación entre los parámetros de subducción en la ZSK se obtuvo una relación empírica general $D_m=f(\varphi)$ usando los parámetros de subducción (profundidad máxima de sismicidad, el ángulo de subducción, la edad de la placa subducida y velocidad de convergencia) de diversas zonas de subducción de todo el mundo. La comparación del parámetro térmico de ZSK con la relación empírica general demuestra que Kamchatka es consistente con $D_m=f(\varphi)$ entre los ~50°N y ~55°N. Al norte de ~55°N, se observa una disminución en valores de D_m que no coinciden con la relación empírica general. Esta disminución en el valor de D_m sugiere que la edad efectiva, o espesor térmico de la placa oceánica, tendrá que ser dos-tres veces menor que la edad estimada en mediciones directas. Estos resultados se interpretan como consecuencia de un rejuvenecimiento térmico de la placa debido a la presencia de los montes marinos Meiji que se subducen en la parte norte de ZSK. Este probable rejuvenecimiento de la placa en subducción podría provocar la disminución de D_m, la disminución del ángulo de subducción y consecuente deformación de la placa subducida en la zona de subducción de los montes marinos.

La aparente relación entre la distribución del volcanismo activo y la compleja configuración de la placa sugirió estudiar la distribución de las anomalías de velocidades de las ondas sísmicas. Para este fin, 5270 sismos registrados en el área limitada entre 50°N y 60°N y 150°E y 165°E, y registrados al menos por cuatro estaciones, fueron seleccionados para realizar una inversión tomográfica tridimensional. En realidad se realizaron tres inversiones sucesivas con el fin de obtener la imagen tomográfica tridimensional en ZSK. Primeramente, se determinó el modelo unidimensional de velocidades sísmicas como un modelo inicial para las siguientes inversiones tridimensionales. Después, se realizó la inversión tridimensional con un modelo inicial homogéneo. Finalmente, se añadieran la discontinuidad de Conrad, el Moho y la placa subducida definidos como parámetros *a priori*. La inversión con estos parámetros definidos *a priori* dio el mejor resultado, el cual se tomó como la versión final de la tomografía.

La imagen tomográfica de la ZSK muestra una zona de alta velocidad dentro del manto superior inclinada hacia el continente y que se asocia con la placa subducida del Pacífico. El ajuste de los parámetros iniciales sugiere que la placa subducida tiene un espesor de ~70 km y una velocidad de onda P entre ~2% y ~7% más alta que el manto circundante.

Otra anomalía relevante de la velocidad de la onda P se observa bajo el frente volcánico, a una profundidad de 30 km. Esta anomalía de baja velocidad (~6%) forma una banda contínua bajo el arco volcánico. Otras zonas de baja velocidad se extienden hasta una profundidad de ~150-200 km. por debajo del arco volcánico y aparentemente se asocian con la generación de magma que alimenta al volcanismo en superficie.

Las anomalías superficiales de baja velocidad de onda P cerca de la trinchera se relacionan con el prisma de acreción y en tierra a las cuencas sedimentarias en el graben central de Kamchatka. Las anomalías de alta velocidad en la parte trasera del arco volcánico se correlacionan con los levantamientos Ganalsky-Valaginskoe de las rocas de basamento. Finalmente, zonas de alta velocidad situados cerca de los volcanes probablemente se correlacionan con los cuerpos intrusivos.

I. Introducción

La península de Kamchatka es un margen activo donde la placa Pacífico, de edad Cretásica [*Rea et al.*, 1993], se subduce por debajo de la placa Norteamericana. El movimiento relativo entre las placas cambia de subducción, en la trinchera Kuril-Kamchatka, a uno de transcurrencia en la trinchera Aleutiana, en el punto de intersección de éstas dos trincheras. El proceso de subducción esta acompañado por una alta sismicidad y por un volcanismo muy activo a lo largo de toda la zona de subducción de Kamchatka (ZSK). Existe dos estructuras batimétricas que se subducen en ZSK: los montes marinos de Meiji (~54°N), que forman la extensión norte de los montes marinos de Emperador, y la zona de fracturas de Kruzenstern (~52°N).

La placa Pacífico subducida, que es una de las más antiguas del mundo, muestra una abrupta contorsión al norte de ~55°N. Esta flexión súbita recuerda los cambios de geometría en las placas más jóvenes. Este cambio en la geometría de la placa produce un impacto importante en la configuración del frente volcánico.

Sin embargo, la geometría y estado de esfuerzos en ZSK eran poco conocidos. No existía, además, un análisis sistemático de grandes eventos telesísmicos, excepto algunos eventos analizados por *Kao y Chen* [1994] en la parte sur de Kamchatka. Por otro lado, los datos de la Red Sísmica Regional de Kamchatka (RSRK) no habían estado disponibles a la comunidad internacional. Tampoco existían estudios tridimensionales completos de la estructura de velocidades en ZSK. De este modo, excepto algunos pocos artículos, no existían muchas publicaciones acerca de ésta zona de convergencia.

Fedotov [1968] y *Fedotov et al.* [1985] fueron los primeros en estudiar la distribución de la sismicidad en ZSK y determinaron una estructura planar para la mayor parte de ZSK, identificando la disminución gradual de la sismicidad en la parte norte. Luego, *Zobin* [1991] estimó la distribución general de esfuerzos en ZSK, usando los mecanismos focales determinados con las primeras llegadas de la onda P registrados por la Red Sísmica Regional de Kamchatka. Aunque sus resultados no son concluyentes, los datos sugieren la presencia de una zona sísmica doble. *Kao y Chen* [1994] sugieren la presencia de una zona sísmica doble al sur de ~53°N, usando los mecanismos focales determinados mediante la inversión de las ondas de cuerpo registrados telesísmicamente y argumentan que ésta no se extiende mas allá de esta latitud.

Los estudios de distribución de velocidad de las ondas sísmicas en ZSK principalmente, han sido basados en los métodos de refracción. Por ejemplo, la estructura de velocidades en dos dimensiones ha sido estudiada con los métodos de refracción usando explosiones en el océano y el continente [*v.g., Anosov et al.*, 1978; *Selivestrov*, 1983; *Balesta et al.*, 1985]. Estos estudios revelaron un aumento de la velocidad de la onda P en la placa subducida de ~7% y una disminución bajo el frente volcánico de ~4%.

Los tiempos de llegada registrados por la RSRK también han sido usados para determinar la estructura tridimensional usando los métodos de refracción [*Gorshkov*, 1958; *Slavina and Fedotov*, 1974] y la inversión tomográfica [*Slavina and Pivovarova*, 1992]. Sin embargo, estos estudios abarcan solamente áreas limitadas de la península, como por ejemplo algunos volcanes específicos [*Gorshkov*, 1958], la corteza bajo la red sísmica [*Slavina and Fedotov*, 1974] o el área entre la costa y la trinchera [*Slavina and Pivovarova*, 1992]. Estos estudios sugieren que la velocidad de la onda P es de ~7.6 km/s en la corteza inferior y de ~8.2 km/s en la parte superior de la placa subducida.

Nuevos estudios de la configuración de la zona Wadati-Benioff en ZSK son necesarios para refinar los modelos que relacionan la geometría de subducción y la subducción de las estructuras batimétricas a la tectónica de las placas y la actividad volcánica [*v.g.*, *Pilger*, 1977; *Kelleher and McCann*, 1977; *Cross and Pilger*, 1982; *Cahill and Isacks*, 1992]. También, estudios adicionales son necesarios para verificar los modelos que relacionan la forma de la placa subducida y los parámetros de subducción, tales como la edad de la placa y la velocidad de la convergencia [*v.g.*, *Kostoglodov*, 1989; *Kirby*, 1991; *Okal and Kirby*, 1995]. Además, el estudio de la distribución tridimensional de las velocidades de las ondas sísmicas en el interior de la ZSK permitirá mejorar nuestro conocimiento sobre la relación entre la actividad volcánica y la tectónica superficial.

Las metas principales del presente estudio son: 1) estudiar en detalle la estructura de la zona de Wadati-Benioff en ZSK. 2) examinar la configuración y la distribución de esfuerzos de la placa subducida. 3) analizar la relación entre los cambios en la configuración de la placa y los parámetros de subducción. 4) estudiar la relación entre la geometría de subducción y el volcanismo activo en ZSK. 5) obtener una imagen tomográfica tridimensional de la ZSK y relacionarla con la tectónica regional.

Referencias

Anosov, G. I., S. K. Bikkenina, A. A. Popov, K. F. Sergeev, V. K. Utnasin, y V. I. Fedorchenko, *Deep seismic sounding of Kamchatka* (en Ruso), 129 pp., Nauka, Moscow, 1978.

Balesta, S. T., y L. I. Gontovaya, The seismic model of the Earth's crust in the Asiatic-Pacific transition zone (en Ruso), *Volcanology and Seismology, 4*, 83-90, 1985.

Cahill, T. y B. L. Isacks, Seismicity and shape of the subducted Nazca plate, *J. Geophys. Res., 97, B12*, 17503-17529, 1992.

Cross, T. A. y R. H. Pilger Jr., Controls of subduction geometry, location of magmatic arcs, and tectonics of arc and back-arc regions, *Geol. Soc. Am. Bull., 93*, 545-562, 1982.

Fedotov, S. A., On deep structure, properties of the upper mantle, and volcanism of the Kuril-Kamchatka island arc according to seismic data, Am.Geophys.Un., Geophys. Monogr., 12, 131-139, 1968.

Fedotov, S. A., A. A. Gusev, L. S. Shumilina, y G. V. Chernyshova, The seismofocal zone of Kamchatka (en Ruso), *Volcanology and Seismology, 4*, 91-107, 1985.

Gorshkov, G. S., Some questions of theory of volcanology (en Ruso), *Izv. Acad. Sci. USSR Geol., 11*, 23-35, 1958.

Kao, H., y W.-P. Chen, The double seismic zone in Kuril-Kamchatka: The tale of two overlapping single zones, *J. Geophys. Res., 99, B4*, 6913-6930, 1994.

Kelleher, J. y W. McCann, Bathymetric highs and the development of convergent plate boundaries, en *Island arcs, deep sea trenches and back-arc basins*, editores M. Talwani y W. C. Pitman III, pp. 115-122, Am. Geophys. Union, Maurice Ewing Ser. 1, 1977.

Kirby, S., W. B. Durham, y L. A. Stern, Mantle phase changes and deep-earthquake faulting in subduction lithosphere, *Science, 252*, 216-225, 1991.

Kostoglodov, V. V., Maximum depth of earthquakes and phase transformation within the lithospheric slab descending in the mantle (en Ruso), en *Physics and Interior Structure of the Earth*, editor V. A. Magnitsky, Nauka, Moscow, 1989.

Okal, E. A. y S. H. Kirby, Frequency-moment distribution of deep earthquakes; Implications for the seismogenic zone at the bottom of slabs, *Phys. Earth Planet. Inter., 92*, 169-187, 1995.

Pilger, R. H., Jr., Plate reconstruction, aseismic ridges and low-angle subduction beneath the Andes, abstract, *EOS, Am. Geoph. Un. Transactions, 58*, 1232, 1977.

Rea, D., I. Basov, T. Janecek, E. Arnold, J. Barron, L. Beaufort, J. Bristow, P. de Menocal, G. Dubuisson, A. Gladenkov, T. Hamilton, L. Ingram, L. Keigwin, R. Keller, A. Kotilainen, L. Krissek, B. McKelvie, J. Morley, M. Okada, G. Olafson, R. Owen, D. Pak, T. Pedersen, J. Roberts, A. Rutledge, V. Shilov, H. Snoeckx, R. Stax, R. Tiedemann, y R. Weeks, Paleoceanographic record of north Pacific quantified, *EOS, Am. Geoph. Un. Transactions, 74, 36*, 406-411, 1993.

Selivestrov, N. I., Structure of the junction zone of the Kurile-Kamchatka and Aleutian island arcs according to data from continuous seismic profiling (en Ruso), *Volcanology and Seismology, 2*, 53-67, 1983.

Slavina, L. B., y S. A. Fedotov, The velocities of longitudinal waves in the upper mantle beneath Kamchatka (en Ruso), en *Seismicity and earthquake prediction, the properties of the upper mantle and their relation to volcanism in Kamchatka*, editor S. A. Fedotov, pp. 188-200, Nauka, Moscow, 1974.

Slavina L. B., y N. B. Pivovarova, Three-dimensional velocity models of focal zones and refinement of hypocentral parameters, *Phys. Earth and Planetary Int.*, 75, 77-88, 1992.

Zobin, V. M., Initial rupture and the main fault of earthquakes: a comparison of the body wave first arrivals and CMT data for the Kamchatka-Commander region, *Phys. Earth and Planet. Inter., 67*, 313-329, 1991.

II. Profundidad máxima de la sismicidad y el parámetro térmico de la placa subducida: relación empírica general y su aplicación

(Aceptado en: *Tectonophysics*, MS#S18, January 6, 1997)

Maximum depth of seismicity and thermal parameter of the subducting slab: general empirical relation and its application

A. Gorbatov and V. Kostoglodov

Instituto de Geofísica,. Universidad Nacional Autónoma de México, México D.F.,04510, México.

Abstract. The maximum depth of seismicity (D_m) in subduction zones is limited by some physical mechanisms related to the rheological strength of slab material, metastability conditions, failure strength etc. The main factors controlling these properties are temperature and pressure within the lithosphere sinking into the mantle. These P-T conditions may be coarsely assessed from thermal models of slab subduction. The observed relationship between D_m, the age of the subducted lithosphere (A) and the convergence rate (V) can be used to test the theoretical models and reveal inconsistencies which may indicate changes in failure mechanisms with depth. We analyze the relation between D_m and the thermal parameter of the descending slab (φ), which is a product of the age of the subducted lithosphere and the vertical component of convergence rate ($V_\perp$). Seismicity profiles across the subduction zones of Mexico, Chile, Kamchatka, Kuriles, Japan, Sumatra, New Hebrides, Aleutians, Tonga and Marianas are used to estimate D_m. The quasi-linear part of the dependence ($D_m \leq 240$ km, and $\varphi \leq 2000$ km) corresponds to relatively young and slowly descending slab and is in general agreement with the "critical temperature" models of deep earthquakes. For $\varphi > 2000$ km, which corresponds to the relatively older lithosphere subducting at a higher rate, the $D_m = f(\varphi)$ dependence is nonlinear. The flattening of the empirical $D_m = f(\varphi)$ curve in the range of 2000 km $< \varphi <$3500 km is found to be a direct indication of the influence of the equilibrium Ol-Sp phase transition on D_m. Models invoking the metastable Ol-Sp phase transition as a mechanism which controls the deepest seismicity can not be definitely constrained by the results of this study. The general dependence $D_m = f(\varphi)$ may be applied as a standard relation between D_m, A, and V for the analysis of deep earthquakes and seismotectonic studies of the subduction zones.

Introduction

A conductive heating model (McKenzie, 1969) of a lithospheric slab descending into the isothermal mantle has been successful at explaining variations of the maximum depth of seismicity, D_m, along the Tonga-Kermadec trench (Sykes, 1966). D_m is the maximum depth to which a particular "critical" isotherm ($T_{cr} \approx 800°C$) within the subducting slab has penetrated into the mantle. Below the depth D_m the material comprising the subducted slab exhibits temperatures greater than T_{cr}, and loses its ability to generate earthquakes. According to the model, D_m should be proportional to the product of the convergence rate, V, and the age, A, of the lithosphere. For a slab which is subducting in the non-isothermal mantle this relation is valid only for a dip angle, α=90° (vertically subducting slab).

The model is also valid for $\alpha \leq 90°$ if the mantle exhibits a temperature distribution which is close to adiabatic (McKenzie, 1970). In this case a general relation for a particular potential temperature T^{*}_{cr} is

$$L_m \propto VA \ , \tag{1}$$

where L_m is the maximum length of downdip seismic activity along the subducting slab and $A \propto H^2$. H is a thickness of the oceanic lithosphere assuming a halfspace cooling model (e.g., Parker and Oldenburg, 1973). A test of relation (1) with data for different subduction zones shows that the relation is approximately linear for L_m up to 600 km, where $VA < 4000$ km (Molnar et al., 1979; Shiono and Sugi, 1985).

For a vertical temperature gradient in the mantle, the slab heating should depend mostly on the vertical component of the convergence rate, $V_\perp = V\sin\alpha$, instead of the total scalar value of V. Two subduction zones with the same values of V and A but with different dip angles $\alpha_1 < \alpha_2$ would have different lengths of seismic activity, $L_{m1} > L_{m2}$, because adiabatic heating should raise the temperature inside the steeper slab (α_2) as compared to the shallow one. Therefore it is better to reformulate relation (1) in terms of an explicit function of the product $V_\perp A$ (Kostoglodov, 1989); specifically

$$D_m \propto L_m \sin\alpha = k\,VA\sin\alpha + d = k\,\varphi + d\,, \tag{2}$$

where $\varphi = VA\sin\alpha = V_\perp A$ is called, after Kirby et al. (1991), the "thermal parameter" of the descending lithospheric slab, and k and d are constants. Relation (2) is valid if temperature (T_{cr}) is the

only parameter controlling the occurrence of deep earthquakes. This concept is applicable for earthquakes in the shallow lithosphere (e.g., Wiens and Stein, 1983) where the pressure effects are small. T_{cr} can not be the direct physical control for the intermediate and deep seismicity in the high pressure environment where the failure mechanism apparently changes with depth. Nevertheless it is worthwhile to estimate the empirical dependence $D_m = f(\varphi)$ and to compare it with existing theoretical thermal models of the slab. This approach is useful in revealing major discrepancy between the models and data. The discrepancy may be a consequence of some physical effects not considered by the models.

It has been shown that relation (2) agrees roughly with the observed $D_m \leq$ 250-300 km, in the range $\varphi = 0$ to 2000 km (Kostoglodov, 1989). In this range, earthquakes occurring at depths less than 300 km inside the subducting slab are believed to be generated by brittle failure and frictional sliding along the fault surface. That occurs probably when some minerals, such as serpentine, dehydrate and release liquid water (Meade and Jeanloz, 1991). A review of the probable mechanisms and the physical factors controlling deep seismicity may be found in Frohlich (1989) and Lay (1994).

For $\varphi >$ 2000 km the relationship $D_m = f(\varphi)$ is essentially non-linear and therefore the "critical temperature" model is not applicable. Using a data set of D_m, V and A to analyze the $D_m = f(\varphi)$ dependence, Kostoglodov (1989) suggested that the observed deviation of D_m vs. φ from the expected linear dependence may be explained by the influence of the Ol-Sp phase transition, and particularly by the metastable Ol-Sp transition, on the physical mechanism of deep earthquakes. A study of Kalinin and Rodkin (1982) and other recent studies (Green and Burnley, 1989; Green et al., 1990; Kirby et al., 1991; Green, 1994) indicate that earthquakes occurring at depths greater than 300 km may be associated with solid-state phase transitions, predominantly in metastable olivine (for example, transformational faulting, anticrack-associated faulting, etc.). Kirby et al. (1991) argued that the distinctive deviation from linearity of $D_m = f(\varphi)$ for relatively old and rapidly subducting lithosphere may favor the transformational faulting model based on the results of laboratory experiments with phase transition in ice.

The empirical relation $D_m = f(\varphi)$ was previously evaluated with the broadly averaged subduction parameters such as V and A (Kostoglodov, 1989, Kirby et al., 1991, Kirby, 1995, Kirby et al., 1996) and that introduced large uncertainties. Molnar et al. (1979) and Wortel (1982) demonstrated that $T_{cr} \neq$ const, on the contrary, it increases with depth. Thus both temperature and pressure may affect the seismicity cutoff in the subducting slab. Recent numerical modeling of Spencer (1994) revealed that the calculated relationship between slab length, L_m, as defined by temperature threshold T_{cr} = 650 °C, and

the product VA (see eq. (1)) is not linear. Unfortunately, the accuracy of previous empirical relationships is not sufficient to resolve the nonlinearity or even distinguish between the models.

Whatever the actual physical mechanism of intermediate and deep earthquakes may be, the accurate empirical relation $D_m = f(\varphi)$ would be of great interest for the study of deep seismicity and tectonics of subduction zones. For example, relation (2) can be applied to subduction zones with $D_m < 250$ km but unknown convergence velocity or age of subducted lithosphere in order to assess these parameters (Kostoglodov and Bandy, 1995, Gorbatov et al., 1997, Kostoglodov et al., 1996). $D_m = f(\varphi)$ may be also useful for the analysis of deep earthquakes (Gorbatov et al., 1996).

In this study we carefully examined the most recent data on seismicity, A and V for the subduction zones in Mexico, Chile, Kamchatka, Kuriles, Japan, Sumatra, New Hebrides, Aleutians, Tonga and Marianas. The observed empirical dependence $D_m = f(\varphi)$ was then analyzed for the consistency with the recent models of slab heating in order to assess a cutoff temperature for the intermediate and deep focus earthquakes. Possible applications of the general empirical dependence are discussed.

Data and method

To estimate D_m and α we use cross-sections of the Wadati-Benioff seismic zones examined in previous study (Gorbatov et al., 1996). Those are in Mexico, Chile, Kamchatka, Kuriles, Japan, Sumatra, New Hebrides and Aleutians. In addition, several more profiles are considered in Kuriles, Japan, and Sumatra subduction zones. We also completed various cross-sections in Tonga and Marianas.

The following criterion is used for the selection of the subduction zones and seismicity profiles for this study: (a) subduction zones with updated age estimates (by using linear magnetic anomalies) are preferred, (b) the subduction regime should be unperturbed, so the cross-sections must be chosen in sections of subduction zone which do not contain prominent subducted bathymetric features. Also, the profiles are selected so that D_m values represent the widest possible range of depths up to 700 km.

We tried to select cross-sections parallel to the vector of subduction velocity to facilitate the assessment of D_m and α; otherwise a special correction (Shiono and Sugi, 1985) for the angle between the direction of profile and vector V is applied. The value of D_m is taken as the depth of the deepest event along the cross-section (see Figure 1). An average dip angle, α, is calculated as $\arctan(D_m / L_s)$ where L_s is the projection of L_m on the Earth's surface.

The uncertainties associated with maximum seismic depths were estimated for each profile as the separation between the deepest and next deepest event. The uncertainty in the angle of subduction was determined from the uncertainty in D_m. This averaged uncertainty is less than approximately ±1.5°-2.0°.

The convergence rates and the associated uncertainties were calculated from the NUVEL 1A model (DeMets et al., 1994) at the location where the true path of the point corresponding to D_m intersects the trench. The error in V estimates depends on each pair of plates sharing the subduction boundary (DeMets et al., 1994). For the subduction zones of Marianas, New Hebrides and Tonga an effect of back-arc spreading is taken into account in the estimates of V. Unfortunately the back-arc spreading rates are not well known except for the Tonga region where GPS data exist (Bevis et al, 1995).

The main difficulties usually arise in assessing the age of the subducted lithosphere, because A in equations (1, 2) is the age of that segment of the oceanic plate now located at depth D_m when it first started to subduct. To estimate this age we use the relation (Shiono and Sugi, 1985)

$$A = A_t + L_m / V_s - L_m / V , \qquad (3)$$

where A_t is the age of the lithosphere at the trench. Equation (3) assumes that the half spreading rate, V_s, during the time interval A_t to L_m / V_s was constant. Picking errors in A_t are usually less than 1 m.y. The errors in A and φ are calculated using the error propagation equation (e.g., Bevington, 1969) applied to (3) and (2) respectively. In addition to the random errors, some indefinite systematic error may be involved in φ estimates related to the assumption that V_s = const.

The seismicity events from ISC Bulletin (NEIC, CD 1964-1987), with a number of registers at seismic station greater than 9, are selected to assess the subduction parameters. The Japan Meteorological Agency Bulletin (1961-1993) is used to assess D_m and α in the Japan subduction zone. Only events with reliable hypocentral estimates are selected (index of computational method is from 1 to 5). Seismicity profiles across the subduction zone of Mexico are taken from Pardo and Suárez (1995). Seismic data along the Kamchatka subduction zone are from Gorbatov et al. (1997).

Aleutians

Convergence between the North American and Pacific plates along the Alaska-Aleutian trench takes place in a northwest direction with the convergence rate of 60-70 mm/yr (Figure 2). The oceanic plate becomes

progressively older to the south across to the trench (Atwater, 1989). Seismicity defines the downgoing slab up to D_m of about 300 km which is almost constant along the Alaska-Aleutian arc. The dip of the subducting lithosphere shallows progressively to the east from ~40°, underneath the Aleutian islands, to ~20° beneath the Alaska. West of 170°, subduction zone changes gradually into a right lateral transform boundary. The most prominent bathymetric features are the Rat and Amlia fracture zones. The Rat fracture zone consists of a system of the fractures. It divides the oceanic plate into two different zones of spreading (Atwater, 1989). Amlia F.Z. is distinguished by the age difference. The segment of the Aleutian arc where the Rat F.Z. is subducting is not used in the analysis because of the apparently disturbed subduction regime. The location of cross-sections A5 and A6 is selected so that to exclude the effect of subduction of the Amlia F.Z. The A_t, V_{sp} and ϕ (azimuth of V_{sp}) were derived from magnetic anomaly lineations published by Atwater (1989). We exclude from the analysis the area from 156°W to 165°W since the problem of age estimate at the "T" anomaly zone. In total, twelve cross-sections were selected for the Aleutian trench.

Chile

The Nazca plate subducts ENE along the margin of the South American plate with the convergence rate of ~80 mm/yr (Figure 3). D_m increases along the Peru-Chile trench from south (~100 km depth at ~40°S) to north (~600 km depth at ~20°S) and decreases north of ~20°S to ~300 km depth. The main fracture zones (with the largest age offset (Mayes et al., 1990)) subducting at the trench are the Easter and Challenger. There is no clear evidence that two extensive bathymetric structures: Perdida ridge and Juan Fernandez ridge, enter the subduction zone (Kostoglodov, 1994). South of the Challenger F.Z., the dip angle is shallow ~20°. The dip angle in the area between the Easter and Challenger fracture zones increases up to ~35°. North of Easter F.Z., the dip decreases to ~25°.

The age of the subducting Nazca plate increases gradually from ~19 m.y. at ~40°S to ~50 m.y. at ~30°S. In the area between the Easter and Challenger fracture zones the age increases up to 75-80 m.y. and drops down to ~50 m.y. to the north of the Easter F.Z. (Mayes et al., 1990). Spreading rate V_s along the Pacific-Nazca (Farallon) plate boundary was essentially irregular during the subduction history. The major change of V_s (from ~70 mm/yr to ~30 mm/yr) had occurred at ~42 m.a. (Mayes et al., 1990). We included that correction of V_s into the assessment of A (3). To eliminate the influence of fracture zones the segments at 28°S and 18°S are excluded from the analysis. Twenty eight cross-sections are selected along the Peru-Chile trench including one profile (b in Table 1) corresponding to the deep Bolivian earthquake of June 9, 1994. This profile is oriented along and to the south of the Easter F.Z. (Gorbatov et al., 1996).

Japan

The Pacific plate subducts beneath the Japan Islands with the convergence rate of about 90 mm/yr (Figure 4). D_m changes from ~400 km to ~600 km depth. The dip angle is almost constant ~35°. The age of the subducted Pacific plate $A_t \approx 130$ m.y., and it becomes younger with the depth. The A_t and ϕ are determined from Nakanishi et al. (1992), the V_{sp} is taken from Nakanishi et al. (1989). Seven cross-sections are selected along the trench. The influence of the Kashima F.Z. on D_m may be expected only at 41°-42°N, therefore this area is excluded from the analysis.

Kamchatka

In the Kamchatka active margin $V = 75$-78 mm/yr and $A_t \approx 65$-70 m.y. The main subducting bathymetric features are the Meiji seamounts (north of ~54°N) and Kruzenstern fracture zone (at ~52°N) (Figure 5). D_m changes from ~500 km in south to ~300 km depth in north. The spreading pattern has a reverse direction with respect to the subduction vector. A_t and V_{sp} are derived from the age estimates of Renkin and Sclater (1988). The segment, whose maximum seismic depth could be altered by Kruzenstern fracture zone subduction, is not considered. The area to the north of 55°N is excluded from the analysis because of the strong influence of the Meiji seamount subduction. Totally, twelve cross-section were selected based on the study of Gorbatov et al. (1997).

Kuriles

The Pacific plate with $A_t \approx 83$ m.y. subducts beneath the southern Kurile arc with $V \approx 82$ mm/yr. and $\alpha \approx 45°$, generating seismicity down to ~450 km depth. The quiet zone of magnetic anomalies to the north of 45°N limits the studied area (Figure 6). The age and half spreading rate are derived from Larson et al. (1985) and Nakanishi et al. (1992). Only three cross-sections are selected from ~43°N to ~45°N.

Marianas

In the Mariana subduction zone, A_t = 83 m.y., V = 34-45 mm/yr., a segment of deepest seismicity D_m ≈ 600 km is located at ~16°N. D_m gradually decreases up to ~300 km to the north from this point. α increases from ~50° (at ~24°N) to ~70° (at ~15°N). The studied area (Figure 7) in the Mariana arc is restricted by the narrow zone where the magnetic anomaly are identified (from 14°N to 20°N) (Nakanishi et al., 1992). The age of the subducted plate decreases with depth. There are not any known bathymetric features which could alter D_m. Only three cross-sections are selected in the northern part of the Mariana trench from 14°N to 24°N.

The initiation of Mariana back-arc spreading (Figure 8a) is dated as ~6 m.a. (Seno and Maruyama, 1984). The spreading rate of the Mariana ridge is 30-43 mm/yr (Bibee et al., 1980; Hussong and Uyeda, 1981). The direction of the spreading is EW (Carlson and Melia, 1984). Using these data the convergence rate between the Philippine and Pacific plates determined from NUVEL 1A can be corrected for the back-arc spreading rate (Mr* in Table 1). Since the relative motion between the subducting Pacific plate and the back-arc spreading center is not known, we consider the back-arc spreading correction as an uncertainty of V.

Mexico

The Cocos plate subducts with a shallow dip (~20°-25°) beneath the North America plate. D_m changes from ~50 km depth (~103°W) to ~150 km depth (~96°W). The age of subducted plate varies from ~13 m.y. to ~16 m.y. in the SE direction along the trench. The A_t, V_{sp} and ϕ are derived from Mammerickx and Klitgord (1982), and Kostoglodov and Bandy (1995). The Orozco and O'Gorman fracture zones intersect the trench at ~102°N and ~99°N respectively (Figure 9). These fracture zones are not expressed clearly in the bathymetry and the age offset across the zones is not significant. D_m does not seem to be perturbed in the zones where fracture zones subduct (Kostoglodov and Bandy, 1995). Nine cross-sections are selected equally spaced along the Mexican trench.

New-Hebrides

In the New Hebrides subduction zone the Australian plate, A_t ≈ 50 m.y., V=82-91 mm/yr., dips steeply eastward beneath the Pacific plate (Figure 10). The seismicity is traced down to the depth of ~300 km. Only four cross-section in the New Hebrides arc are selected for limited segments where magnetic anomaly

lineations are known (Larue et al., 1977; Circum-Pacific Council for Energy and Minerals Resources, 1981; Weissel et al., 1982).

The age of the back-arc spreading in the North Fiji basin (Figure 8b) is ~5.5 m.a. (Chase, 1971; Malahoff et al., 1982). The spreading rate estimates in this region are 70 mm/yr (Malahoff et al., 1982) and 96 mm/yr (Falvey, 1975). There is not evidence that the western part of the North Fiji basin which overrides the Australian plate is detached from the Pacific plate (e.g., Eguchi, 1984; Charvis et. al., 1989). A noticeable relative movement between the Fiji Islands and Australia plate is not detected (Bevis et al, 1995). The direction and rate of the back-arc spreading coincide with the convergence velocity predicted by NUVEL 1A model for the Pacific and Australian plates (e.g., Eguchi, 1984). For that reason, no correction for the back-arc spreading is applied to V between the Pacific and Australian plates at New Hebrides.

Sumatra

Convergence of the subducting Australian plate, A_t = 64-105, to the northeast along the Sunda trench takes place at ~70 mm/yr with $\alpha \approx 30°$ (Figure 11). The seismicity occurs down to ~250 km. There are numerous fracture zones subducting in the Sunda trench. Magnetic anomaly lineations are estimated in the area limited by 6°N to 4°S. We selected three cross-sections in this area where the deepest seismicity is not perturbed by subduction of bathymetric features. The age and half spreading rate were derived from Neprochnov et al., (1979) and Mueller et al., (1993).

Tonga

The oblique subduction of the Pacific plate, $A \approx 178$ m.y., in the Tonga-Kermadec trench and a lack of age estimates north of 16°S (Sclater et al., 1980) limit an area of the study by 28°S-20°S (Figure 12). The Pacific plate subducts underneath the Australian plate with a dip angle of ~50°. The deepest events occur at ~700 km depth. The half spreading rate is derived from Sclater et al., (1980). Four profiles are selected in a way that two main fracture zones crossing the trench at 26°S and 22°S do not influence the D_m estimates.

The age of opening of the Lau basin (Figure 8b) is less than 4 m.y. (Malahoff et al., 1982). The convergence rate of 164 mm/yr (at 21°S), obtained from direct GPS measurements (Bevis et al, 1995) between the Lau basin and Pacific plate, is taken for the last 4 m.a. The older convergence rate is assumed from NUVEL 1A between the Australian and Pacific plates.

Dependence of D_m on φ

Figure 13 is a plot of $D_m = f(\varphi)$ based on the data from Table 1. An important feature of this plot is a significantly reduced scatter of D_m and smaller errors of φ estimates in comparison with the previous studies (Kostoglodov, 1989, Kirby et al., 1991, Kirby, 1995, Kirby et al., 1996). The approximation of the general empirical relationship by the best fit polynomial curve (Figure 13) with the coefficients $\mathbf{a}(a_0, a_1, \ldots, a_4) = (54, 10^{-1}, 0.44\times10^{-2}, -0.37\times10^{-3}, 0.63\times10^{-5})$ implied in Gorbatov et al. (1996) is consistent with the new data set up to $D_m \approx$ 620-640 km and $\varphi \approx$ 4500 km (thick solid curve in Figure 13). In the range of $\varphi >$ 4500 km (thick dashed curve in Figure 13) D_m remains at 680-700 km level that is probably related to the break down of the relation $A \propto H^2$ at $A >$ 70-80 m.y. (e.g., thermal models of Parsons and Sclater, 1977, Molnar et al., 1979, Stein and Stein, 1992). The ocean lithosphere older than 80 m.y. apparently should have the same thermal thickness as one with $A \approx$ 80 m.y., therefore $\varphi >$ 4500-5000 km may not have a physical meaning as the thermal parameter. Unfortunately, limitations of the halfspace thermal models for the approximation of H at old ages are difficult to assess (S. Stein, 1996, personal communication).

The following procedure is used to compare observed empirical relation with the modeled minimum temperature distribution in the slab. A set of coldest geotherms inside the subducting lithosphere with different values of φ is found from the results of numerical modeling by Goto et al., (1983, 1985). Each of these geotherms represents (Figure 14) the distribution of minimum temperature within the slab as a function of depth or pressure in the mantle. Using the value of φ of each modeled geotherm, the D_m estimate, and its uncertainty from the empirical dependence $D_m = f(\varphi)$ in Figure 13, are superimposed on that geotherm in Figure 14. The range of empirical estimates of D_m in Figure 14 (shaded curved band) defines the P-T conditions of the seismicity cutoff in the subducting slab for the model of Goto et al., (1983, 1985).

Down to $D_m \approx$ 240 km and up to $\varphi \approx$ 1500-2000 km the critical temperature changes gradually from ~ 700°C to ~ 600°C (gray circles in Figure 14). These cutoff conditions of the model correspond to a relatively young and slowly descending slab. They disagree with the results of Molnar et al. (1979), where T_{cr} was rising with depth. The modeled $D_m = f(\varphi)$ curve for T_{cr} = 650°C was obtained from the geotherms presented in Figure 14 and plotted in Figure 13 as a dashed curve (Goto et al., 1983, 1985).

As can be seen from Figure 13, the model does not fit well the empirical $D_m = f(\varphi)$ relation for the constant T_{cr}.

A better approximation for the empirical $D_m = f(\varphi)$ relation in its quasi-linear section ($D_m < 240$ km) is the model of Spencer (1994). In this model the controlling mechanisms of the seismicity cutoff are the drop of compressive slab strength below 10^{13} N/m, and the increase of slab core temperature of more than 650°C. Above this temperature the calculated slab strength is defined entirely by dislocation creep in olivine. The $D_m = f(\varphi)$ dependence from Spencer (1994), adjusted to the empirical data, is shown in Figure 13. This model for the temperature cutoff $T_{cr} = 650$°C is very close to the best fitting polynomial curve only within the range of $\varphi < 2000$ km.

The next range of φ from 2000 km to ~3500 km (relatively older lithosphere subducting at a higher rate) is not related to further apparent increase of D_m. It remains approximately at the level of $D_m \approx 260$ km (Figure 13). For the model of Goto et al., (1983, 1985) T_{cr} in that range of φ decreases even more, down to ~550°C, and for the model of Spencer (1994) this decrease is somewhat less, T_{cr} ~600°C (Figure 14). The drop of T_{cr} may be interpreted by the influence of the Ol-Sp phase boundary which crosses the geotherms with 2000 km $< \varphi <$ 3500 km approximately at a depth of 260 km (Figure 14). Neither of these models includes the effect of latent heat released by the Ol-Sp phase transition which should increase the temperature in the slab core by $\Delta T \approx 130$°C (e.g., Turcotte and Schubert, 1971). The geotherms roughly corrected for ΔT are presented in Figure 15. As can be seen, this correction produces an increase of T_{cr} with depth (as well as with φ) which is physically more meaningful and consistent with the conclusions of previous studies (e.g., Molnar et al., 1979, Wortel, 1982).

The drastic increase of D_m from ~ 260 km to > 600 km in the narrow range of 3500 km $< \varphi <$ 4500 km (Figure 13) has been considered to favor models invoking the metastable Ol-Sp phase transition as a mechanism for the deepest seismicity (e.g., Kostoglodov, 1989, Kirby et al., 1991). Unfortunately, the large uncertainty in D_m and φ in this range and upward deflection of the geotherms for $D_m > 450$ km (as a result of the model inference, the sinking slab is heating from its downgoing tip (Goto et al., 1983, 1985)) do not allow us to support this conclusion. The cutoff P-T conditions for observed values of D_m and φ are far beyond the hypothetical kinetic boundary between metastable olivine and stable spinel with its characteristic temperature $T_{ch} \sim 700$°C (Sung and Burns, 1976) (Figures 14 and 15). It should be noted that in existing thermal models of the slab the temperature distribution strongly depends on various poorly known model parameters and could vary by ±200°C (e.g., Kirby et al., 1996). Nevertheless the trend of the cutoff temperature versus φ (Figure 15) is apparently less model-

dependent and can be interpreted as indicating that the deep earthquakes (D_m > 350-400 km) are a distinct population with a higher T_{ch} ≈ 800-900°C in comparison with the shallower earthquakes with T_{cr} ≈ 650-700°C. The main conclusion from this observation is that shallow and deep seismicity in subduction zones have different failure mechanisms.

Although a number of analytical and numerical models have been proposed for slab thermal structure, only a few (e.g., Goto et al., 1983, 1985; Spencer, 1994) considered different values of φ. More adequate models and modeling results (for a wide range of φ), implying Ol-Sp equilibrium phase transition and metastable Ol-phase in cold slab core are required to achieve more reliable interpretation of the empirical dependence $D_m = f(\varphi)$.

Several convergent zones in the western Pacific (e.g., New Zealand, Solomon Islands etc.) were not considered in this study because the age estimates for these regions are not adequate to make a proper correction for A in equation (3). On the other hand, it may be worth applying the empirical dependence $D_m = f(\varphi)$ in these subduction zones to asses A_t when V and D_m are fairly well known.

We should note that for the smooth-shaped cross-sections with a seismic gap from D'_m to the deepest events D_m (such as the most of profiles in Chile) usually both points D'_m and D_m fit the dependence $D_m = f(\varphi)$. To illustrate that, several D'_m values for the Chilean cross-sections C13-C21 and the Bolivian profile (Gorbatov et al., 1996) (c13-c21 and b1 in Table 1) are plotted in Figure 16 together with the general empirical relation $D_m = f(\varphi)$. All D'_m points are in good agreement with $D_m = f(\varphi)$. This unexpected observation deserves further special and more detailed study. Unfortunately D'_m - D_m seismic gap is not so clearly resolved in other subduction zones. To define the gap, an approach used, for example, by Helffrich and Brodholt (1991) can be applied for every one of the cross-sections.

Application of the general empirical relation $D_m = f(\varphi)$

Molnar et al., (1979) first proposed to use an empirical relation between D_m, V and A to analyze unknown or poorly known seismotectonic parameters in subduction zones. The general empirical relation $D_m = f(\varphi)$, where $\varphi = VA\sin\alpha$, based on the data from Table 1 (Figure 13) is more accurate than the similar relations obtained in previous studies (e.g., Molnar et al., 1979, Shiono and Sugi, 1985, Kostoglodov, 1989, Kirby et al., 1991, Kirby 1995, Kirby et al., 1996). That permits one to apply relation $D_m = f(\varphi)$ in some cases to examine the anomalous features of subduction zones.

Aleutian - Kamchatka trench junction

The maximum depth of seismicity, D_m, in the Kamchatka subduction zone decreases gradually from ~500 km (50°N) to ~300 km (54°N) (Figure 17). The steep change of D_m from ~300 km to ~200 km occurs at 54.5°N where the Meiji seamounts (Figure 5) enter the subduction zone. The area of relatively shallow D_m then continues up to the Aleutian - Kamchatka trench junction (~55.5°N). The origin of this change of D_m is analyzed by applying the general empirical relation $D_m = f(\varphi)$ (Gorbatov et al., 1997). D_m and φ are estimated for several cross-sections (k13-k19 in Table 1) in the northernmost part of the Kamchatka trench (Figure 5). Then these estimates are compared with the relation $D_m = f(\varphi)$ (Figure 18). It can be seen that for the assessed values of $\varphi = V A \sin\alpha$ for profiles k13-k19 the observed values of D_m are anomalously shallow. In contrast, for the profiles in the southern part of the Kamchatka peninsula (Figure 18) the values of D_m fit the empirical curve $D_m = f(\varphi)$ within the limits of the error estimates.

Profiles k13-k19 (Figure 5) cross a relatively old segment of the Pacific plate (A, ~86 m.y.). The convergence rate, dip angle and D_m are well constrained for the area. Using these estimates it is easy to show that D_m would fit the general empirical curve if the age of the Pacific plate in the northern part of the Kamchatka subduction zone was about from two to three times younger (see Figure 18). This speculation is fairly reasonable taking into account the following concerns. There is not any geological or geophysical evidence of an abrupt decrease of V in the northern part of the KSZ. A variation of the dip angle (from ~55° to ~35°) does not produce a substantial reduction of φ. Heat flow data of Smirnov and Sugrobov (1979, 1980 a,b) suggest that the thermal thickness (the depth of 1200°C isotherm) of the subducting oceanic plate is from two to three times less to the north of the Meiji seamounts chain than that to the south of it. Thus the reduced thermal thickness of the subducted plate at profiles k13-k19 corresponds to the effective age which is lower than the geologic age of the Pacific plate.

Deep earthquakes in Chile

The empirical dependence $D_m = f(\varphi)$ is applied to the deep seismicity in central Chile (south of 25°S). Deep events of Chile north of 23°S and south of the Easter fracture zone apparently occurred within the oldest, $A > 80$ m.y. (Mayes et al., 1990), segment of the subducted Nazca plate

(Kostoglodov, 1994) (Figure 19). The shape of seismicity cross-sections and the assessed age (3) of the oceanic lithosphere at the depth (~100 m.y.) do not require total slab detachment in this region, as it have been proposed by Engebretson and Kirby (1992) based on other age appraisal, to explain the maximum depth of seismicity. D_m values corresponding to these cross-sections (C13-C21, Figure 3) are in agreement with the general $D_m = f(\varphi)$ dependence (Figure 18).

Because of a lack of intermediate depth seismicity in the cross-sections corresponding to the deep events located between 25°S and 29°S, it is not clear whether these events pertain to the continuous or detached slab. The shape of cross-sections C1*-C4* (see Figure 3 for the location) favors the hypothesis of the detached slab. On the $D_m = f(\varphi)$ plot these events (C1*-C4* in Figure 18 and Table 1) are scattered around some average value of $\varphi \sim 3500$ km and $D_m \sim 600$ km and shifted from the general curve to lower φ (Figure 18). This may be interpreted to indicate that deep events were taking place within the detached fragment of the Nazca plate. Figure 19 illustrates this interpretation (Kostoglodov, 1994). However, we should note that the application of $D_m = f(\varphi)$ dependence to analyze deep events in old slabs depends critically on the adequacy of halfspace thermal model of oceanic lithosphere with $A > 80$ m.y. If the model breaks down at $A \approx 80$ m.y. there would not be any essential difference of D_m, φ estimates between groups of profiles C13-C21 and C1*-C4*.

Rivera - North America convergence rate

A value of the convergence rate between the Rivera and North American plates is essential to understand the large-scale strain accumulation, recurrence time of large subduction earthquakes and tectonics of the Jalisco block, Mexico (e.g., DeMets et al., 1995). There are two significantly different types of models for the convergence rate between those two plates. The first type, the high-rate model (Bandy, 1992), predicts convergence rates of approximately 50 mm/yr near the southern end of the Rivera - North America subduction zone and between 20-30 mm/yr at its northern end. In contrast, the second type, the low-rate models (e.g., DeMets and Stein, 1990), predicts convergence rate of between 20-33 mm/yr near the southern end of the Rivera - North America subduction zone and between 6-17 mm/yr at its northern end.

To constrain V between the Rivera and North American plates, Kostoglodov and Bandy (1995) applied a slightly modified relation $D_m = f(\varphi)$ in a way similar to that presented in section *4.1*. The analysis was done based on the $D_m = f(\varphi)$ relation observed for the Cocos - North American plates pair.

A comparison of this dependence with D_m and φ (calculated for different convergence rate models) shows that D_m estimates in the Jalisco zone fit $D_m = f(\varphi)$ relation only when the corresponding φ values are assessed applying the high-rate model. It is important that two other independent seismotectonic approaches applied to verify an average V in the Rivera - North America subduction zone (Kostoglodov and Bandy, 1995) favor the high-rate model too.

Discussion and conclusion

A careful analysis has been attempted to retrieve new reliable estimates of D_m from the distribution of seismicity in different subduction zones. The values of A and V were found for each seismicity profile using the latest published data on the age of the ocean floor and the corrected global plate motion model NUVEL 1A (DeMets et al., 1994). Corrections for the back-arc spreading and the age of the subducted slab are introduced. The data contain significantly smaller uncertainties of D_m and φ in comparison with previous studies. A general empirical dependence $D_m = f(\varphi)$ (Gorbatov et al., 1996) is corrected using new data and compared with the modeled $D_m = f(\varphi)$ curves from Goto et al. (1983, 1985) and Spencer (1994) for $T_{cr} = 650°C$. The models fit the empirical relation $D_m = f(\varphi)$ within the uncertainty limits for the range of $D_m <$ 240-260 km (quasi-linear section), and the better fit is obtained for the model of Spencer (1994) (Figure 13). Prominent deviation of the general empirical dependence $D_m = f(\varphi)$ from the model curves in the range of φ from 2000 km to ~3500 km is apparently the after-effect of equilibrium Ol-Sp phase transition which may be elevated up to depth of ~260 km within the relatively cold slab core.

To examine the influence of the Ol-Sp phase transition on D_m we compared the observed values of D_m and φ with the location of the corresponding "coldest" geotherms in the P-T phase diagram. Each geotherm has been estimated using the results of numerical modeling (Goto et al., 1983, 1985) of the temperature distribution within the subducting slab with matching values of V, A and α. Approximate P-T conditions of the seismicity cutoff inside the cold core of the subducting slab were also obtained in a similar way applying the empirical fit $D_m = f(\varphi)$ for slightly extrapolated results of Spencer's (1994) model. For both models an apparent decrease of T_{cr} at the depth of ~190-270 km can be observed (Figure 14) which is in contradiction with the conclusions of several previous studies (e.g., Molnar et al., 1979, Wortel, 1982). After a rough correction of the geotherms for the latent heat released by the equilibrium Ol-Sp phase transition (Figure 15), the seismicity cutoff temperature apparently remains at

$T_{cr} \approx 650°C$ down to a depth of ~350 km. That result evidently relates observed upward deflection of the empirical dependence $D_m = f(\varphi)$ from the modeled curves to equilibrium Ol-Sp phase transition. The latent heat of the Ol-Sp transition increases the temperature within the slab, which partly delays a further increase of D_m in the range of 2000 km < φ <3500 km (Figure 13).

The abrupt increase of D_m from ~ 260 km to > 600 km in the range of 3500 km < φ < 4500 km (Figure 13) can not be interpreted using the results of this study in favor of the deep seismicity being induced by the metastable Ol-Sp phase transition, although we cannot discard this reasonable mechanism. Significant change of cutoff temperature from relatively shallow to deep earthquakes (D_m > 350 km) can be an evidence for different failure mechanisms between those distinct populations of events. To approach the problem, applying the empirical dependence $D_m = f(\varphi)$, an exceptionally accurate age estimate in other subduction zones and more adequate modeling are required.

The best approximating curve (Gorbatov et al., 1996) can be used as a standard general dependence $D_m = f(\varphi)$ for studying the relation between convergence parameters and deep seismicity. This approach has been used in several studies to: (1) estimate the effective thermal age of the Pacific plate subducting in the region of the Aleutian - Kamchatka trench junction; (2) constrain the convergence rate between the Rivera and North American plates; (3) analyze the deep seismicity in the Chilean subduction zone.

Acknowledgments. The authors thank R. Dmowska, C. Lomnitz and J. Pacheco for attentive correction of the manuscript, S. Cande for the discussion on the age estimates. S. Stein made a number of very important suggestions. The GMT-3 System software by P. Wessel and W. Smith was utilized in this study.

References

Akaogi, M., E. Ito, and A. Navrotsky, 1989. Olivine-modified Spinel-Spinel Transitions in the System Mg_2SiO_4-Fe_2SiO_4: Calorimetric Measurements, Thermochemical Calculation, and Geophysical Application, J. Geoph. Res., 94, B11: 15671-15685.

Atwater, T., 1989. Plate tectonic history of the northeast Pacific and western North America, E. L. Winterer, D. M. Hussong, and R. W. Decker (editors), The Eastern Pacific Ocean and Hawaii, The Geology of North America, Geol. Soc. of Am., N: 21-71.

Bandy, W.L., 1992. Geological and geophysical investigation of the Rivera-Cocos plate boundary: Implications for plate fragmentation, Ph.D. thesis, Tex. A&M Univ., College Station.

Bevington, P.R., 1969. Data Reduction and Error Analysis for the Physical Sciences, McGraw-Hill, N.Y., 336 pp.

Bevis, M., F. W. Taylor, B. E. Schutz, J. Recy, B. L. Isacks, S. Helu, R. Singh, E. Kendrick, J. Stowell, B. Taylor, and S. Calmant, 1995. Geodetic observations of very rapid convergence and back-arc extension at the Tonga arc, Nature, 374: 249-251.

Bibee, L. D., G. G. Shor, and R. S. Lee, 1980. Inter-arc spreading in the Mariana Trough, Mar. Geol., 35: 183-197.

Carlson, R. L., and P. J. Melia, 1984. Subduction hinge migration, Tectonophysics, 102: 399-411.

Charvis, P., E. Ruellan, B. Pelletier, and J. Recy, 1989. Widespread extension in New-Hebrides back-arc area (Vanuatu, Southwest Pacific), (Abstract), 28 International Geol. Congress, Washington D. C., p. 1266.

Chase, C. G., 1971. Tectonic history of the Fiji plateau, Bull. Geol. Soc. Am., 82: 3087-3110.

Circum-Pacific Council for Energy and Minerals Resources, Plate-Tectonic Map of the Circum-Pacific Region, Am. Assoc. Petrol. Geol., Tulsa, Okla., 1981.

DeMets, C., and S. Stein, 1990. Present-day kinematics of the Rivera plate and implications for tectonics in Southwestern Mexico, J. Geophys. Res., 95: 21,931-21,948.

DeMets, C., R. G. Gordon, D. F. Argus, and S. Stein, 1994. Effects of recent revisions to the geomagnetic reversal time scale on estimates of current plate motions, Geophys. Res. Lett., 21: 2191-2194.

DeMets, C., I. Carmichael, T. Melbourne, O. Sanchez, J. Stock, G. Suárez, and K. Hudnut, 1995. Anticipating the successor to Mexico's largest historical earthquake, EOS Trans., AGU, 76: 417,424.

Eguchi, T., 1984. Seismotectonic of the Fiji Plateau and Lau basin, Tectonophysics, 102: 17-32.

Engebretson, D., and S. Kirby, 1992. Deep Nazca slab seismicity: Why is it so anomalous?, EOS Trans. AGU, 73(43), Fall Meet. Suppl., 379.

Falvey, D., 1975. Arc reversals and a tectonic model for the North Fiji Basin, Bull. Aust. Soc. Explor. Geophys., 6(2/3): 47-49.

Frohlich, C., 1989. The nature of deep-focus earthquakes, Ann. Rev. Earth Planet. Sci., 17: 227-254.

Gorbatov, A., V. Kostoglodov, and E. Burov, 1996. Maximum seismic depth versus thermal parameter of subducted slab: application to deep earthquakes in Chile and Bolivia, Geofisica Int., 35: 41-50.

Gorbatov, A., V. Kostoglodov, G. Suárez, and E. Gordeev, 1997. Seismicity and structure of the Kamchatka subduction zone, J. Geophys. Res., (in press).

Goto, K., H. Hamaguchi, and Z. Suzuki, 1983. Distribution of stress in descending plate in special reference to intermediate and deep focus earthquakes. I. Characteristics of thermal stress distribution, Tohoku Geophys. J. (The science reports of the Tohoku University, Series 5), 29: 81-105.

Goto, K., H. Hamaguchi, and Z. Suzuki, 1985. Earthquake generating stresses in a descending slab, Tectonophysics, 112: 111-128.

Green, H. W., and Burnley, P. C., 1989. A new self-organizing mechanism for deep-focus earthquakes, Nature, 341: 733-737.

Green, H. W., Young, T. E., Walker, D., and Scholz, C. H., 1990. Anticrack associated faulting at very high pressure in natural olivine, Nature, 348: 720-722.

Green, H. W., 1994. Solving the Paradox of deep earthquakes, Scientific American, 50-57.

Helffrich, G., and J. Brodholt, 1991. Relationship of deep seismicity to the thermal structure of subducted lithosphere, Nature, 353: 252-255.

Hussong, D. M., and S. Uyeda, 1981. Tectonic processes and the history of the Mariana Arc: a synthesis of the results of Deep Sea Drilling Project Leg 60, Initial reports of the Deep Sea Drilling Project, 60, U. S. Government Printing Office, Washington D. C., pp. 909-929.

Kalinin, V. A., and M. V. Rodkin, 1982. Physical model for the source of deep focus earthquakes, Izv. Acad. Sci. USSR Geophys., 8: 3-12.

Kirby, S., W. B. Durham, and L. A. Stern, 1991. Mantle phase changes and deep-earthquake faulting in subduction lithosphere, Science, 252: 216-225.

Kirby, S., 1995. Interslab earthquakes and phase change in subducting lithosphere, Rev. Gephys., Suppl., U.S. National Report to International Union of Geodesy and Geophysics 1991-1994, 287-297.

Kirby, S.H., S. Stein, E.A. Okal, and D.C. Rubie, 1996. Metastable mantle transformations and deep earthquakes in subducting oceanic lithosphere, Rev. Geophys., 34: 261-306.

Kostoglodov, V.V., 1989. Maximum depth of earthquakes and phase transformation within the lithospheric slab descending in the mantle, V. A. Magnitsky (editor), Physics and Interior Structure of the Earth, Nauka, Moscow, pp. 52-57.

Kostoglodov, V., 1994. Structure and seismotectonic segmentation of Chilean subduction zone, 7° Congreso Geológico Chileno 1994, Concepción, 17-20 Oct. 1994, Univ. de Concepción, Actas Volumen II, 1383-1387.

Kostoglodov, V., and W. Bandy, 1995. Seismotectonic constraints on the convergence rate between the Rivera and North American plates, J. Geophys. Res., 100: 17,977-17,989.

Kostoglodov V., M. Guzman-Speziale and W. Bandy, 1996. Seismotectonic constraints on the age of the lithosphere in the Guatemala basin, EOS Trans. AGU, 77(42), Fall Meet. Suppl., 646.

Larson, R. L., W. C. Pitman III, X. Golovchenco, C. S. Cande, J. F. Dewey, W. F. Haxby, and J. L. LaBrecque, 1985. The Bedrock Geology of the World, Freeman and Co., N. Y.

Larue, B. M., J. Daniel, C. Jouannic, and J. Recy, 1977. The South Rennel trough: evidence for a fossil spreading zone, in International Symposium on Geodynamics in South-West Pacific, Noumea, 1976., Editions Technip, Paris, pp. 51-62.

Lay, T., 1994. Seismological constraints on the velocity structure and fate of subducting lithospheric slabs: 25 years of progress, Advances in Geophysics, 35: 1-185.

Malahoff, A., R. H. Feden, and H. S. Fleming, 1982. Magnetic anomalies and tectonic fabric of marginal basins north of New Zealand, J. Geophys. Res., 87: 4109-4125.

Mammerickx, J., and K. Klitgord, 1982. Northern East Pacific rise: evolution from 25 m.y. B.P. to the present, J. Geophys. Res., 87: 6751-6759.

Mayes, C. L., L. A. Lawver, and D. T. Sandwell, 1990, Tectonic history and new isochron chart of the South Pacific, J. Geophys. Res., 95: 8543-8567.

McKenzie, D. P., 1969. Speculations on the consequence and cause of plate motions, Geophys. J. R. Astron. Soc., 18: 1-32.

McKenzie, D. P., 1970. Temperature and potential temperature beneath island arcs, Tectonophysics, 10: 357-366.

Meade, C. and R. Jeanloz, 1991. Deep-Focus earthquakes and recycling of water into the Earth's Mantle, Science, 252: 68-72.

Molnar, P., D. Freedman, and J. S. Shih, 1979. Length of intermediate and deep seismic zones and temperatures in downgoing slabs of lithosphere, Geophys. J. R. Astron. Soc., 56: 41-54.

Mueller, R. D., W. R. Roest, J.-Y. Royer, L. M. Gahagan, and J. G. Sclater, 1993. A digital age map of the oceanic floor, SIO Reference Series No. 93-30, Scripps Inst. of Oceanography, Univ. of California at San Diego, La Jolla, Ca.

Nakanishi, M., K. Tamaki, and K. Kobayashi, 1989. Mesozoic magnetic anomaly lineations and seafloor spreading history of the Northwestern Pacific, J. Geophys. Res., 94: 15437-15462.

Nakanishi, M., K. Tamaki, and K. Kobayashi, 1992. Magnetic anomaly lineations from Late Jurassic to Early Cretaceous in the west-central Pacific Ocean, Geophys. J. Int., 109: 701-719.

Neprochnov, Y. N., L. R. Merklin, and A. A. Shreyder, 1979. New data on the structure and geomagnetic field of the Sunda (Java) trench, Oceanology, Acad. Sci. USSR, Engl. Transl., 19, 3: 281-283.

Pardo, M., and G. Suárez, 1995. Shape of the subducted Rivera and Cocos plates in Southern Mexico: Seismic and Tectonic implications, J. Geophys. Res., 100, B5: 12357-12373.

Parker, R.L., and D.W. Oldenburg, 1973. Thermal models of ocean ridges, Nature, 242: 137-139.

Parsons, B., and J.G. Sclater, 1977. An analysis of the variation of ocean floor bathymetry and heat flow with age, J. Geophys. Res., 82: 803-823.

Renkin, M.L., and J.G. Sclater, 1988. Depth and age in the North Pacific, J. Geophys. Res., 93: 2919-2935.

Sclater, J. G., C. Jaupart, and D. Galson, 1980. The heat flow through oceanic and continental crust and the heat loss of the Earth, Rev. Geophys. Space Phys., 18: 1, 269-311.

Seno, T., and S. Maruyama, 1984. Paleogeographic reconstruction and origin of the Philippine sea, Tectonophysics, 102: 53-84.

Shiono, K., and N. Sugi, 1985. Life of an oceanic plate: cooling time and assimilation time, Tectonophysics, 112: 35-50.

Smirnov, Ya. B., and V. M. Sugrobov, 1979. Terrestrial heat flow in the Kurile-Kamchatka and Aleutian provinces. I. Heat flow and tectonics, Volcanology and Seismology, 1: 59-73, (in Russian).

Smirnov, Ya. B., and V. M. Sugrobov, 1980a. Terrestrial heat flow in the Kurile-Kamchatka and Aleutian provinces. II. The map of measured and background heat flow, Volcanology and Seismology, 1: 16-31, (in Russian).

Smirnov, Ya. B., and V. M. Sugrobov, 1980b. Terrestrial heat flow in the Kurile-Kamchatka and Aleutian provinces. III. Assessments of temperature at depth and thickness of the lithosphere, Volcanology and Seismology, 2: 3-18, (in Russian).

Spencer, J. E., 1994. A numerical assessment of slab strength during high- and low-angle subduction and implications for Laramide orogenesis, J. Geophys. Res., 99: 9227-9236.

Stein, C.A., and S. Stein, 1992. A model for the global variation in oceanic depth and heat flow with lithoshperic age, Nature, 359: 123-129.

Sung, C.M., and R.G. Burns, 1976. Kinetics of high-pressure phase transformations: implications to the evolution of the olivine-spinel transition in the downgoing lithosphere and its consequences on the dynamics of the mantle, Tectonophysics, 31: 1-32.

Sykes, L., 1996. The seismicity and deep structure of island arcs, J. Geophys. Res., 71: 2981-3006.

Turcotte, D.L., and G. Schubert, 1971. Structure of the Olivine-Spinel phase boundary in the descending lithosphere, J. Geophys. Res., 76: 7980-7987.

Von Herzen, R.P., 1967. Heat flow and some implications for the mantle, T.G. Gaskell (editor), The Earth's Mantle, Academic, N.Y., pp. 197-230.

Weissel, J. K., A. B. Watts, and A. Lapouille, 1982. Evidence for late Paleocene to late Eocene seafloor in the southern New Hebrides basin, Tectonophysics, 87: 243-2251.

Wiens, D.A., and S. Stein, 1983. Age dependence of oceanic interplate seismicity and implications for lithospheric evolution, J. Geophys. Res., 88: 6455-6468.

Wortel, M.J.R., 1982. Seismicity and rheology of subducted slab, Nature, 296: 553-556.

Table 1. Summary of parameters

Prof.	Lat °N	Lon °E	Az deg.	V^e mm/yr.	θ deg.	A_t m.y.	A^c m.y.	α deg.	D_m km	δD_m km	φ 10^2km	$\delta\varphi$ 10^2km
A1	51.6	172.7	27	73	317	35	36	35	120	20	5.0	0.5
A2	50.5	177.8	17	73	318	44	44	36	166	5	9.8	0.6
A3	50.2	-179.6	4	72	320	64	62	44	245	5	22.4	1.4
A4	50.3	-177.4	357	71	320	63	63	43	253	25	24.2	1.5
A5	50.7	-174.6	352	70	322	63	63	37	232	5	23.1	1.8
A6	50.9	-171.2	347	68	324	52	51	42	263	30	21.4	1.0
A7	51.5	-168.3	328	67	325	51	51	40	237	30	21.8	1.2
A8	55.0	-154.5	328	59	335	53	52	25	180	30	13.1	1.5
A9	55.4	-153.4	328	58	336	50	52	26	211	33	13.5	1.8
A10	55.8	-152.4	328	58	337	48	52	30	250	30	14.9	0.7
A11	56.3	-151.2	328	57	338	50	48	23	172	10	10.5	0.6
A12	57.4	-148.8	328	55	341	46	46	20	150	20	8.4	0.5
b	-18.5	-72.5	47	77	81	79	92	39	270	10	30.9	1.4
C1	-42.0	-75.5	74	80	80	14	15	14	90	5	3.4	0.4
C2	-41.0	-75.3	74	80	80	19	20	18	120	25	5.8	0.6
C3	-40.0	-75.1	74	80	80	20	20	22	160	15	7.4	0.4
C4	-39.0	-75.0	74	80	79	25	25	25	185	13	10.3	0.6
C5	-38.0	-74.9	74	80	79	30	31	19	145	28	9.8	0.5
C6	-37.0	-74.7	74	80	79	31	32	23	195	13	12.1	0.7
C7	-36.0	-74.3	74	80	79	33	34	19	170	10	10.7	0.6
C8	-35.0	-73.9	74	80	79	36	41	19	185	13	10.5	0.9
C9	-34.0	-73.3	74	80	79	37	47	17	190	5	11.0	0.7
C10	-33.0	-72.9	74	80	78	39	55	14	190	20	10.8	1.2
C11	-32.0	-72.7	74	80	78	42	62	14	180	15	12.1	0.9
C12	-31.5	-72.8	74	80	78	48	64	21	210	15	18.3	1.4
C13	-27.0	-72.0	74	80	78	62	92	33	600	10	40.4	1.6
C14	-26.0	-71.7	74	80	78	69	98	33	570	15	42.3	1.7
C15	-25.0	-71.5	74	79	78	72	103	29	550	40	39.8	1.7
C16	-24.0	-71.5	74	79	78	76	108	29	570	15	41.7	1.8
C17	-23.0	-71.4	74	79	78	79	108	32	560	15	45.3	1.8
C18	-22.3	-71.3	74	78	77	82	111	33	570	15	46.7	2.3
C19	-21.0	-71.4	74	78	77	83	111	36	610	15	50.9	2.4
C20	-20.0	-71.6	74	78	77	84	111	37	600	20	51.9	2.4
C21	-19.0	-72.7	74	77	78	84	112	35	600	20	49.6	1.9
C22	-17.4	-74.4	74	77	79	57	73	23	230	10	21.9	1.9
C23	-16.5	-75.4	74	77	79	51	67	26	270	10	22.3	1.1
c14	-26.0	-71.7	74	80	78	69	85	26	250	5	29.8	1.8
c15	-25.0	-71.5	74	79	78	72	87	25	250	5	29.1	2.3

c16	-24.0	-71.5	74	79	78	76	94	29	300	5	36.0	2.0
c17	-23.0	-71.4	74	79	78	79	97	29	320	10	36.9	2.0
c18	-22.3	-71.3	74	78	77	82	102	32	490	15	42.2	2.6
c19	-21.0	-71.4	74	78	77	83	97	33	290	20	41.2	2.0
c20	-20.0	-71.6	74	78	77	84	99	30	280	5	38.7	1.6
c21	-19.0	-72.7	74	77	78	84	102	25	280	20	33.7	1.6
C1*	-31.0	-72.7	74	80	78	49	81	33	620	10	34.8	1.4
C2*	-30.2	-72.6	74	80	78	51	83	33	620	10	35.7	1.8
C3*	-29.3	-72.6	74	80	78	52	83	32	590	10	34.8	1.8
C4*	-28.4	-72.5	74	80	78	58	89	32	595	5	37.7	1.6
c1*	-31.0	-72.7	74	80	78	49	66	10	140	10	9.2	1.4
c2*	-30.2	-72.6	74	80	78	51	70	16	190	10	15.4	1.5
c3*	-29.3	-72.6	74	80	78	52	70	18	200	10	17.3	1.5
c4*	-28.4	-72.5	74	80	78	58	77	9	130	10	9.6	1.6
Jp1	35.2	142.4	303	93	292	127	95	29	541	10	41.8	2.8
Jp2	36.9	143.5	295	92	292	123	99	30	424	20	45.6	3.5
Jp3	38.3	144.1	290	91	293	121	90	29	588	20	39.8	3.0
Jp4	39.5	144.4	283	90	293	131	106	29	588	35	45.9	3.0
Jp5	40.2	144.3	283	90	293	131	105	29	588	10	45.5	3.8
Jp6	40.9	144.7	310	90	293	129	107	27	388	10	42.5	2.4
Jp7	41.4	145.5	324	90	294	129	101	32	518	70	41.7	2.3
K1	50.2	159.4	302	78	306	105	73	45	482	41	40.2	5.7
K2	50.6	159.8	302	77	306	104	77	44	400	24	41.3	5.5
K3	50.9	160.2	302	77	307	104	74	49	482	153	43.4	7.2
K4	51.3	160.6	302	77	307	104	72	45	482	141	39.1	6.8
K5	51.7	160.8	302	77	307	103	75	47	424	18	42.4	6.1
K6	52.1	161.1	302	76	307	92	71	53	329	10	42.9	6.3
K7	52.8	161.9	302	76	308	93	69	45	423	117	36.9	6.0
K8	53.1	162.4	302	76	309	91	70	43	341	23	36.3	5.3
K9	53.5	162.8	302	75	309	91	70	46	335	35	37.8	5.9
K10	53.8	163.0	302	75	309	91	71	43	306	6	36.5	5.3
K11	54.2	163.2	302	75	309	90	73	44	282	70	37.5	6.2
K12	54.5	163.4	302	75	309	90	72	45	298	27	38.2	5.4
k13	54.7	163.5	302	75	310	89	76	42	211	10	37.8	5.0
k14	54.9	163.5	302	75	310	89	77	45	182	10	40.4	5.9
k15	55.0	163.5	302	75	310	89	77	45	182	11	40.4	5.3
k16	55.2	163.6	302	75	310	88	76	40	176	12	36.7	5.5
k17	55.3	163.8	302	75	311	88	75	38	171	47	33.8	5.3
k18	55.5	163.9	302	75	311	87	78	31	111	5	29.6	3.8
k19	55.7	164.2	302	75	311	87	77	25	94	11	24.1	3.2
Ku1	44.5	150.0	320	82	300	114	82	45	460	10	44.2	1.5

Ku2	44.0	149.0	320	82	300	114	85	43	400	15	44.2	1.5
Ku3	43.3	148.0	320	82	299	114	84	40	400	10	41.4	1.4
M1	15.3	-96.0	33	67	33	16	16	25	145	8	4.6	0.4
M2	15.4	-97.0	34	65	34	16	16	20	125	8	3.4	0.4
M3	15.6	-98.0	35	62	35	15	15	15	100	15	2.3	0.3
M4	15.9	-99.0	35	60	35	14	14	17	96	9	2.3	0.3
M5	16.2	-100.0	35	58	35	13	13	13	65	5	1.7	0.2
M6	16.5	-101.0	36	55	36	13	12	12	55	8	1.3	0.2
M7	16.8	-102.0	36	53	36	14	13	13	55	8	1.5	0.2
M8	17.3	-103.0	36	50	36	13	13	26	99	10	2.9	0.3
M9	17.9	-103.9	36	47	36	13	13	25	88	8	2.5	0.3
Mr1	17.5	147.9	310	39	311	157	115	58	700	39	37.6	1.7
Mr2	17.0	147.7	310	38	311	158	115	60	650	10	37.6	1.4
Mr3	16.5	147.5	310	37	311	160	124	61	600	250	39.9	6.0
Mr1*	17.5	147.9	310	49	311	157	119	58	700	39	49.9	1.7
Mr2*	17.0	147.7	310	48	311	158	120	60	650	10	50.0	1.4
Mr3*	16.5	147.5	310	50	312	160	129	61	600	250	56.4	6.0
N1	-12.0	165.7	75	91	80	28	24	63	250	10	19.4	0.9
N2	-14.8	166.6	75	87	80	54	45	70	260	10	36.3	1.0
N3	-15.6	166.8	75	85	80	53	44	65	260	20	33.7	1.2
N4	-17.6	167.1	75	82	80	50	45	55	250	10	30.3	1.1
Su1	-4.5	100.0	50	68	19	65	53	30	210	15	16.9	0.9
Su2	0.0	96.5	50	65	18	69	52	24	196	20	13.4	0.6
Su3	3.7	93.5	50	62	16	110	95	33	245	88	31.8	5.6
T1	-21.9	-173.9	290	74	274	109	107	50	710	20	58.0	1.1
T2	-23.3	-174.8	290	71	273	109	107	55	700	35	60.0	1.2
T3	-25.6	-175.3	290	68	273	103	101	49	690	20	49.0	1.1
T4	-27.6	-175.7	290	64	272	102	99	50	700	99	46.0	1.9
T1*	-21.9	-173.9	290	107	283	109	109	50	710	20	89.7	3.9
T2*	-23.3	-174.8	290	94	281	109	108	55	700	35	83.1	3.9
T3*	-25.6	-175.3	290	73	278	103	100	49	690	20	55.5	2.7
T4*	-27.6	-175.7	290	61	274	102	97	50	700	99	45.4	2.8

The column abbreviations are: Lat - Latitude, Lon - Longitude (coordinates of the intersection point between the profile and the trench), Az - Azimuth of the cross-section, V - convergence velocity; θ - Azimuth of the convergence velocity, A_t - age of the lithosphere at the trench, A^c - age of the subducted lithosphere as in (3), α - average dip angle; φ - thermal parameter (2), δD_m and $\delta\varphi$ are uncertainties in the estimates of D_m and φ respectively.

[a] Abbreviations are: A- Aleutians; b- Northern Chile-Bolivia; C- Chile; C*- Chile, profiles for the detached slab; Jp -Japan; K - Kamchatka; k - Northern Kamchatka trench; Ku - Kuriles; Mr - Marianas;

Mr* - Marianas with the back-arc spreading correction; M - Mexico; N - New Hebrides; Su - Sumatra; T - Tonga; T* - Tonga with the back-arc spreading correction; c, c* - the same as C and C* in Chile but D_m is D'_m - maximum depth ahead of the aseismic gap.

[b] Derived from DeMets et al. (1994); the convergence velocities for Mr* and T* are shown corrected for back-arc spreading.

[c] Aleutians: Atwater (1989); Chile: Mayes et al. (1990); Japan: Nakanishi et al. (1992); Sumatra: Neprochnov et al. (1979), Mueller et al. (1993); Kamchatka: Renkin and Sclater (1988); Kuriles: Larson et al. (1985), Nakanishi et al. (1992); Marianas: Nakanishi et al. (1992); Mexico: Mammerickx and Klitgord (1982); New Hebrides: Larue et al. (1977), Circum-Pacific Council for Energy and Minerals Resources (1981), Weissel et al. (1982); Tonga: Sclater et al., (1980).

Figure captions

Figure 1. Seismicity cross-section illustrating how L_m, D_m, δD_m, α and $\delta\alpha$ are measured. D_m is taken as the depth of the deepest event along the cross-section. An average dip angle, α, is calculated as $\arctan(D_m/L_s)$, where L_s is the projection of L_m on the Earth's surface. The uncertainties associated with maximum depth of seismicity are assessed as the separation between the deepest and next deepest event. The uncertainty in the angle of subduction is determined from the uncertainty of D_m. Dashed line is an approximation of the seismic surface of the subducting slab.

Figure 2. Tectonic framework of the Aleutian subduction zone. Numbered letters identify the cross-sections used in this study. Dashed lines represent fracture zones. Arrows show subduction vector with convergence rate in mm/yr. Shaded triangle is "T" anomaly zone. Aleutian trench is marked by 6000 m isodepth contour.

Figure 3. Chilean subduction zone. Dashed lines show Easter and Challenger fracture zones. Arrows show subduction vector with convergence rate in mm/yr. Peru-Chile trench is traced by 5000 m isodepth contour. Other symbols are the same as in Figure 2.

Figure 4. Location of the cross-sections in the Japan subduction zone. Arrows show subduction vector with convergence rate in mm/yr. Dashed line is the location of the Kashima fracture zone. The trench is traced by 6000 m isodepth contour.

Figure 5. General tectonic setting of the Kamchatka subduction zone. Dashed line is Kruzenstern fracture zone. The trench is traced by 5000 m isodepth contour. Meiji seamounts are marked by 4000 and 3000 m isodepth contours. Other symbols are the same as in Figure 2.

Figure 6. Southern Kuriles subduction zone. Trench is shown by 7000 m isodepth contour. Other symbols are the same as in Figure 2.

Figure 7. Cross-section selected in the Mariana subduction zone. Trench is traceded by 7000 m isodepth contours. Other symbols are the same as in Figure 2. Back-arc spreading system in Marianas is illustrated in Figure 8a.

Figure 8. (a). Sketch illustrating the back-arc spreading system of the Mariana subduction zone. PAC is the Pacific plate and PHIL is the Philippine plate. Double broken line is the area of spreading. Thin arrows indicate the direction of spreading and thick arrows are the subduction vectors in the Mariana trench. (b). New-Hebrides and Tonga back-arc spreading systems. AUST is the Australian plate and PAC is the Pacific plate. NF is the North Fiji basin. Shaded ellipse is the location of the Fiji islands. Double thin lines denote the back-arc spreading zones. Thin arrows show the direction of spreading. Thick arrows are the vectors of relative motion of the PAC and AUST. L - the Lau Basin.

Figure 9. Mexico subduction zone. Dashed lines mark the Orozco and O'Gorman fracture zones. Middle America trench is traced by 4000 m isodepth contour. Other symbols are the same as in Figure 2.

Figure 10. New Hebrides tectonic setting. 5000 m isodepth contours mark the trench. Other symbols are the same as in Figure 2. Back-arc spreading system in New Hebrides is illustrated in Figure 8b.

Figure 11. Sumatra subduction zone. Dashed lines represent fracture zones. Trench location is shown by 4000 m isodepth contour. Other symbols are the same as in Figure 2.

Figure 12. Tectonic framework of the Tonga subduction zone. Dashed lines are fracture zones. 6000 m isodepth contour marks the trench location. Other symbols are the same as in Figure 2. Back-arc spreading system in Tonga is illustrated in Figure 8b.

Figure 13. Plot of the observed D_m against the thermal parameter of descending slab, φ, based on the data from Table 1. Heavy gray curve is the best-fitting polynomial $D_m = f(\varphi)$ and thin curves are 95% confidence bounds. Dashed heavy gray curve is $D_m = f(\varphi)$ for $\varphi > 4500$ km. Long dashed curves are $D_m = f(\varphi)$ dependencies assessed from Goto et al. (1983, 1985) and from Spencer (1994) for T_{cr} = 650°C. The last one is adjusted to the empirical data (120 km shift for the thickness of the continental lithosphere in the model). Shaded rectangular areas illustrate the uncertainties in the estimates of φ for the Marianas subduction zone associated with back-arc spreading correction of V.

Figure 14. Phase diagram and coldest geotherms of the subducting slab (lines annotated with the values of φ) from the thermal model of Goto et al. (1983, 1985). The circles indicate D_m for each geotherm with its particular value of φ for the model of Goto et al. (1983, 1985) and diamonds are D_m for the model of Spencer (1994). Open symbols denote interpolated values. Straight lines are equilibrium transitions for different phases ($\alpha \rightarrow \beta \rightarrow \gamma$) of the composition $(Mg_{0.89} - Fe_{0.11})_2 SiO_4$ (Akaogi et al., 1989). Shaded curved band represents average P-T conditions of seismicity cutoff in the subducting slab (model of Goto et al., (1983, 1985)) with different values of φ. Gray long dashed curve is the expected kinetic phase boundary between the metastable and stable phases with the characteristic temperature T_{ch} ~700°C (Sung and Burns, 1976). Host mantle geotherm ($\varphi = 0$) (Von Herzen, 1967) used in the model of Goto et al., (1983, 1985). Dashed black lines are coarse interpolations of the geotherms for $\varphi = 45.3$ and $\varphi = 55.4$ as if the slab in the model of Goto et al. (1983, 1985) were not heated from its bottom tip.

Figure 15. Same as Figure 14, except the coldest geotherms are corrected for the latent heat effect of equilibrium Ol-Sp phase transition, $\Delta T = 130$°C. The points of the maximum seismic depth, D_m, below the $\alpha+\gamma$ phase line are shifted by that correction. Open circles and diamond denote D_m corresponding to interpolated and extrapolated values of φ. Topmost dashed line is the mantle geotherm in the model of Spencer (1994).

Figure 16. Observed D_m against φ for the Chilean cross-sections (Figure 3 and Table 1) and the Bolivian profile (Gorbatov et al., 1996) (b1 in Table 1). Gray curve is the best-fitting polynomial $D_m = f(\varphi)$ and thin curves are 95% confidence bounds. Legend: Chile - (c*) the same cross-sections as marked by C* but the deepest events in the detached slab are not considered; Chile - (c) Chilean cross-sections C with D'_m - maximum depth ahead of the aseismic gap.

Figure 17. Earthquake hypocentral projection on the Kamchatka trench axis (Gorbatov et al., 1997). Arrow marks the Meiji seamounts and short vertical line shows the Aleutian trench location. Shaded triangles are active volcanoes. Abrupt decrease of D_m is observed at 54.5°N.

Figure 18. Upper part (D_m<500 km): Comparison of D_m, φ data observed for the Kamchatka subduction zone and the empirical relation $D_m = f(\varphi)$. Arrows indicate the shift of the observed data for the Northern Kamchatka trench (filled diamonds) in order to fit general dependence. Lower part (D_m>500 km): Plot of the observed deepest D_m versus φ for the Chilean subduction zone. Cross-sections C13-C21 correspond to the oldest (~80 m.y.) segment of the subducted Nazca plate. The deepest events in cross-sections C1*-C4* apparently occur within the detached fragment of the slab and are shifted from the general relation $D_m = f(\varphi)$ to the lower φ (see Figure 19).

Figure 19. 3D Wadati-Benioff seismic surface (WBSS) of the Chilean subduction zone synthesized using ISC catalog of seismicity data (Kostoglodov, 1994). Detached segment of the subducted Nazca plate is seen between ~24°-29°S. Dotted lines are strikes of the main fracture zones extrapolated down dip along the WBSS. Inverted filled triangles are the "roots" of active volcanoes (projection of locations of volcanoes on the WBSS).

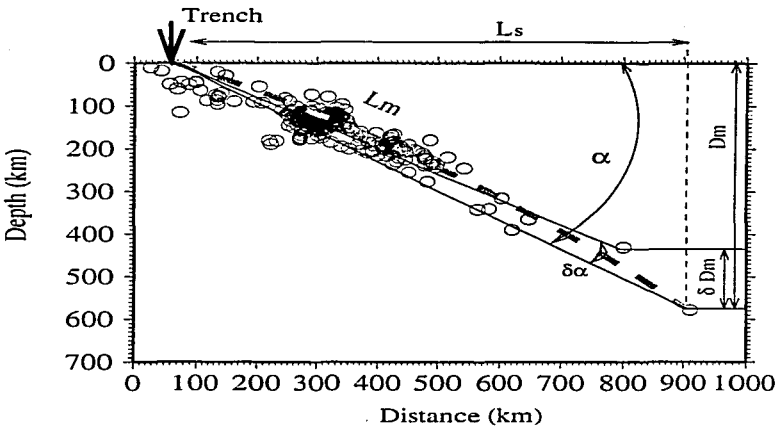
Trench
Ls
Lm
α
Dm
δα
δ Dm
Depth (km)
0
100
200
300
400
500
600
700
0 100 200 300 400 500 600 700 800 900 1000
Distance (km)

Figure 1.

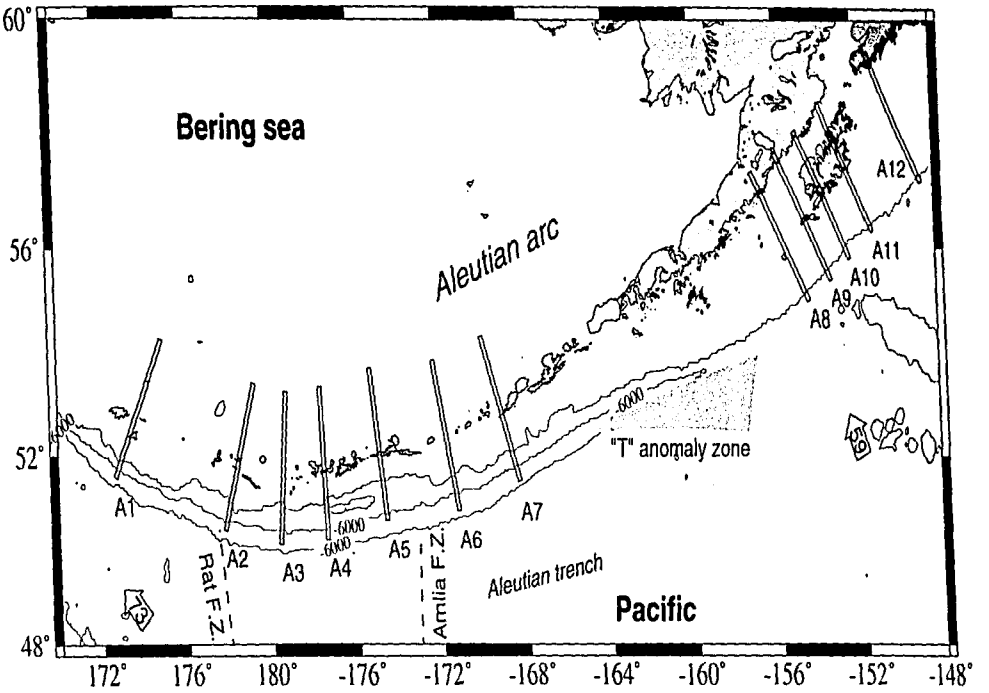
60°
56°
52°
48°
172°
176°
180°
-176°
-172°
-168°
-164°
-160°
-156°
-152°
-148°
Bering sea
Aleutian arc
Pacific
Aleutian trench
"T" anomaly zone
A1
A2
A3
A4
A5
A6
A7
A8
A9
A10
A11
A12
Rat F.Z.
Amlia F.Z.
6000
6000
6000
6000

Figure 2.

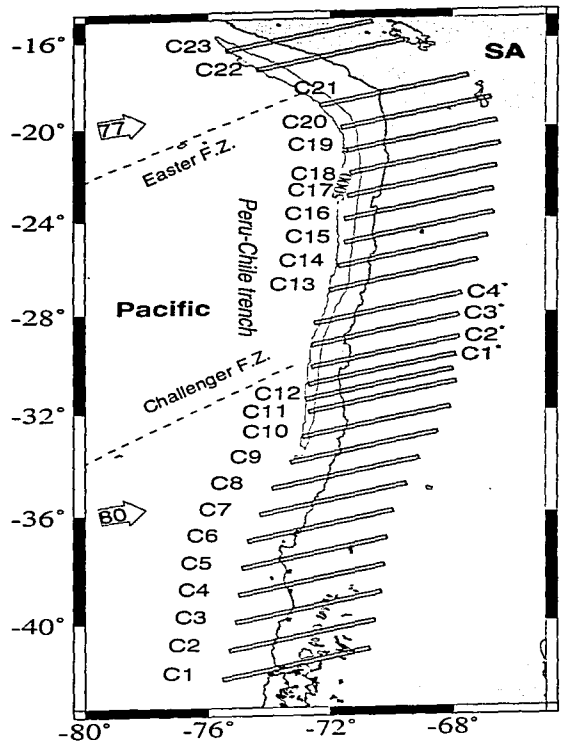
-16°
-20°
-24°
-28°
-32°
-36°
-40°
-80°
-76°
-72°
-68°
SA
Pacific
Peru-Chile trench
Easter F.Z.
Challenger F.Z.
77
80
C23
C22
C21
C20
C19
C18
C17
C16
C15
C14
C13
C12
C11
C10
C9
C8
C7
C6
C5
C4
C3
C2
C1
C4'
C3'
C2'
C1'

Figure 3.

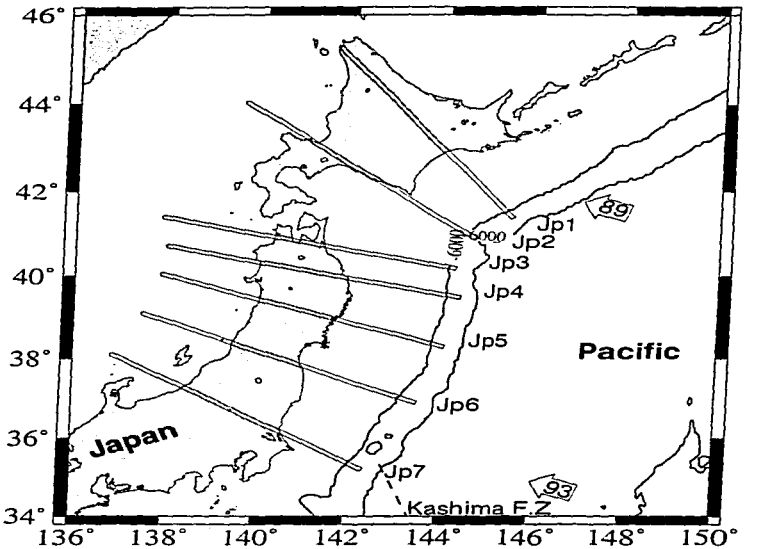
46°
44°
42°
40°
38°
36°
34°
136°
138°
140°
142°
144°
146°
148°
150°
Jp1
Jp2
Jp3
Jp4
Jp5
Jp6
Jp7
89
93
Kashima F.Z
Pacific
Japan

Figure 4.

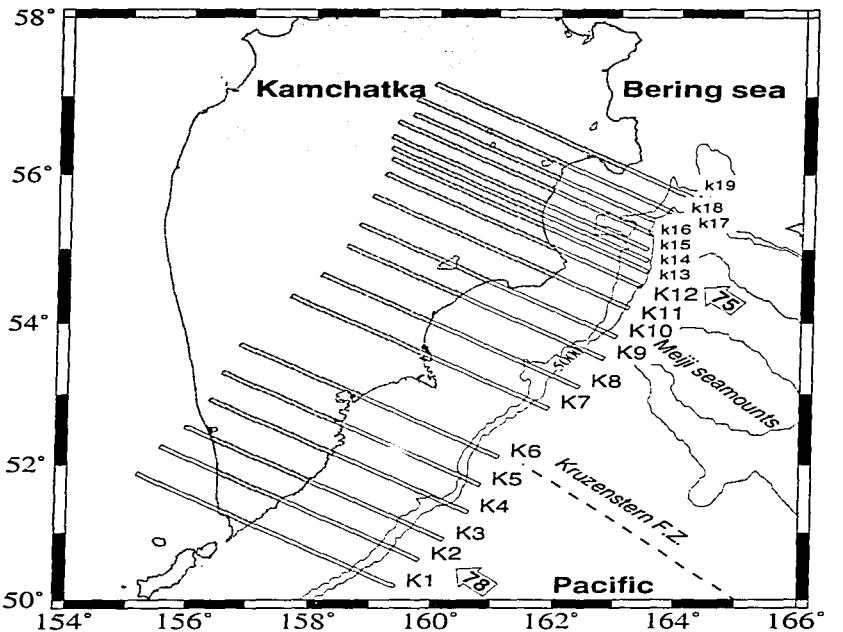
58°
56°
54°
52°
50°
154°
156°
158°
160°
162°
164°
166°
Kamchatka
Bering sea
Pacific
k19
k18
k17
k16
k15
k14
k13
K12
K11
K10
K9
K8
K7
K6
K5
K4
K3
K2
K1
75
78
Meiji seamounts
Kruzenstern F.Z.

Figure 5.

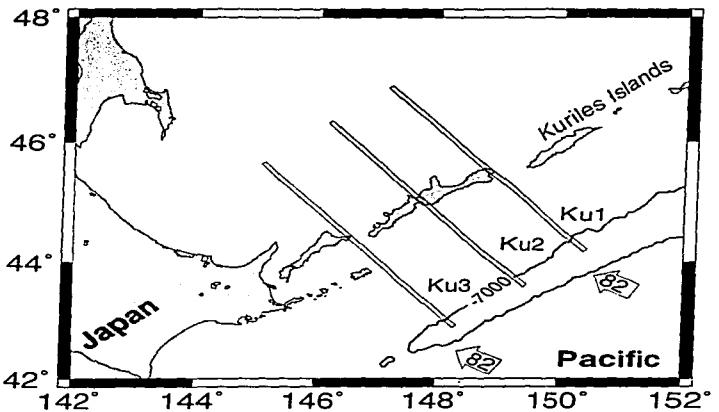
48°
46°
44°
42°
142°
144°
146°
148°
150°
152°
Kuriles Islands
Ku1
Ku2
Ku3
-7000
82
82
Japan
Pacific

Figure 6.

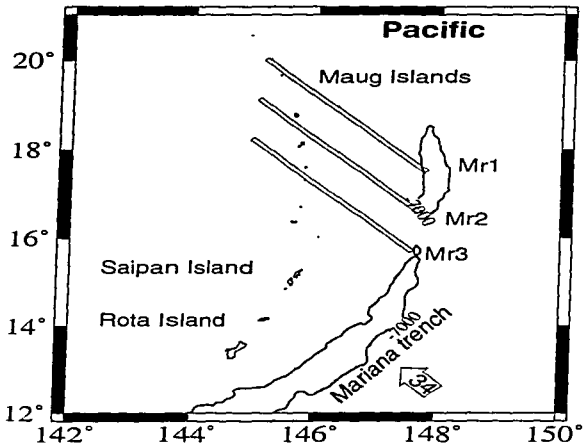
Pacific
20°
18°
16°
14°
12°
142°
144°
146°
148°
150°
Maug Islands
Mr1
Mr2
Mr3
Saipan Island
Rota Island
-2000
-2000
Mariana trench

Figure 7.

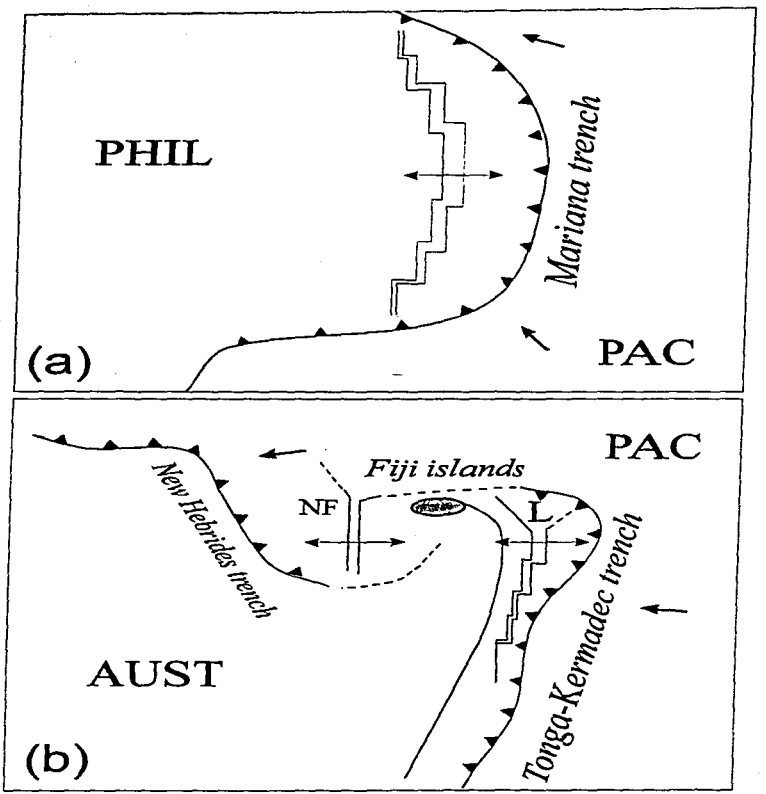
PHIL
Mariana trench
(a)
PAC
PAC
Fiji islands
NF
L
New Hebrides trench
AUST
Tonga-Kermadec trench
(b)

Figure 8.

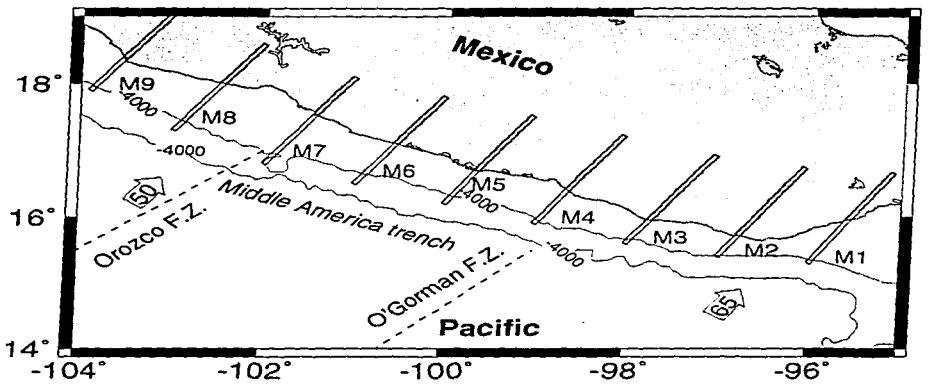
Mexico
M9
M8
M7
M6
M5
M4
M3
M2
M1
-4000
-4000
-4000
-4000
Middle America trench
Orozco F.Z.
O'Gorman F.Z.
Pacific
18°
16°
14°
-104°
-102°
-100°
-98°
-96°

Figure 9.

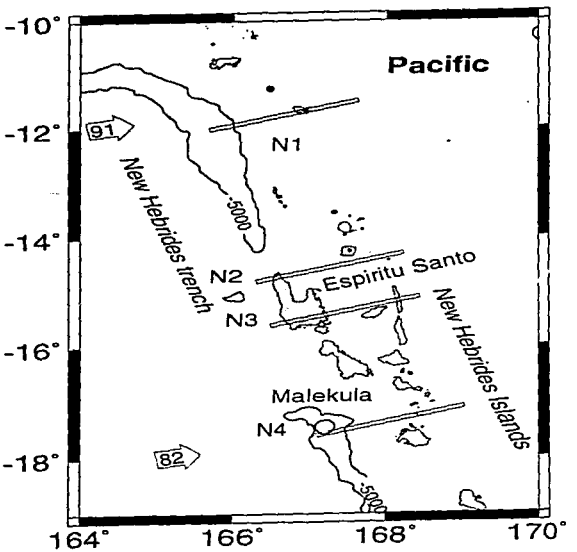
-10°
-12°
-14°
-16°
-18°
164°
166°
168°
170°
Pacific
91
N1
New Hebrides trench
-5000
N2
N3
Espiritu Santo
New Hebrides Islands
Malekula
N4
92
-5000

Figure 10.

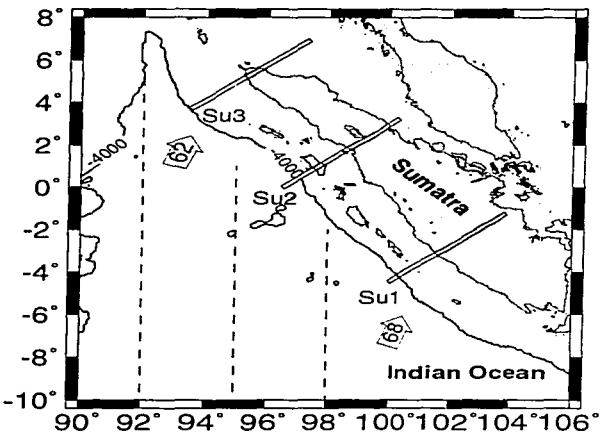
8°
6°
4°
2°
0°
-2°
-4°
-6°
-8°
-10°
90° 92° 94° 96° 98° 100° 102° 104° 106°
Su3
Su2
Su1
-4000
-4000
62
68
Sumatra
Indian Ocean

Figure 11.

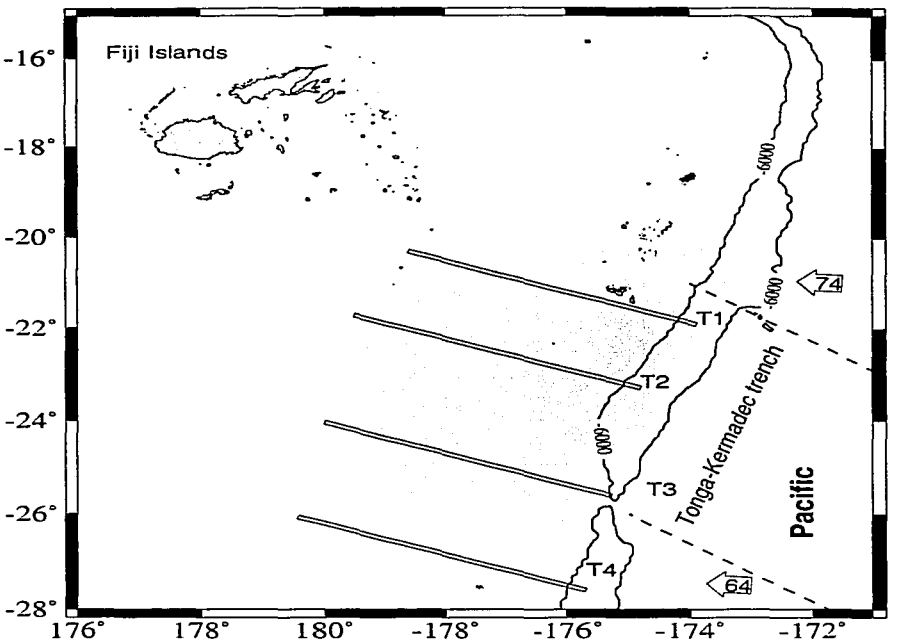
Fiji Islands
-16°
-18°
-20°
-22°
-24°
-26°
-28°
176°
178°
180°
-178°
-176°
-174°
-172°
-6000
-6000
-6000
T1
T2
T3
T4
74
64
Tonga-Kermadec trench
Pacific

Figure 12.

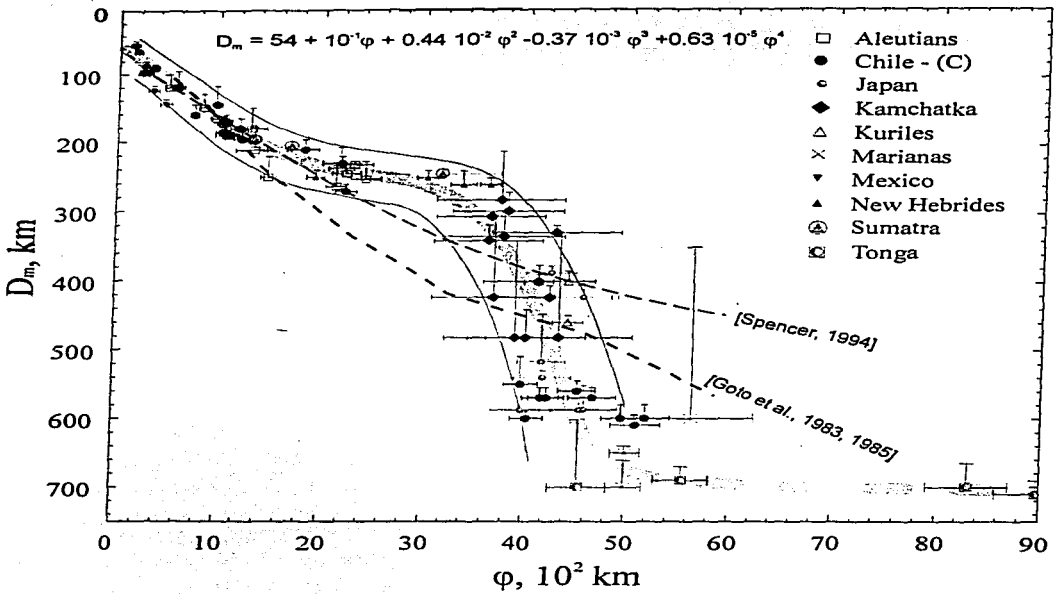
$D_m = 54 + 10^{-1}\varphi + 0.44\ 10^{-2}\ \varphi^2 - 0.37\ 10^{-3}\ \varphi^3 + 0.63\ 10^{-5}\ \varphi^4$
Aleutians
Chile - (C)
Japan
Kamchatka
Kuriles
Marianas
Mexico
New Hebrides
Sumatra
Tonga
[Spencer, 1994]
[Goto et al., 1983, 1985]
D_m, km
φ, 10^2 km
0
100
200
300
400
500
600
700
0
10
20
30
40
50
60
70
80
90

Figure 13.

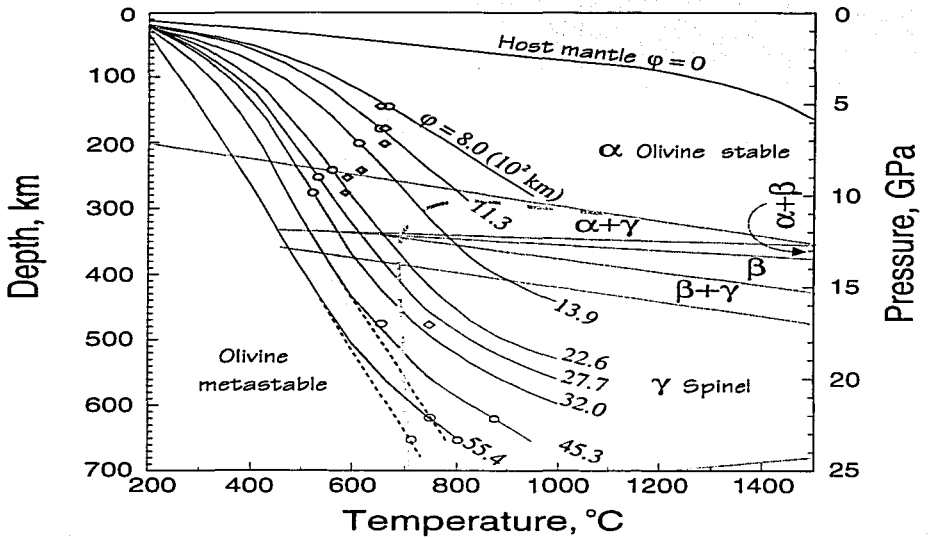
Depth, km
Pressure, GPa
Temperature, °C
Host mantle φ = 0
φ = 8.0 (10³ km)
α Olivine stable
α+γ
α+β
β
β+γ
γ Spinel
Olivine
metastable
11.3
13.9
22.6
27.7
32.0
45.3
55.4
0
100
200
300
400
500
600
700
5
10
15
20
25
200
400
600
800
1000
1200
1400

Figure 14.

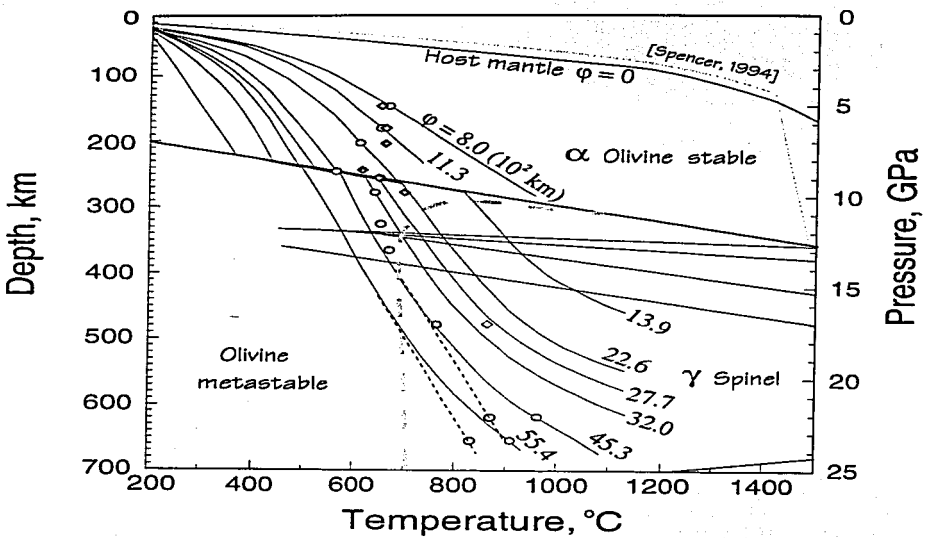
Depth, km
Pressure, GPa
Temperature, °C
Host mantle φ = 0
[Spencer, 1994]
φ = 8.0 (10³ km)
11.3
α Olivine stable
13.9
22.6
27.7
32.0
45.3
55.4
γ Spinel
Olivine
metastable
0
100
200
300
400
500
600
700
5
10
15
20
25
200
400
600
800
1000
1200
1400

Figure 15.

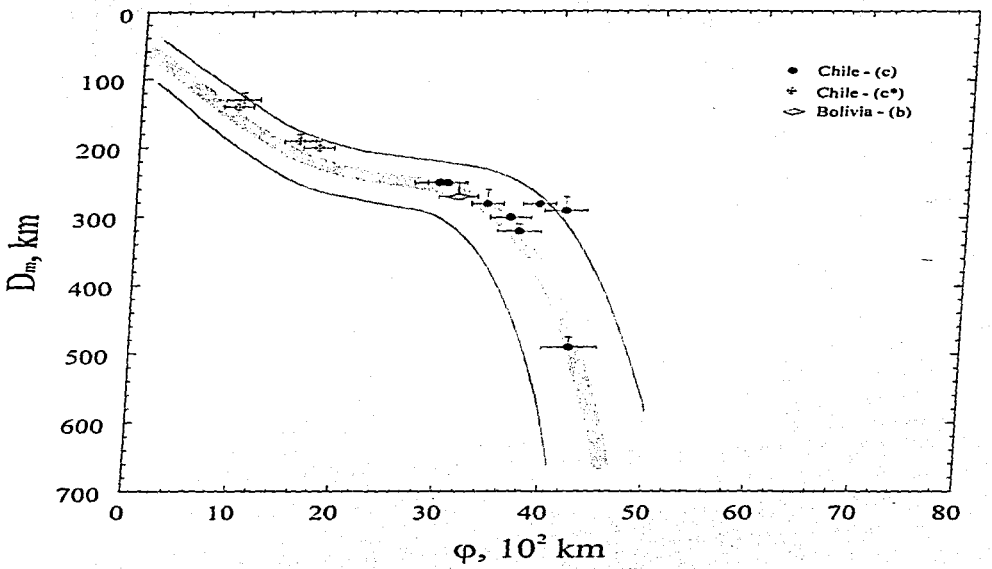
0
100
200
300
400
500
600
700
D_m, km
0
10
20
30
40
50
60
70
80
φ, 10^2 km
Chile - (c)
Chile - (c*)
Bolivia - (b)

Figure 16.

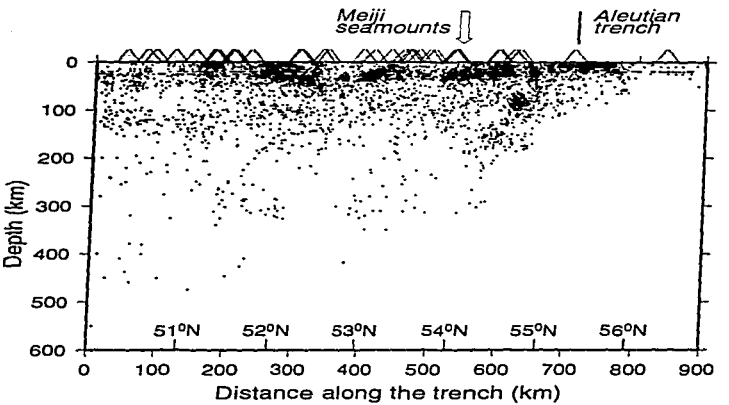
Meiji seamounts
Aleutian trench
0
100
200
300
400
500
600
Depth (km)
51°N
52°N
53°N
54°N
55°N
56°N
0
100
200
300
400
500
600
700
800
900
Distance along the trench (km)

Figure 17.

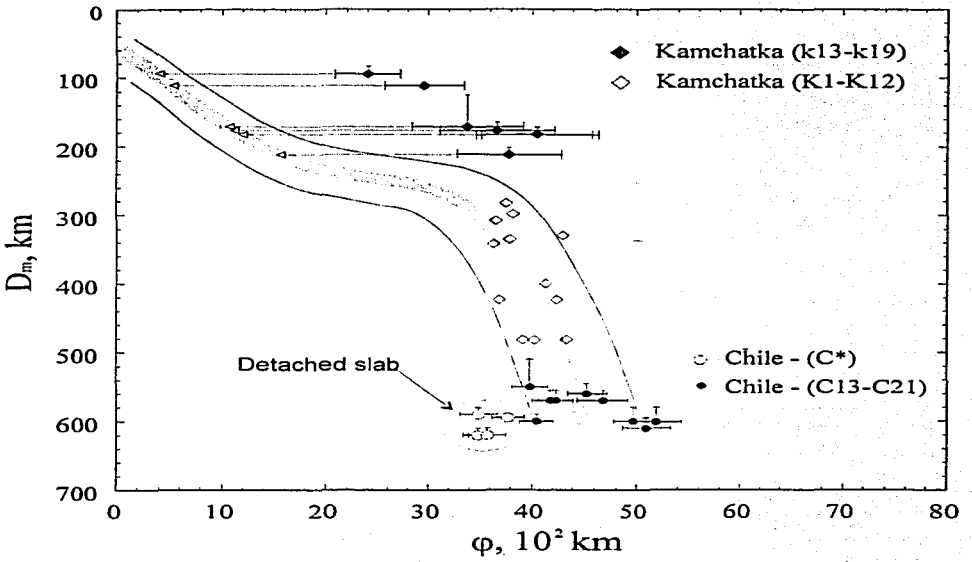
Kamchatka (k13-k19)
Kamchatka (K1-K12)
Chile - (C*)
Chile - (C13-C21)
Detached slab
D_m, km
φ, 10^2 km
0
100
200
300
400
500
600
700
0
10
20
30
40
50
60
70
80

Figure 18.

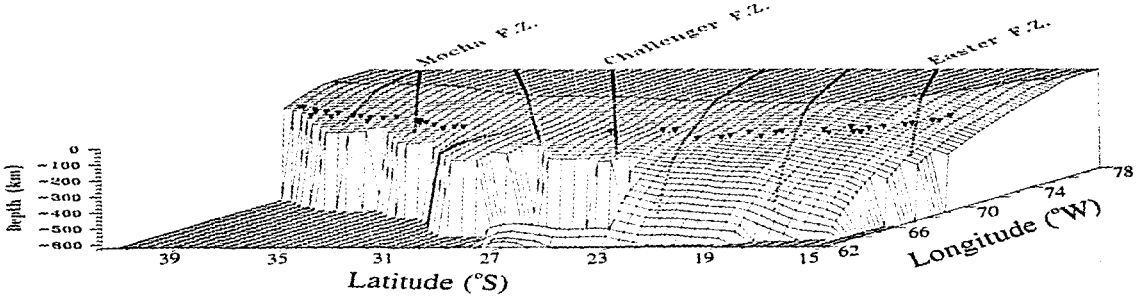
Mocha F.Z.
Challenger F.Z.
Easter F.Z.
Depth (km)
0
~100
~200
~300
~400
~500
~600
39
35
31
27
23
19
15
62
66
70
74
78
Latitude (°S)
Longitude (°W)

Figure 19.

III. Sismicidad y estructura de la zona de subducción de Kamchatka

(Aceptado en: *J. Geophys. Res.*, MS#96JB03491, Noviembre 7, 1996)

Seismicity and structure of the Kamchatka subduction zone

A. Gorbatov, V. Kostoglodov, and G. Suárez

Instituto de Geofísica, Universidad Nacional Autónoma de México, México D.F., México.

E. Gordeev

Geophysical Service, Academy of Sciences of Russia, Petropavlovsk-Kamchatsky, Russia.

Abstract. The configuration of the Pacific plate subducted beneath the Kamchatka peninsula and the stress distribution in the Kamchatka subduction zone (KSZ) were studied using the catalog of the Kamchatka regional seismic network, focal mechanism solutions estimated from P-wave first motions, the formal inversion of long-period waveforms, and centroid moment tensor solutions. To the south of ~55°N, the slab shows an approximately constant dip angle of ~55°. To the north of ~55°N, the dip of the slab becomes shallower reaching ~35°. The maximum depth of seismicity, D_m, varies from ~500 km depth near 50°N to ~300 km depth at ~55°N. The volcanic front is almost linear along the main part of the KSZ whereas it is sharply shifted landward to the north of ~55°N. The variation of D_m is apparently consistent with the standard empirical relation $D_m = f(\varphi)$, where φ is the thermal parameter of the subducted slab. To the north of ~55°N, the slab is offset toward the northwest and it is sharply deformed in a narrow contorted zone which is ~30 km wide (~56°N, ~161°E). To the north of this contortion, D_m decreases to ~100 km. The landward shift of the northern part of the slab is reflected by a sharp deviation of the volcanic front to the northwest which follows the ~90-160 km isodepth range of the subducted slab. The observed value of D_m in the northern segment significantly diverges from the global relation $D_m = f(\varphi)$. We interpret this as an effective decrease of the thermal thickness of the subducted lithosphere.

Introduction

The Kamchatka peninsula is an active margin where the Pacific plate (PAC), of Cretaceous age [*Rea et al.*, 1993] subducts beneath the North American plate. The relative plate motion changes from underthrusting of the PAC at the Kuril-Kamchatka arc to essentially strike-slip motion along the Aleutian arc, at the junction

of the Kamchatka and Aleutian trenches. The subduction process is accompanied by a chain of active volcanoes along the Kamchatka subduction zone (KSZ). There are two bathymetric structures related to this subduction zone: the Meiji seamounts and Kruzenstern fracture zone. The Meiji seamounts, which are the northernmost segment of the Emperor seamounts chain, enter the Kamchatka trench at ~54°N (Figure 1). This is the most prominent bathymetric feature being subducted. The other bathymetric structure, the Kruzenstern fracture zone, subducts at ~52°N.

The Kamchatka subduction zone is important in the understanding of convergent margins. Here, the subducted slab is one of the oldest in the world and there is a sharp contortion in the subduction geometry. These drastic changes in dip angle are reminiscent of those occurring in younger subduction environments. As in other regions, the sharp changes in the subduction geometry have important corresponding effects on the geometry of the volcanic arc. In spite of its relevance, the KSZ is poorly known. No systematic analysis of the larger teleseismic events has been undertaken, except a number of events analyzed by *Kao and Chen* [1994], and the data from the regional network had been unavailable. Thus except for a few articles little has been published about this convergent margin.

Fedotov [1968] and *Fedotov et al.* [1985] first studied the distribution of shallow and intermediate depth seismicity in Kamchatka, and determined a consistent and roughly planar structure of most of the Kamchatka seismic zone, except for a gradual shallowing of the dip angle to the north. Later, *Zobin* [1991] estimated the average stress distribution in the KSZ using the focal mechanism solutions obtained from P-wave first motion data of the regional seismic network. Although his results are not conclusive, the data suggest the presence of a double seismic zone. *Kao and Chen* [1994], using the results of waveform inversion of teleseismically recorded events, suggested that the double planed seismic zone in Kamchatka exists only to the south of ~53°N.

The hypocentral distribution of the earthquakes recorded by the Kamchatka Regional Seismic Network was reexamined recently, together with the focal mechanism solutions estimated from teleseismic data [*Gorbatov et al.*, 1994]. These results reveal a double-planed seismic zone developed from ~50°N to ~54°N; and possibly extending farther north, to ~56°N.

Further knowledge of the Wadati-Benioff seismic zone subduction geometry in Kamchatka are important to refine models relating subduction geometry and subduction of bathymetric features to upper-plate tectonics and volcanic activity [*e.g.*, *Pilger*, 1977; *Kelleher and McCann*, 1977; *Dickinson and Snyder*, 1978; *Chung*, 1979; *Cross and Pilger*, 1982; *Spence*, 1987; *Cahill and Isacks*, 1992; *Geist et al.*, 1993; *Gavrilov et al.*, 1994; *Kostoglodov and Ponce*, 1994]. Moreover, these facts are important for testing models that relate the shape of the subducted slab and the maximum depth of seismicity to geodynamic parameters of

the descending lithosphere, such as the age of the lithosphere and the rate of subduction [*e.g., McKenzie*, 1969; *Kostoglodov*, 1989; *Kirby et al.*, 1991, *Okal and Kirby*, 1995].

The main goals of the present study are: 1) to estimate the detailed structure of the Kamchatka Wadati-Benioff zone using the catalog of regional seismicity from 1964 to 1990 and all available teleseismic data. 2) to study the stress distribution and geometry of the subducted PAC. 3) to study the relation between the changes in the maximum depth of seismicity and the thermal parameter of the subducted slab in the KSZ. 4) to analyze the relation between the subduction geometry and subduction of bathymetric features to upper-plate tectonics and volcanic activity.

Data and methods of analysis

The regional seismic catalog

Regional and teleseismic data were used to define the configuration of the subducted PAC and the stress distribution within the Wadati-Benioff zone. The Kamchatka Regional Seismic Network (KRSN) consists of twenty eight, three-component short-period seismic stations (T_s=1.2 sec), and covers most of the Kamchatka peninsula (Figure 2 and Table 1). The catalog of seismicity registered by the regional network is available from 1962 to 1990. This catalog contains the hypocentral locations, errors in their determination, and the estimated magnitude of the events [*Fedotov et al.*,1964; *Gusev*, 1979].

Completeness of the catalog

To analyze the completeness and homogeneity of the catalog, the relations of log$N$ versus M_w and cumulative number of events versus time were considered (Figures 3a and 3b respectively). Here N is the number of events and M_w is the moment magnitude. The magnitude in the catalog of the KRSN is listed as a "klass", K^{F68}, [*Fedotov*, 1972]. The conversion from K^{F68} to M_w was done using the following equation [*Gusev*, 1991]:

$$M_w = 0.61\ K^{F68} - 2.17 \quad (3 \geq M_w \geq 6.5) \tag{1}$$

The log$N$ versus M_w plot shows a linear logarithmic decrease of the number of events for $M_w \geq 3.8$ with an average b-value of 0.98 (Figure 3a). This suggests that the catalog of the KRSN is complete for events with

$M_w \geq 3.8$. The plot of the cumulative number of events versus time shows an almost constant slope with the exception of two relatively small irregularities (in 1972 and 1983) marked as black arrows on Figure 3b. These two small changes in slope represent less than a ~2% change in the total number of reported events. There is no evidence that these irregularities correlate to any notable changes in the network operation; these small irregularities probably do not bias the homogeneity of the catalog.

The quality of hypocentral location

Unfortunately, the catalog from 1962 to 1990 does not include the arrival times of the phase data and, consequently, the number and distribution of seismic stations used to locate each event. Therefore, it is impossible to analyze the reliability of the hypocentral determination other than using the errors reported in the catalog (Figure 4a). *Gusev* [1974; 1979] analyzed the error estimates of hypocentral determination reported by the KRSN. These studies show that the average mean-square errors of the hypocentral determination of the KRSN are 15 km in depth, 6 km in longitude and 12 km in latitude [*Gusev*, 1974; 1979]. Fortunately, complete catalog including phase readings of ~2000 events exists for events that occurred between 1985 and 1987. These data offer the possibility to analyze in more details the quality of hypocentral determinations. Synthetic tests were applied to those events for which phase readings exist. The goal of these tests was to evaluate the maximum error of hypocentral determination caused by changes in the assumed earth structure and the network geometry. For this purpose, the hypocenters of the events recorded during 1985-1987 and the station sets that registered each event were used to generate synthetic travel times to which random noise was added. The added noise was normally distributed with a standard deviation of 0.2 s for P and 0.8 s for S waves. The events were then relocated using different velocity models applying a ±5% perturbation to the P-wave velocity model and to the Poisson ratio. Also, the depth of the Moho was taken at 30 and 40 km. It may be assumed that the quality of hypocentral location is reflected by the magnitude of the largest hypocentral deviation between the original location and the perturbed relocated hypocenter (Figures 4b and 5).

The synthetic tests show that the average maximum deviation of the hypocentral depth determination is 18 km and the average maximum epicentral deviation is 6 km. Maximum hypocentral deviations for the events with $M_w \geq 3.9$ are about half of those observed for the events with smaller magnitudes (Figure 4b). Shallow earthquakes (0-45 km depth) offshore and near the trench have larger hypocentral deviations (~40 km in depth and ~20 km in epicenter) than those located closer to the coast (~20 km in depth and ~5 km in epicenter) (Figure 5). Depending on the network coverage, the smallest hypocentral deviations (about 5 km)

are observed for events within a depth range of 45 to 200 km and located landward. The maximum hypocentral deviation increases as a function of depth and, for the events located deeper than 200 km, it is of ~20 km in depth and ~5 km in epicenter.

In conclusion, the hypocenters that define the slab geometry, the purpose of the present study, are generally located at depths greater than about 40 km and are inland or close to the coast. As discussed above, the hypocentral locations of these events were consistently the most stable regardless of the perturbations applied to the arrival time data or to the assumed Earth structure. The average maximum hypocentral deviation for events with $M_w \geq 3.9$ were usually less than ~15 km in depth and ~10 km in epicenter (Figure 4b), giving us confidence of the observed geometry and structure of the subducted slab. Although the synthetic tests have been applied only to events occurring between 1985 and 1987, we assume that these results are valid for the complete catalog. Thus, taking into account the analysis of the completeness of the catalog and supposing that the events with estimated errors in depth greater than 10 km (Figure 4a) are not reliable, we decided to exclude from the catalog all events with the $M_w \leq 3.8$ and for which the estimated error in depth was greater than 10 km.

Inversion of long-period P and S waves

To estimate the stress distribution in the KSZ and to constrain the depth of the upper surface of the descending slab, focal mechanisms were determined using teleseismic data. Events with magnitude $m_b \geq 5.5$ were selected to determine their focal mechanisms from the inversion of long-period body waves.

Digital seismic traces recorded by the Global Digital Seismograph Network (GDSN) and the digitized analog seismograms of the World-Wide Standardized Seismograph Network (WWSSN) were used for the body wave inversion. The teleseismic body wave inversion technique of *Nábelek* [1984] was used to determine the source parameters of 21 earthquakes (Figure 6 and electronic supplement[1]). Seismograms were selected for stations with epicentral distances in the range of 35° to 75° and all seismograms were normalized for a magnification of 1500 and an epicentral distance of 40°. The epicentral locations of the events reported by the KRSN catalog were used in the inversion, assuming that epicenters in these catalog are more accurate than those published by the ISC bulletin for the Kamchatka area [*Gusev*, 1974]. The arrival times were taken from short-period records, when available, or as reported by the ISC bulletin. The inversion determines the strike and dip of one fault plane and the rake of the slip vector, the centroidal focal source depth, the seismic

moment (M_o), and the shape of the source time function parameterized by a series of overlapping isosceles triangles [*Nábelek*, 1984].

A half-space source structure is assumed with P-wave velocity of 6.0 km/s, a Poisson ratio is of 0.25, and a density of 2.6×10^3 kg/m^3 beneath the seismic stations. A half-space source structure determined for the Kamchatka area by *Balesta et al.* [1985] was used at the source. Additionally, a water layer was included in the source structure model for offshore earthquakes according to the bathymetry above the epicenter. The inelastic attenuation along the propagation path is parameterized using t^*=1 s for P-waves and t^*=4 s for S-waves [*Langston and Helmberger*, 1975]. The focal mechanism, centroidal depth, seismic moment, and source time function were solved simultaneously in each iteration. For the less reliable solutions, the resulting formal errors are within ±10° for the fault strike, dip and rake, ± 1 km for the centroidal depth and ±20% for the seismic moment (Table 2).

The focal mechanism solutions

Harvard Centroid Moment Tensor Solutions (HCMTS) [*Dziewonski et al.*, 1981; *Dziewonski and Woodhouse*, 1983] were also used for the areas where the lack of events with $m_b \geq 5.5$, which can be used for body-wave inversion. Unfortunately, the northern part of the KSZ (north of ~54°N) does not have a sufficient number of events with appropriate magnitudes to perform a body-wave inversion or that are reported in the Harvard catalog. Therefore, P-wave first motions were used to estimate twelve focal mechanisms in this area using the data from the ISC Bulletin of Hypocenter Associated Phase & Comment Data from 1964 to 1987. Only stations with arrival time errors (RMS) smaller than 1.5 s were used. Stations with reported inverted polarities are corrected according to the *NEIC Semi-Annual Technical Report* [1990].

In total, twenty one focal mechanism solutions were estimated from the waveform inversion analysis, twelve solutions were constructed using the first motions of P-waves, and twelve mechanisms were taken from HCMTS (Table 2, Figure 7, and electronic supplement[1]). A comparison between the focal depth estimates for the events modeled in this study (Table 2) using the body-wave inversion, D_i, and the depths of the same events reported by the KRSN, D_l, is shown on Figure 8. The uncertainties of the depth values reported by the KRSN are shown as error bars. The best fit linear dependence D_l against D_i (dashed line in Figure 8) is D_l=1.01(±0.03)D_i+ 4.05(±4.1). The average standard deviation of D_l predicted from D_i is ±15 km. Not surprisingly, the best agreement between D_l and D_i is within the depth range from ~70 to ~300 km (Figure 8). Several events that are shallower than ~70 km or deeper than ~300 km have larger differences

(more than ~15 km) in focal depth estimates (Figure 8). These results are similar to those obtained in the hypocentral location quality test realized above.

Geometry of the subducted Pacific plate and its stress distribution

Seismicity profiles

In order to perform a detailed analysis of the spatial distribution of earthquakes beneath the Kamchatka peninsula, the selected catalog of hypocenters reported by the KRSN (M_w>3.8 and depth error smaller than 10 km) were projected on twenty vertical cross-sections AA' to MM' oriented normal to the trench and on profile ZZ' which is oriented along the strike of the trench (Figure 9). Profiles AA' to MM' have widths of 40 km, whereas NN' to TT' have widths of 20 km in order to examine in more detail the change of the dip angle of the slab in the northern part of the KSZ.

The hypocentral distribution of earthquakes along the Kurile-Kamchatka trench projected onto profile ZZ' shows a gradual decrease of the maximum depth of seismicity, D_m, from ~500 km near 50°N to ~300 km near 54°N (Figures 10). An abrupt change of D_m (from approximately 300 km to 200 km) is observed where the Meiji seamounts are subducted. Near the Aleutian arc, a diffuse shallow seismicity is apparently related to the strike-slip motion observed in that zone. The configuration of the downgoing plate in the Aleutians can not be defined because of the sparse distribution of seismicity. The average dip angle of the subduction zone of ~55° is constant from profile AA' to MM' (Figure 11).

Curves approximating the upper boundary of the subducted slab were traced on the profiles (Figure 11). The curve origin was set at the trench and it passes through the interplate contact, which is identified by the hypocenters of events showing thrust mechanisms. The curves obtained from these profiles were used to construct the isodepth contours of the subducted slab (Figure 12). The isodepth lines were selected at depths of 40, 60, 80, 100, 140, 180, 300, 400 and 500 km. All isodepth contours were smoothed using a polynomial interpolation. The relatively sharp change in the shape of the subducted slab and the dip angle begin near profile NN' (Figures 11, 12 and 13). The zone of rapid change in the dip of the slab is located between profiles OO' and PP' (Figures 13). The slab on profile PP' is offset with respect to that on profile OO' by about 20 km. This deviation takes place without a prominent change of D_m or dip angle of the slab. Farther north, D_m decreases from ~180 km (profile PP') to ~100 km, on profile TT', and the dip angle decreases from ~55° to ~35°.

Stress distribution in the downgoing plate

Intraplate down-dip tensional earthquakes are observed from ~50°N to ~56°N (Events number 2, 4, 24, 27, 28, 29, 30, 37, 39, 45 on Figure 11); these mechanisms probably indicate the presence of a double-planed seismic zone along practically the entire KSZ. *Gorbatov et al.*, [1994] showed that the maximum depth of the double seismic zone is ~180 km. The zone of interplate seismogenic coupling is defined by the change from interplate thrust to down-dip compressional events at the depth of ~60 km [*Gorbatov et al.*, 1994].

Events number 18 and 44, showing down-dip tensional mechanisms are unusual given their hypocentral location (Figure 11). These events occur in the region where thrust events take place at a depth of about 50 km. Events number 6, 8 and 15 (Table 2 and Figure 7) indicate right lateral strike-slip motion along the Aleutian trench as predicted by the relative motion of the Pacific and North American plates.

Maximum depth of seismicity and the age of the subducting slab

It was shown above that the maximum depth of seismicity, D_m, decreases gradually from ~500 km (50°N) to ~300 km (54°N) (Figure 10). The steep change of D_m from ~300 km to ~200 km occurs at 54.5°N, where the Meiji seamounts chain enter the subduction zone. In order to investigate the origin of this change a dependence of D_m against φ for KSZ is analyzed, where $\varphi = V A \sin\alpha$ is the "thermal parameter" of the descending slab [*Kirby et al.*, 1991], A is the age of the plate, V is convergence velocity, α is subduction angle. The main idea is to compare the standard relationship $D_m = f(\varphi)$ with the data on D_m vs. φ for the KSZ. f is a global empirical estimate [*Kostoglodov* 1989; *Kirby*, 1991; *Kirby* 1995; *Kirby et al.*, 1996]. The estimates of f recently obtained from the analysis of different Wadati-Benioff zones [*Gorbatov et al.*, 1996] were used in the analysis. The dependence of D_m versus φ for a given subduction zone may differ significantly from the general empirical dependence $D_m = f(\varphi)$ if the parameters of subduction for the particular subduction zone are not known well or the subducted slab is inhomogeneous (bathymetric features having different physical properties).

To estimate D_m and α, profiles from AA' to TT' (Figure 11) and cross-section ZZ' (Figure 10) of the Wadati-Benioff seismic zone are used. The convergence rate and associated uncertainties are calculated from the NUVEL 1A model [*DeMets et al.*, 1994] at the location where the subduction trajectory of the point corresponding to D_m intersects the trench. The age of the subducted slab in $\varphi = V A \sin\alpha$ represents the age of

that segment of the oceanic plate now located at depth D_m when it first started to subduct. The relation by *Shiono and Sugi* [1985] is used to estimate A:

$$A = A_t + L_m/V_s - L_m/V \quad (2)$$

where V_s is the half-spreading rate, L_m is the length of down dip seismic activity along the subducting slab and A_t is the age of the oceanic plate at the trench. A_t and V_s are estimated using the isochrone lines of the Northern Pacific obtained by *Renkin and Sclater* [1988]. A correction [*Shiono and Sugi*, 1985] for the angle between the direction of profile and vector V is applied. L_m is measured along the seismicity profiles (Figure 11). An average dip angle, α, is calculated as $\arctan(D_m/L_s)$ where L_s is a projection of L_m on the Earth's surface.

Table 3 summarizes the estimates of D_m and φ together with the assessments of their uncertainties for the analyzed profiles. The uncertainty of D_m, δD_m, is estimated as the separation between the deepest event and next deepest event for each profile. The uncertainty in the average dip angle, $\delta\alpha$, is then determined from the uncertainty in D_m. The error of A, σA, is assessed using the uncertainty of age estimates by *Renkin and Sclater* [1988]. For the Pacific plate subducting beneath Kamchatka (87-105 m.y.) this uncertainty is not more than 10 m.y. [*Renkin and Sclater*, 1988]. Uncertainties in A_t and V_s are the main contribution to the error of A (see equation 2). σA is calculated as a result of the error propagation in equation (2). It should be noted that for the following analysis a relative changes of D_m and φ are only important. Because we applied the same value of uncertainty of 10 m.y. and the same calculation procedure to obtain σA for all profiles, the main component of σA can be considered as a systematic error for that group of profiles. It means that a relative change of φ has a significantly smaller random error.

The results of D_m and φ presented in Table 3 are compared with the general empirical dependence $D_m = f(\varphi)$ [*Gorbatov et al.*, 1996] (Figure 14). For most of the profiles in the southern part of the Kamchatka peninsula, the observed values of D_m fit the empirical curve $D_m = f(\varphi)$ (Figure 14) except for profile GG'. Profile GG' coincides spatially with the subduction of the Kruzenstern fracture zone, which apparently alters the seismic regime and perturbs D_m in that area, as observed for different topographic features in other subduction zones [*e.g. Chung and Kanamori*, 1978]. We should note that subduction parameters and age estimates of *Renkin and Sclater* [1988] are fairly reliable. Furthermore, the upper Cretaceous age estimated

from DSDP site 192 [*Creager et al.*, 1973] is in agreement with the isochrone of 90 m.y. of *Renkin and Sclater* [1988] at the drilling site.

In the northern part of the KSZ (profiles OO' - TT') the observed values of D_m are significantly smaller than those predicted by the general empirical relation. That sharp decrease of the maximum seismic depth is observed to the north of the area where the Meiji seamounts enter the trench (Figure 10). The convergence rate, dip angle, and D_m are well constrained for profiles NN' to TT'; those profiles correspond to a relatively old segment of the Pacific plate (A_t ~ 86 m.y.) and there is no evidence of abrupt changes of the seafloor age for the KSZ [*Creager et al.*, 1973, *Lonsdale*, 1988, *Rea et al.* 1993]. Nevertheless, for the assessed values of φ the observed values of D_m are anomalously shallow. In order to fit the general empirical curve, the age of the Pacific plate in that zone should be about two to three times younger (A_t ~ 25-55 m.y.) than the age reported by *Renkin and Sclater* [1988] (Table 4).

Heat flow data of *Smirnov and Sugrobov* [1979; 1980a,b] suggest that the thermal thickness of the subducted plate (the depth of the 1200°C isotherm) is two to three times less to the north of the Meiji seamount chain axis than that to the south of it. Thus the reduced thermal thickness of the subducted plate near profiles NN', OO', PP', QQ', RR', SS', and TT' corresponds to a lower effective age than the geologic age of the PAC estimated by *Renkin and Sclater* [1988] (Table 4 and Figure 14).

Intraplate island-seamount chains represent density anomalies in oceanic plates [*e.g.*, *Cross and Pilger*, 1982; *Nur and Ben-Avraham*, 1983; *Geist et al.*, 1993]. A difference in relative buoyancy between normal oceanic lithosphere and a seamount chain may arise from a difference in their thermal thicknesses or effective ages. Thinner lithosphere of the Meiji seamount chain subducts at a lower angle than old normal lithosphere at the KSZ, as has been observed for other island-seamount chains subduction [*e.g.*, *DeLong and Fox*, 1977; *Molnar and Atwater*, 1978].

The contortion zone and the shift in the volcanic arc

To analyze the contortion zone located near ~55°N, profiles NN', OO', PP', and QQ' were combined into a wider cross-section NQ (Figure 15). The hypocenters with focal depths of less than ~100 km on the four superimposed profiles, form a wide seismic band (Figure 15a). At depths greater than ~100 km, the seismic pattern splits into two seismic sheets. The lower sheet correspond to the main part of the subducted slab which dips at an approximately constant angle of ~55° from ~50°N to ~54°N. The upper sheet corresponds to the shifted segment (Profiles PP' to TT' on Figure 11). On the frontal view of cross-section NQ (Figure 15b), a clear circular hypocentral concentration of ~40 km in diameter is observed at depths from ~60 km to ~100

km. It is interesting to note that the change in dip between these two seismic sheets starts below this hypocentral concentration.

Focal mechanism solutions were determined for nine events in the contortion zone (events 7, 24, 26, 27, 28, 29, 30, 32 and 33 in Table 2 and Figure 16). For all of these earthquakes, except event number 7, (Table 2 and Figure 16), the nodal planes of the focal mechanism solutions strike in a direction which is approximately parallel to the strike of the slab (Figure 16), suggesting that these events are not directly related with an anomalous stress distribution produced by the contortion of the subducting plate. Event number 7 is located in the zone of hypocentral concentration where the two seismic sheets are offset. In plan view (Figure 16), the nodal planes of this event focal mechanism is perpendicular to the isodepth curves and oriented along the contortion zone. This mechanism may represent scissor-type faulting occurring along the contortion zone.

The volcanic front in Kamchatka lies about 200 to 250 km landward from the trench axis. According to the configuration of the subducted slab obtained in this study, the volcanic front from ~50°N to ~54°N coincides with a depth of the subducted slab of about 90 to 140 km (Figure 12). To the north of 56°N, the volcanoes Klyuchevskoy and Sheveluch (Figures 12 and 16) are shifted (~100 km) to the west of the main axis of the volcanic front. Although *Tatsumi et al.* [1994] suggested that Klyuchevskoy and Sheveluch volcanic groups are related to a second, backarc-type volcanic activity, these volcanoes follow the isodepth contours of the slab corresponding to depths of ~90 to ~160 km, which is approximately of the same range as that for the main volcanic front. Furthermore, isotopic analyses [*Vinogradov et al.*, 1986], water and fumarole gases [*Taran et al.*, 1987], geochemical analysis [*Kersting and Arculus*, 1994], and the distribution of the trace and minor elements [*Popolitov and Volynets*, 1982] in lavas of the Klyuchevskoy and Sheveluch volcanoes show that the lava genesis apparently occurs at approximately the same depths as those of the volcanoes of the main volcanic front and are directly related to the subduction process. These results suggest that the Sheveluch and probably Klyuchevskoy volcanic groups belong to the volcanic front, which is shifted to the northwest from the main axis of the volcanic front due to the lower subduction angle in the northern part of the KSZ.

Discussion and conclusions

The seismotectonics and structure of the Kamchatka subduction zone was studied using a dataset of regional (from 1964 to 1990), and teleseismic earthquakes. The KSZ may be subdivided into two parts: the main southern part (from ~50°N to ~55°N) and the northern shifted segment. The southern part of the

subducting slab shows an average dip angle of ~55°. The maximum seismic depth, D_m, varies smoothly from ~500 km (~50°N) to ~300 km (~55°N).

In the area to the north of the Meiji seamounts the subducted slab is sharply deformed within a narrow zone of ~30 km width (~161°E,~56°N). The maximum depth of seismicity , D_m, abruptly decreases from ~300 km to ~200 km in that zone. Farther north from this contortion, the dip angle decreases from ~55° to ~35° and D_m decreases to ~100 km depth. The hypocentral distribution shows that the contortion of the slab begins at depth of ~100 km (Figure 15). A notable hypocentral concentration is associated with the shallowest section of the contortion zone.

An analysis of the relationship between volcanism in Kamchatka and the configuration of the subducted slab shows that the location of the main volcanic front corresponds approximately to the ~90-160 km isodepth limits of the upper surface of the slab, which is common for subduction zones [*Cross and Pilger*, 1982]. The volcanic front is almost linear for the main part of the KSZ (from ~50°N to ~55°), where the dip angle of the subducted slab is constant. From ~55°N to ~56°N, the shift of the northern segment of the subducted slab and change of the dip angle from ~55° to ~35° produces the deviation of the volcanic front to the northwest following the ~90-160 km isodepth range of the surface of the subducted slab (Figure 12).

The variation of the maximum depth of seismicity in the main part of the KSZ is apparently consistent with the global empirical dependence $D_m = f(\varphi)$, whereas the observed D_m in the northern shifted segment of the subducted slab (from ~55°N to ~56°N) diverges from this general relation. To the north of the area where the Meiji seamounts enter the trench, D_m becomes significantly shallower than the average estimates of the maximum depth of seismicity in other subduction zones with similar values of the thermal parameter, $\varphi = V A \sin\alpha$. A plausible explanation of the anomalously low values of D_m is the lower effective age (or thermal thickness) of the lithosphere.

The Meiji seamount subduction is an important factor which changes the subduction regime of the PAC in the KSZ. That manifests in the change of dip angle, shallower seismicity, and shifted volcanic front in the northern part of the Kamchatka subduction zone.

Acknowledgments. We wish to thank A. Gusev and Yu. Taran for useful discussions and suggestions. Essential critical comments and recommendations were made by G. Abers, L. Astiz, and one anonymous reviewer. The GMT-System software by P. Wessel and W. Smith was utilized in this study.

References

Balesta, S. T., and L. I. Gontovaya, The seismic model of the Earth's crust in the Asiatic-Pacific transition zone (in Russian), *Volcanology and Seismology, 4*, 83-90, 1985.

Cahill, T. and B. L. Isacks, Seismicity and shape of the subducted Nazca plate, *J. Geophys. Res., 97, B12*, 17503-17529, 1992.

Chung, W. Y. and H. Kanamori, Tectonic anomalies in aseismic ridges subduction in the New Hebrides arc, *Tectonophysics, 50*, 29-40, 1978.

Chung, W. Y., A seismological investigation of the subduction mechanism of aseismic ridges (part 2), Ph.D. thesis, 197 pp., Ca. Inst. of Tech., Pasadena, 1979.

Creager, J. S., D. W. Scholl, et al., Initial Reports of the Deep Sea Drilling Project, v. 19, 913 pp., U.S. Government Printing Office, Washington, 1973.

Cross, T. A. and R. H. Pilger Jr., Controls of subduction geometry, location of magmatic arcs, and tectonics of arc and back-arc regions, *Geol. Soc. Am. Bull., 93*, 545-562, 1982.

DeLong, S. E., and P. J. Fox, Geological consequences of ridge subduction, in *Island arcs, deep sea trenches and back-arc basins*, edited by M. Talwani and W. C. Pitman III, pp. 115-122, Am. Geophys. Union, Maurice Ewing Ser. 1, 1977.

DeMets, C., R. G. Gordon, D. F. Argus, and S. Stein, Effect of recent revisions to the geomagnetic reversal time scale on estimates of current plate motions, *Geophys. Res. Lett., 21, 20*, 2191-2194, 1994.

Dickinson, W. R. and W. S. Snyder, Plate tectonics of Laramide Orogeny, *Geol. Soc. Am. Mem., 151*, 355-366, 1978.

Dziewonski, A. M., T.-A. Chou, and J. H. Woodhouse, Determination of earthquake source parameters from waveform data for studies of global and regional seismicity, *J. Geophys. Res., 86*, 2825-2825, 1981.

Dziewonski, A. M., and J. H. Woodhouse, An experiment in the systematic study of global seismicity: Centroid-moment tensor solutions for 201 moderate and large earthquake of 1981, *J. Geophys. Res., 88*, 3247-3271, 1983.

Fedotov, S. A., I. P. Kuzin, and M. F. Bobkov, Detailed seismological studies in Kamchatka in 1961-1962 (in Russian), *Izv. Acad. Sci. USSR Geophys., 3*, 102-111, 1964.

Fedotov, S. A., On deep structure, properties of the upper mantle, and volcanism of the Kuril-Kamchatka island arc according to seismic data, Am.Geophys.Un., Geophys. Monogr., 12, 131-139, 1968.

Fedotov, S. A., Energy classification of the Kurile-Kamchatka earthquakes and the problem of magnitudes (in Russian), Moscow, Nauka, 111 pp., 1972.

Fedotov, S. A., A. A. Gusev, L. S. Shumilina, and G. V. Chernyshova, The seismofocal zone of Kamchatka (in Russian), *Volcanology and Seismology, 4*, 91-107, 1985.

Gavrilov, S. V., A. N. Boyko, and O. B. Aleksandrova, Lithosphere bending near the junction of the Aleutian and Kurile-Kamchatka trenches, *Phys. Solid Earth, 30, 1*, 26-30, 1994.

Geist, E. L., M. A. Fisher, and D. W. Scholl, Large-scale deformation associated with ridge subduction, *Geophys. J. Int, 115*, 344-366, 1993.

Gorbatov, A., G. Suárez, V. Kostoglodov, and E. Gordeev, A double-planed seismic zone in Kamchatka from local and teleseismic data, *Geophys. Res. Lett., 21, 16*, 1675-1678, 1994.

Gorbatov, A., V. Kostoglodov and E. Burov, Maximum seismic depth versus thermal parameter of subducted slab: application to deep earthquakes in Chile and Bolivia, *Geofísica Internacional, 35, 1*, 41-50, 1996.

Gusev, A. A., The errors of determination of parameters of earthquake foci in Kamchatka (in Russian), in *The properties of the upper mantle and their relation to volcanism in Kamchatka*, edited by S. A. Fedotov, pp. 66-81, Nauka, siberian branch of Ac. Sci. USSR, Novosibirsk, 1974.

Gusev, A. A., Computer determination of hypocenters of near earthquakes in Kamchatka (in Russian), *Volcanology and Seismology, 1*, 74-81, 1979.

Gusev, A. A., Intermagnitude relationship and asperity statistics, *Pageoph, 136, 4*, 515-527, 1991.

Kao, H., and W.-P. Chen, The double seismic zone in Kuril-Kamchatka: The tale of two overlapping single zones, *J.Geophys.Res., 99, B4*, 6913-6930, 1994.

Kelleher, J. and W. McCann, Bathymetric highs and the development of convergent plate boundaries, in *Island arcs, deep sea trenches and back-arc basins*, edited by M. Talwani and W. C. Pitman III, pp. 115-122, Am. Geophys. Union, Maurice Ewing Ser. 1, 1977.

Kersting, A. B., and R. J. Arculus, Klyuchevskoy volcano, Kamchatka, Russia: The role of high-flux recharged, tapped, and fractionated magma chamber(s) in the genesis of high-Al_2O_3 from high-MgO basalt, *J. Petrology, 35*, 1, 1-41, 1994.

Kirby, S., W. B. Durham, and L. A. Stern, Mantle phase changes and deep-earthquake faulting in subduction lithosphere, *Science, 252*, 216-225, 1991.

Kirby, S. H., Intraslab earthquakes and phase transition in subduction lithosphere, *U.S. Natl. Rep. Int. Union Geod. Geophys. 1990-1994, Rev. Geophys., 33*, 287-297, 1995.

Kirby, S. H., S. Stein, E. Okal, and D. Rubie, Metastable mantle phase transformations and deep earthquakes in subducting oceanic lithosphere, *Rev. Geophys., 34*, 261-306, 1996.

Kostoglodov, V. V., Maximum depth of earthquakes and phase transformation within the lithospheric slab descending in the mantle (in Russian), in *Physics and Interior Structure of the Earth*, edited by V. A. Magnitsky, Nauka, Moscow, 1989.

Kostoglodov, V. V., and L. Ponce, Relationship between subduction and seismicity in the Mexican part of the Middle America trench, *J. Geophys. Res., 99, B1*, 729-742, 1994.

Langston, C. A., and D. V. Helmberger, A procedure for modeling shallow dislocation sources, *Geophys. J. R. Astron. Soc., 42*, 117-130, 1975.

Lonsdale, P., Paleogene history of the Kula plate: offshore evidence and onshore implications, *Geol. Soc. Am. Bull.*, 733-754, 1988.

McKenzie, D. P., Speculations on the consequence and cause of plate motions, *Geophys. J. Roy. Astron. Soc., 18*, 1, 1-32, 1969.

Molnar, P., and T. Atwater, Interarc spreading and cordilleran tectonics as alternates related to the age of subducted oceanic lithosphere, *Earth and Planetary Sc. Lett., 41*, 330-340, 1978.

Nábelek, J. L., Determination of earthquake source parameters from inversion of body waves, Ph.D. thesis, 361 pp., Mass.Inst. of Tech., Cambridge, 1984.

NEIC semi-annual technical report, *Open File Report 90-267, 2, 1*, 35 pp., National Earthquake Information Center, U.S. Geol. Surv., Dept. of the Interior, 1990.

Nur, A. and Z. Ben-Avraham, Volcanic gaps due to oblique consumption of aseismic ridges, *Tectonophysics, 99*, 355-362, 1983.

Okal, E. A. and S. H. Kirby, Frequency-moment distribution of deep earthquakes; Implications for the seismogenic zone at the bottom of slabs, *Phys. Earth Planet. Inter., 92*, 169-187, 1995.

Pilger, R. H., Jr., Plate reconstruction, aseismic ridges and low-angle subduction beneath the Andes, abstract, *EOS, Am. Geoph. Un. Transactions, 58*, 1232, 1977.

Popolitov, E. I., and O. N. Volynets, Geochemistry of quaternary volcanic rocks from the Kurile-Kamchatka island arc, *J. Volcanol. Geotherm. Res., 12*, 299-316, 1982.

Rea, D., I. Basov, T. Janecek, E. Arnold, J. Barron, L. Beaufort, J. Bristow, P. de Menocal, G. Dubuisson, A. Gladenkov, T. Hamilton, L. Ingram, L. Keigwin, R. Keller, A. Kotilainen, L. Krissek, B. McKelvie, J. Morley, M. Okada, G. Olafson, R. Owen, D. Pak, T. Pedersen, J. Roberts, A. Rutledge, V. Shilov, H. Snoeckx, R. Stax, R. Tiedemann, and R. Weeks, Paleoceanographic record of north Pacific quantified, *EOS, Am. Geoph. Un. Transactions, 74, 36*, 406-411, 1993.

Renkin, M. L., and J. G. Sclater, Depth and Age in the North Pacific, *J. Geophys. Res., 93, B4*, 2919-2935, 1988.

Shiono, K., and N. Sugi, Life of an oceanic plate: cooling time and assimilation time, *Tectonophysics, 112*, 35-50, 1985.

Smirnov, Ya. B., and V. M. Sugrobov, Terrestrial heat flow in the Kurile-Kamchatka and Aleutian provinces. I. Heat flow and tectonics (in Russian), *Volcanology and Seismology, 1*, 59-73, 1979.

Smirnov, Ya. B., and V. M. Sugrobov, Terrestrial heat flow in the Kurile-Kamchatka and Aleutian provinces. II. The map of measured and background heat flow (in Russian), *Volcanology and Seismology, 1*, 16-31, 1980 a.

Smirnov, Ya. B., and V. M. Sugrobov, Terrestrial heat flow in the Kurile-Kamchatka and Aleutian provinces. III. Assessments of temperature at depth and thickness of the lithosphere (in Russian), *Volcanology and Seismology, 2*, 3-18, 1980 b.

Spence, W., Slab pull and the seismotectonics of subducting lithosphere, *Rev. Geophys., 25, 1*, 55-69, 1987.

Taran, Yu. A., T. P. Kirsanova, E. A. Vakin, A. D. Esikov, and A. L. Cheshko, Isotopic composition of water of fumarole gases of volcanoes of Kamchatka (in Russian), *Izv. Acad. Sci. USSR Geology, 9*, 124-127, 1987.

Tatsumi, Y., Y. Furukawa, T. Kogiso, Y. Yamanaka, T. Yokoyama, and S. Fedotov, A third volcanic chain in Kamchatka: thermal anomaly at transform/convergence plate boundary, *Geoph. Res. Lett., 21, 7*, 537-540, 1994.

Vinogradov, V. I., V. S. Grigoriev, and B. G. Pokrovsky, Isotopic composition of the oxygen and strontium in the rocks of the Kurile-Kamchatka island arc - key for some genetic constructions (in Russian), in *Evolution of the system Crust-Mantle*, edited by Yu. A. Shukolyukov, 78-102, Nauka, Acad. Sci. USSR, Moscow, 1986.

Zobin, V. M., Initial rupture and the main fault of earthquakes: a comparison of the body wave first arrivals and CMT data for the Kamchatka-Commander region, *Phys. Earth and Planet. Inter., 67*, 313-329, 1991.

Table 1. Catalog of Seismic Stations of the KRSN.

No.	Name	Longitude deg.	Latitude deg.	Period of operation, yr. from		to
1	APC	157.158	52.925	1986	-	
2	APH	160.840	56.000	1962	-	1988
3	AVH	158.738	53.265	1969	-	
4	BER	158.450	52.270	1963	-	
5	BKI	165.972	55.204	1963	-	
6	BLC	158.800	53.193	1976	-	1988
7	BLK	158.794	53.193	1976	-	1988
8	ESO	158.700	55.925	1965	-	
9	GNL	157.942	53.695	1988	-	
10	GRL	158.080	52.552	1980	-	
11	KBG	162.705	56.255	1968	-	
12	KLY	160.852	56.313	1961	-	
13	KMN	160.240	55.760	1990	-	
14	KPL	161.296	56.592	1986	-	
15	KRI	161.134	54.596	1966	-	
16	KRK	158.636	53.292	1975	-	1988
17	KRS	160.558	56.214	1987	-	
18	KRY	159.449	54.036	1968	-	
19	KZL	158.894	53.201	1976	-	1988
20	KZY	159.900	56.070	1961	-	
21	MED	167.566	54.786	1973	-	1974
22	MLK	158.630	54.700	1962	-	1964
22	MLK	158.630	54.700	1986	-	
23	NLC	159.345	53.171	1984	-	
24	OSS	163.060	59.250	1973	-	
25	OZR	160.392	54.692	1967	-	1969
26	PAU	156.810	51.467	1961	-	
27	PDK	160.780	56.140	1981	-	
28	PET	158.653	53.023	1961	-	
29	RUS	158.507	52.432	1987	-	
30	SKR	156.100	50.670	1952	-	
31	SML	159.975	54.108	1961	-	1976
32	SPN	160.011	53.107	1962	-	
33	SVL	161.225	56.583	1980	-	
34	TOP	158.041	53.230	1963	-	
35	UBL	156.308	52.842	1961	-	1964
36	VDP	160.220	55.770	1977	-	
37	VKM	158.473	54.627	1966	-	1971
38	ZLN	160.804	56.018	1988	-	

Table 2. Summary of Source Parameters.

Event[1]	Date UT	Origin Time[2]	Latitude[3] °N	Longitude[3] °E	Depth[4] km	Strike[5]	Dip[5]	Rake[5]	Magnitude[6]
				Modeled events					
1	March 18, 1964	0437:25.7	52.43	153.79	437±0.5	47±1.8	84±1.7	-63±1.9	6.1
2	Nov. 24, 1971	1935:28.5	52.77	159.66	95±0.9	165±2.7	10±2.1	40±2.7	7.1
3	May 27, 1972	0406:49.6	54.87	156.48	418±0.6	23±1.6	78±1.6	-93±5.6	5.7
4	July 23, 1975	1351:23.0	54.53	160.35	151±0.5	122±2.3	30±2.4	1±3.4	5.8
5	Sept. 21, 1977	2101:44.4	51.63	155.37	241±0.7	47±9.5	71±1.9	-89±9.8	6.1
6	Nov. 9, 1979	1345:46.7	55.66	164.12	31±0.4	76±2.7	54±1.2	50±2.2	5.6
7	March 22, 1980	1027:37.7	55.60	161.82	77±0.4	69±1.4	58±0.6	74±1.2	5.8
8	May 31, 1982	1021:16.8	55.07	165.48	14±0.8	204±1.2	63±2.4	3±1.4	6.3
9	Nov. 14, 1982	0829:20.6	52.84	158.98	88±0.2	47±1.2	73±1.1	-91±1.6	5.3
10	Jan. 5, 1983	0201:00.0	54.66	163.01	13±0.5	9±1.5	75±0.4	99±2.3	5.7
11	April 4, 1983	1904:22.1	52.95	160.02	57±0.3	23±1.1	56±0.3	101±0.8	5.7
12	July 24, 1983	2307:31.8	53.77	158.62	168±0.3	217±0.8	81±0.5	103±1.5	6.0
13	March 26, 1984	2312:36.0	56.34	162.95	22±0.3	84±1.9	67±1.0	91±3.4	5.2
14	July 27, 1984	1251:09.8	52.96	161.35	32±0.3	107±3.4	36±1.1	56±2.2	5.4
15	Dec. 28, 1984	1037:54.4	56.17	163.50	9±0.5	360±0.7	77±1.0	33±1.9	6.7
16	March 6, 1985	2231:51.9	55.09	162.48	44±0.2	34±1.4	59±0.3	95±1.3	5.6
17	May 19, 1985	0807:47.0	53.54	160.65	55±0.3	40±1.2	58±0.3	85±1.0	5.6
18	May 25, 1985	2329:22.0	53.95	161.14	56±0.4	232±1.1	51±0.2	-105±0.7	5.6
19	March 2, 1986	0314:43.2	51.47	157.43	96±0.2	19±1.3	65±0.5	-89±1.7	5.4
20	April 1, 1986	1340:45.9	54.44	161.96	56±0.2	60±1.4	56±1.3	79±1.0	5.4
21	May 2, 1986	1030:02.9	55.07	163.85	8±0.4	160±1.0	68±0.5	-124±1.0	6.0
				Mechanisms from first motion					
22	Nov. 11, 1964	1818:57.0	56.66	161.33	79	35	25	-90	5.2
23	Sept. 4, 1967	1930:12.9	54.5	159.62	170	71	80	-84	4.6
24	May 18, 1977	0357:14.5	55.61	160.87	160	35	77	83	5.0
25	Feb. 14, 1979	0104:35.9	55.12	158.86	303	227	29	-65	4.6
26	Nov. 13 1980	1951:39.1	55.57	161.73	80	150	53	44	5.4
27	Feb. 10 1982	0113:46.9	55.75	161.20	171	176	21	108	5.3
28	April 17, 1982	2037:09.7	55.71	161.27	165	7	90	90	5.3
29	April 25, 1983	2324:24.1	55.61	160.98	164	30	70	90	4.4
30	Oct. 1, 1983	2336:03.0	55.55	161.62	76	45	76	90	5.0
31	June 7, 1984	2155:16.5	54.50	159.72	157	63	85	-125	4.6
32	Nov. 14, 1984	1055:34.9	55.62	160.91	150	40	81	-90	4.6
33	April 23,1986	1008:58.9	56.12	160.83	179	37	79	-90	4.5
				Centroidal Moment Tensor Solution[7]					
34	Nov. 6, 1977	0239:36.9	53.50	159.96	60	36	18	109	5.1
35	Dec. 30, 1979	0418:32.1	52.37	152.52	550	245	16	-41	5.4
36	Oct. 13, 1981	1553:56.6	51.35	157.76	101	318	27	-117	5.3
37	Aug. 8, 1982	0614:09.4	50.69	157.20	117	279	14	164	5.1
38	Sept. 26, 1982	0109:28.6	50.27	158.62	31	235	55	-121	5.5
39	April 15, 1983	1451:58.0	53.30	160.64	30	184	38	47	5.8
40	June 1, 1984	0554:52.8	53.49	159.69	102	134	21	-176	5.2
41	April 16, 1987	0110:21.0	54.86	158.39	349	329	73	-57	5.0
42	July 6, 1987	2322:06.3	53.32	158.69	150	225	12	-93	5.2
43	Feb. 19, 1988	2237:10.5	52.78	158.25	112	132	13	-175	5.2
44	July 25, 1988	2342:34.0	50.92	158.00	42	101	24	-9	5.6
45	July 28, 1988	0358:17.7	50.80	157.35	104	297	53	-160	5.1

[1]Identification number of events.

[2]Values reported by the International Seismological Center (ISC).

[3]Epicenters reported by the Kamchatka Regional Seismic Network (KRSN).

[4]Focal depth obtained by the analysis of long-period waveform inversion and reported by the KRSN for the rest of events.

[5]Magnitude: M_w for the modeled events and m_b for the rest of events.

[6]Centroid moment tensor solutions of Harvard University [*Dziewonski et al.*, 1981; *Dziewonski and Woodhouse*, 1983].

[7]Focal mechanism parameters of modeled events are presented with corresponding formal errors determined in the inversion scheme.

Table 3. Summary of D_s Estimates and other Parameters Used for Thermal Parameter, φ, Calculation.

Prf	Lat °N	Lon °E	[1]Az_c deg	[2]V_c cm/yr	[3]Az_{cv} deg.	[4]V^*_c cm/yr	[5]α deg.	$\delta\alpha$	[6]D_s km	δD_s	[7]V_p cm/yr	[8]Az_{sp} deg.	[9]V^*_{sp} cm/yr	[10]A_s m.y.	[11]L_s km.	[12]A^s m.y.	φ 10^3km.	$\delta\varphi$
A	50.2	159.4	302	7.81	306.5	7.78	45.0	0.5	482	41	2.89	150	3.15	104.5	706	73.03	40.20	5.69
B	50.6	159.8	302	7.78	306.8	7.76	43.5	0.5	400	24	2.89	150	3.14	104.2	600	77.38	41.31	5.45
C	50.9	160.2	302	7.76	307.1	7.73	49.0	0.5	482	153	2.89	150	3.14	103.8	658	74.31	43.36	7.16
D	51.3	160.6	302	7.74	307.5	7.70	45.0	3.0	482	141	2.89	150	3.13	103.5	706	71.77	39.09	6.84
E	51.7	160.8	302	7.72	307.7	7.68	47.0	3.0	424	18	2.89	150	3.12	102.5	600	75.48	42.39	6.07
F	52.1	161.1	302	7.69	307.9	7.65	52.5	2.5	329	10	2.70	158	3.12	92.0	471	70.76	42.95	6.30
G	52.5	161.5	302	7.67	308.3	7.62	43.5	0.5	235	11	2.70	158	3.11	90.5	353	74.52	39.11	5.31
H	52.8	161.9	302	7.65	308.6	7.60	45.0	0.5	423	117	3.40	150	3.65	93.0	600	68.67	36.88	6.00
I	53.1	162.4	302	7.62	309.0	7.56	43.0	1.0	341	23	3.40	150	3.64	91.4	517	70.37	36.29	5.27
J	53.5	162.8	302	7.60	309.3	7.53	45.5	3.5	335	35	3.40	150	3.63	91.0	506	70.36	37.81	5.92
K	53.8	163.0	302	7.57	309.6	7.51	43.0	1.5	306	6	3.40	150	3.63	90.6	471	71.35	36.53	5.26
L	54.2	163.2	302	7.55	309.8	7.48	43.5	4.5	282	70	3.40	150	3.62	90.2	424	72.83	37.50	6.22
M	54.5	163.4	302	7.53	309.9	7.46	45.0	0.5	298	27	3.40	150	3.62	89.8	424	72.40	38.19	5.36
N	54.7	163.5	302	7.52	310.1	7.44	42.0	0.5	211	10	3.40	150	3.62	89.4	329	75.88	37.79	5.03
O	54.9	163.5	302	7.51	310.2	7.44	45.0	3.5	182	10	3.40	150	3.61	89.0	294	76.91	40.44	5.85
P	55.0	163.5	302	7.50	310.2	7.43	45.0	0.5	182	11	3.40	150	3.61	88.6	282	77.00	40.44	5.30
Q	55.2	163.6	302	7.49	310.3	7.42	40.5	3.5	176	12	3.40	150	3.61	88.2	294	76.09	36.65	5.52
R	55.3	163.8	302	7.48	310.5	7.40	37.5	3.5	171	47	3.40	150	3.61	87.8	312	74.93	33.76	5.34
S	55.5	163.9	302	7.47	310.6	7.39	31.0	0.5	111	5	3.40	150	3.60	87.4	235	77.70	29.56	3.85
T	55.7	164.2	302	7.45	310.9	7.36	25.0	0.5	94	11	3.40	150	3.60	87.0	235	77.28	24.05	3.17

[1]Azimuth of profile.
[2]Convergence velocity.
[3]Azimuth of convergence vector.
[4]Corrected convergence velocity rate.
[5]Dip angle and uncertainties of its determination respectively.
[6]Maximum seismic depth and uncertainties of its determination respectively.
[7]Spreading rate [*Renkin and Sclater*, 1988].
[8]Azimuth of spreading [*Renkin and Sclater*, 1988].
[9]Corrected spreading rate.
[10]Age of the Pacific plate at the trench [*Renkin and Sclater*, 1988].
[11]Length of seismic slab activity in the slab.
[12]Age of the subducted slab at the maximum seismic depth.

Table 4. Comparison Between the Age Obtained from *Renkin and Sclater* [1988] and that Predicted by the General Empirical Dependence $D_m = f(\varphi)$.

Prf.	A^a m.y.	A^p m.y.
N	75.88	30
O	76.91	20
P	77.00	20
Q	76.09	20
R	74.93	20
S	77.70	20
T	77.28	10

A^a is the age of the subducted slab at the maximum seismic depth derived from *Renkin and Sclater* [1988] (see Table 3).

A^p is the age predicted from the general empirical dependence $D_m = f(\varphi)$.

Figure Captions

Figure 1. Tectonic framework of the Kamchatka subduction zone. Solid triangles are volcanoes. The arrow represents the subduction velocity vector. The Meiji seamounts are shown by the 4000 m and 5000 m bathymetric contours. The dashed line is the location of the Kruzenstern fracture zone and the shaded wide lines mark the volcanic front. Star points the DSDP site number 192 [*Creager et al.*, 1973].

Figure 2. Distribution of the seismicity registered between 1962 and 1990 by the KRSN. Numbers identify the seismic stations shown on Table 1. Black dots are events located deeper than 300 km and gray dots are events shallower than 300 km.

Figure 3. (a) Gutenberg-Richter relation, $\log N \sim M_w$, for the catalog of the KRSN, where N is the number of earthquakes. The dashed line approximates the linear part of the relationship. The catalog is apparently complete for magnitudes $3.8 \leq M_w \leq 6.5$. (b) Cumulative number of events from 1962 to 1990 from the KRSN catalog. The quasi-linear dependence of the cumulative number of events versus time indicates that the properties of the regional seismic network did not change during the observation period. Black arrows point to the two relatively small irregularities observed in 1972 and 1983.

Figure 4. (a) Histogram showing the number of events in the KRSN catalog for different error intervals both in focal depth and epicenter. (b) Maximum deviation of hypocentral locations between the original hypocenters and the perturbed locations as a function of magnitude. The circles represent the larger deviation in longitude, squares are the larger deviation in latitude, and crosses in depth; lines using the same symbols represent the average larger deviations in hypocentral location.

Figure 5. Summary of the estimated errors in hypocentral locations perturbing the phase arrival times and Earth structure as described in the text. Ellipses and crosses represent the maximum deviation between the original hypocenter and the various perturbed locations for epicenter and focal depth respectively. The tests show that the events located inland and close to the coast have smaller maximum hypocentral deviation than offshore events.

Figure 6. Example of three of the twenty one focal mechanisms determined in this study using a formal inversion of long-period teleseismic P and SH waveforms [*Nábelek*, 1984]; the rest are presented in the electronic supplement[1]. The focal mechanisms are shown in a lower hemispheric projection. Observed (solid line) and synthetic (dashed line) waveforms of P wave (top) and SH wave (bottom) are shown. The source time function is shown in the central part of the figure. The event number (Table 2) and date of the event are shown at the top.

Figure 7. Distribution of the focal mechanism solutions where the black compressional quadrant are determined from wave form inversion; the dark gray compressional quadrant from the centroidal moment tensor solutions reported by the Harvard University (HCMTS) [*Dziewonski et al.*, 1981; *Dziewonski and Woodhouse*, 1983]; and the light gray compressional quadrant are from first motion focal mechanisms. The numbers identify the events on Table 2. Other symbols are the same as those on Figure 1.

Figure 8. Comparison between the depth estimates for the events modeled in this study (Table 2) using the body-wave inversion (D_i) and the depths of the same events reported by the KRSN (D_l). Error bars are the uncertainties of the depth values reported by the KRSN (when available). The dashed line is the best fit linear dependence of D_l against D_i; $D_l = 1.01(\pm 0.03)D_i + 4.05(\pm 4.1)$.

Figure 9. Location of the profiles used in the study of the subducted slab configuration. The letters identify the profiles shown on Figures 10 and 11. Other symbols as in Figure 1.

Figure 10. Projection of the seismicity recorded by the KRSN shown along profile ZZ' (Figure 9). Solid triangles are volcanoes.

Figure 11. Seismicity profiles from AA' to TT' across the KSZ (Figure 9). Focal mechanism solutions are shown on side-view, lower hemispheric projection. The numbers identify the events in Table 2. Black and white dots on the focal mechanisms are the location of P and T axes respectively. Triangles represent the volcanoes. The dashed lines show the approximate configuration of the upper surface of the subducted slab. Other symbols are the same as those on Figure 7.

Figure 12. Isodepth contours in kilometers approximating the upper surface of the subducted slab in the KSZ. For the main part of the KSZ, from ~50°N to ~55°N, the dip angle is constant (~55°). The northern segment of the slab, from ~55°N to ~56°N, is shifted to the northwest. Klyuchevskoy and Sheveluch volcanoes are marked as K and S respectively. The other symbols are the same as on Figure 1.

Figure 13. Superposition of the upper boundaries of the seismicity in the subducted slab for profiles MM' - TT'. The horizontal distance is measured from the line approximating the trench strike.

Figure 14. Maximum seismic depth, D_m, versus thermal parameter, φ, of the subducting slab. The solid line is the empirical dependence $D_m = f(\varphi)$ obtained from data for different subduction zones [*Gorbatov et al.*, 1996]. The thin lines indicate the 95% confidence limits [*Gorbatov et al.*, 1996]. Large circles are data for the KSZ (Table 3). Vertical and horizontal bars are error estimates of D_m and φ respectively (Table 3). The letters identify the profiles (see Figure 9 and Table 3). Arrow points to the new position of the data (from N to T) fitting the general empirical curve (Table 4).

Figure 15. (a) Side projection of profile NQ. (b) Frontal projection of profile NQ (seen from the east). Ticks on the lower axis indicate the width of the NN'- QQ' profiles. Gray triangles are volcanoes. Focal mechanism solution for event #7 (Table 2) is shown on a side-view lower hemispheric projection.

Figure 16. Focal mechanism solutions of earthquakes near the transition zone. Black and white circles on the lower hemisphere represent compressional and tensional arrivals respectively. The numbers identify the events on Table 2. Gray triangles are volcanoes. The solid curves are isodepth curves in kilometers. The Klyuchevskoy and Sheveluch volcanoes are marked as K and S respectively. Other symbols are the same as those on Figure 7.

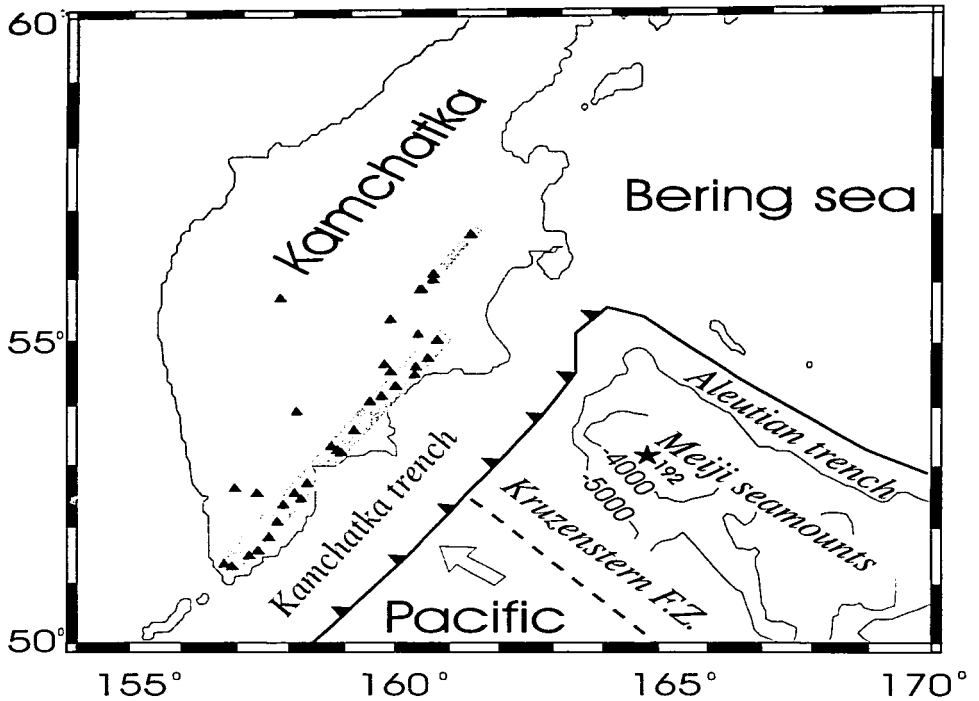

Figure 1.

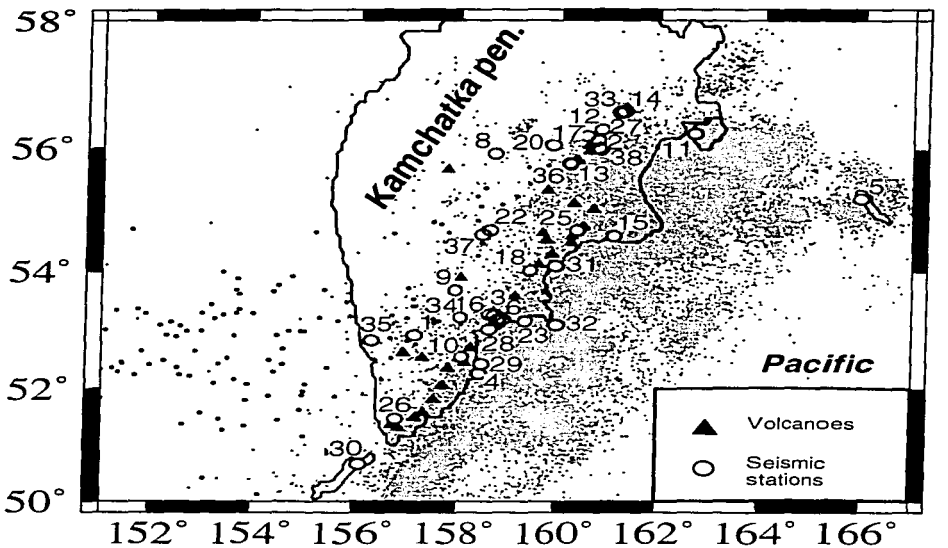
58°
56°
54°
52°
50°
152°
154°
156°
158°
160°
162°
164°
166°
Kamchatka pen.
Pacific
Volcanoes
Seismic stations

Figure 2.

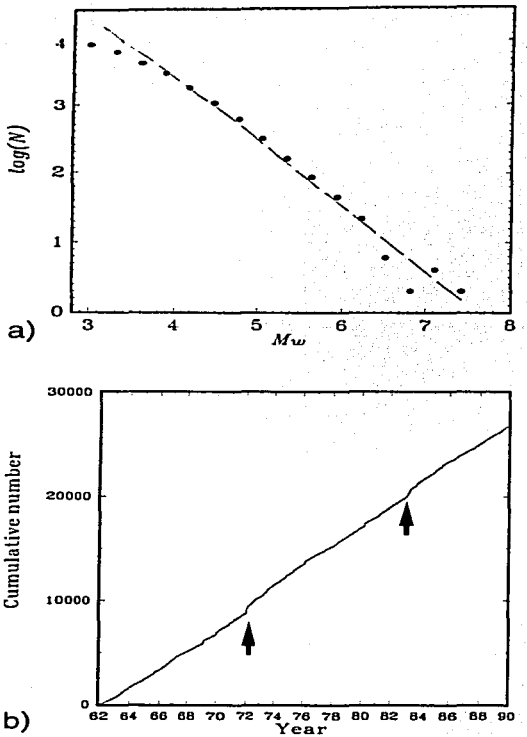

Figure 3.

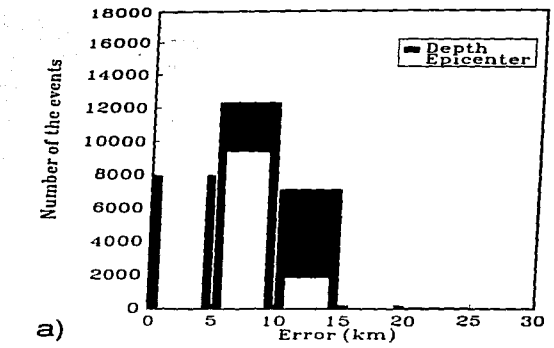
18000
16000
14000
12000
10000
8000
6000
4000
2000
0
Number of the events
Depth
Epicenter
0
5
10
15
20
25
30
Error (km)
a)

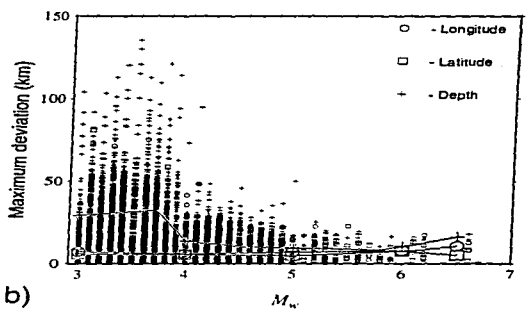
150
100
50
0
Maximum deviation (km)
- Longitude
- Latitude
- Depth
3
4
5
6
7
M_w
b)

Figure 4.

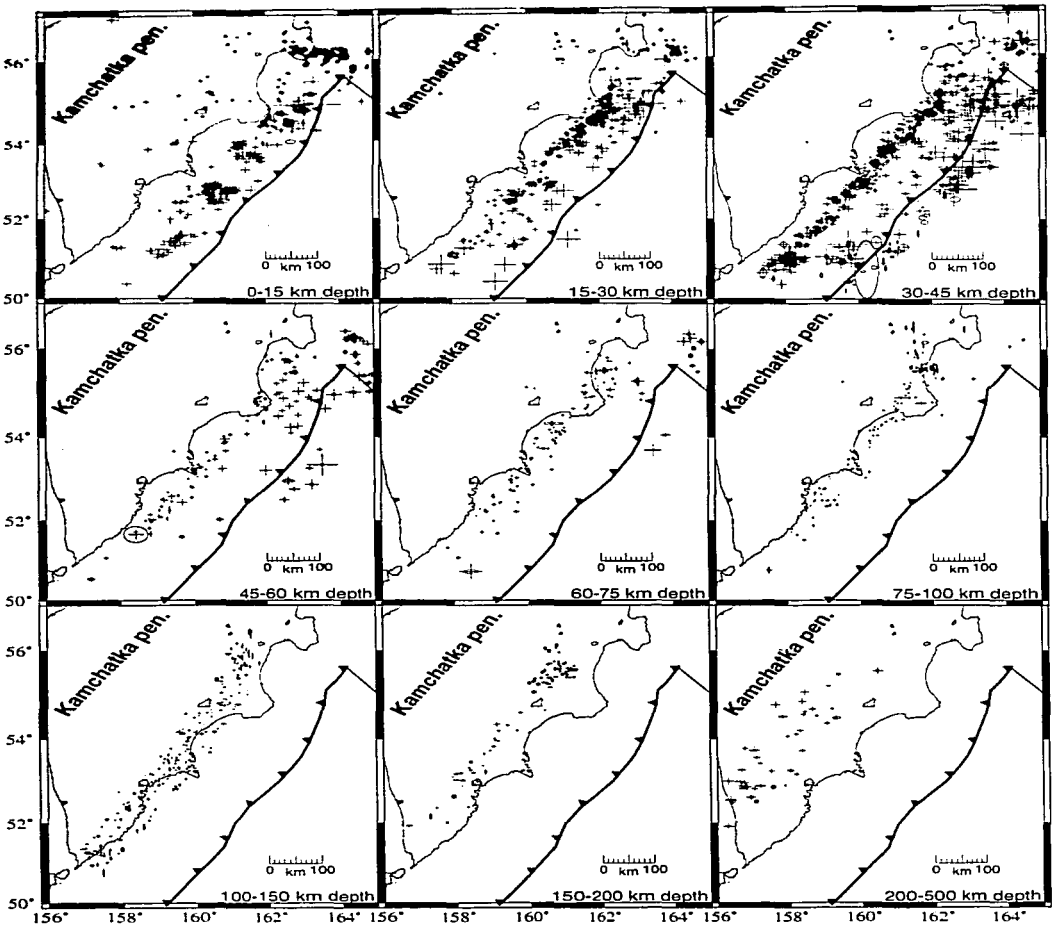
Kamchatka pen.
0 km 100
0-15 km depth
15-30 km depth
30-45 km depth
45-60 km depth
60-75 km depth
75-100 km depth
100-150 km depth
150-200 km depth
200-500 km depth
56°
54°
52°
50°
156°
158°
160°
162°
164°

Figure 5.

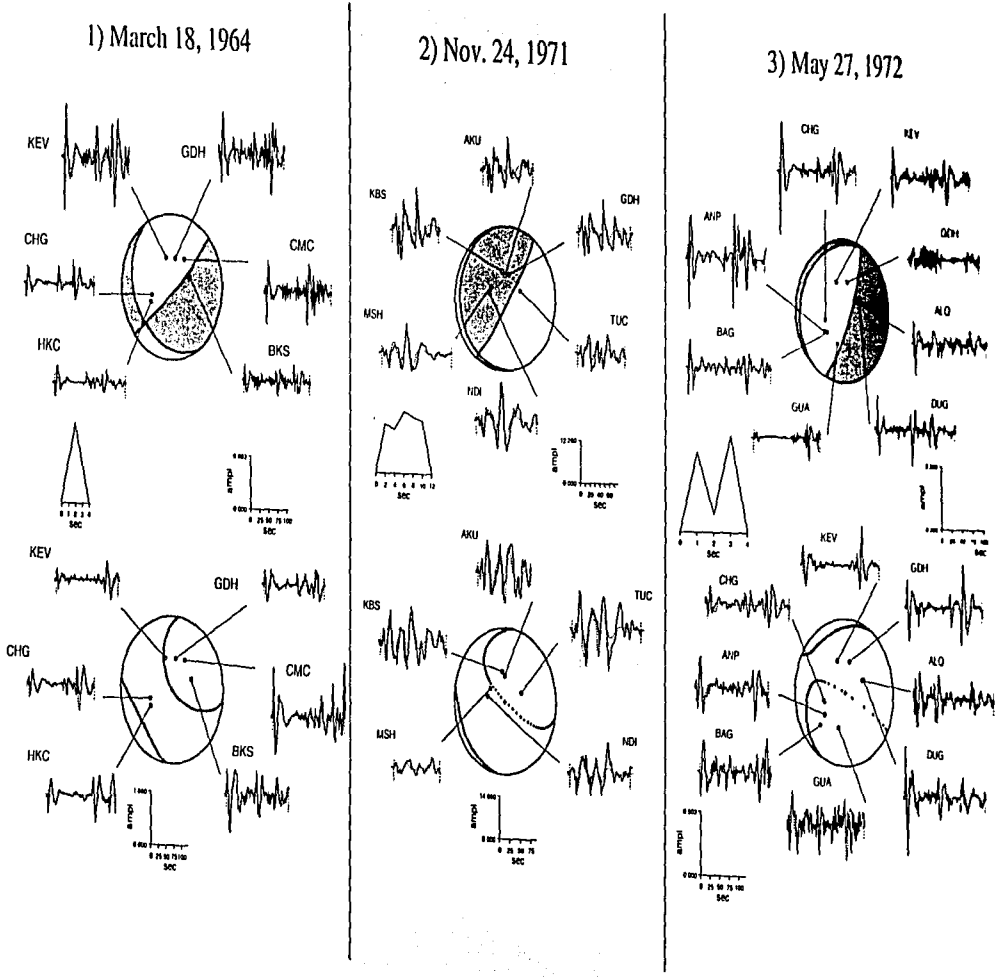
1) March 18, 1964
KEV
GDH
CHG
CMC
HKC
BKS
sec
ampl
KEV
GDH
CHG
CMC
HKC
BKS
2) Nov. 24, 1971
AKU
KBS
GDH
MSH
TUC
NDI
sec
ampl
AKU
KBS
TUC
MSH
NDI
3) May 27, 1972
CHG
KEV
ANP
QDH
BAG
ALQ
GUA
DUG
sec
ampl
KEV
GDH
CHG
ANP
ALQ
BAG
DUG
GUA
ampl

Figure 6.

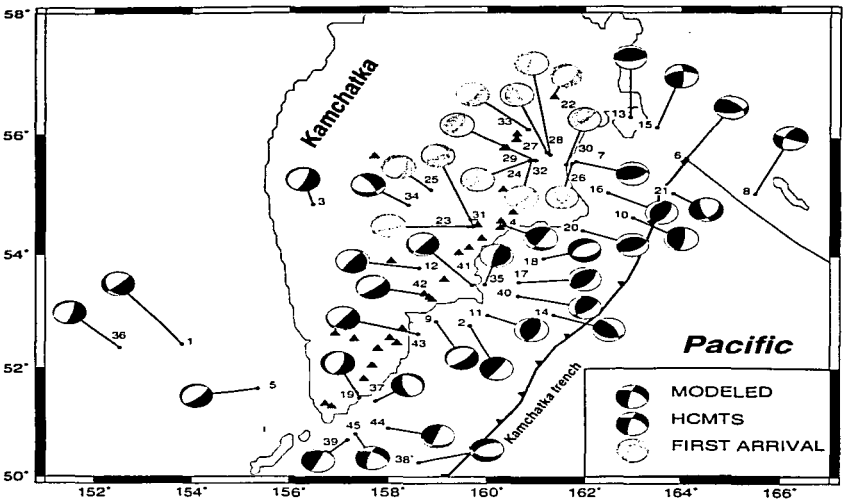
58°
56°
54°
52°
50°
152°
154°
156°
158°
160°
162°
164°
166°
Kamchatka
Pacific
Kamchatka trench
MODELED
HCMTS
FIRST ARRIVAL

Figure 7.

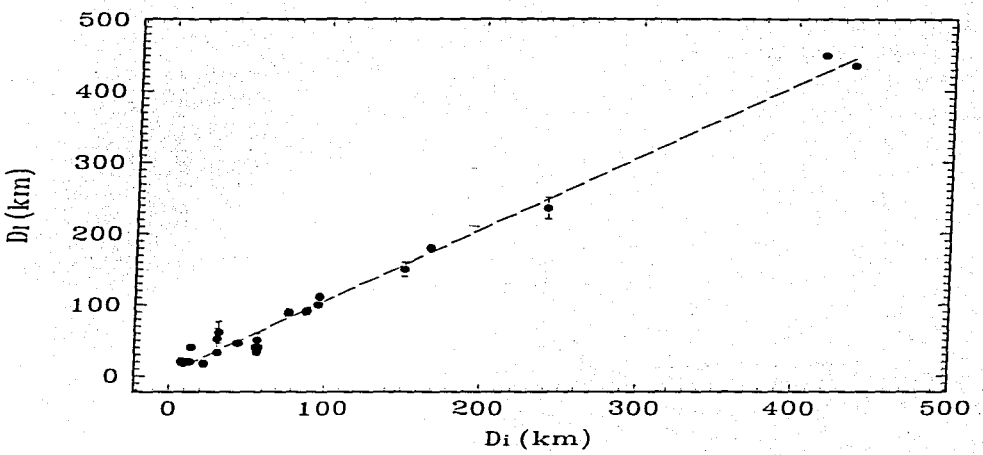

Figure 8.

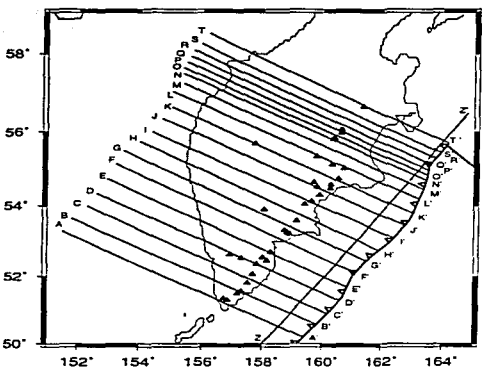

Figure 9.

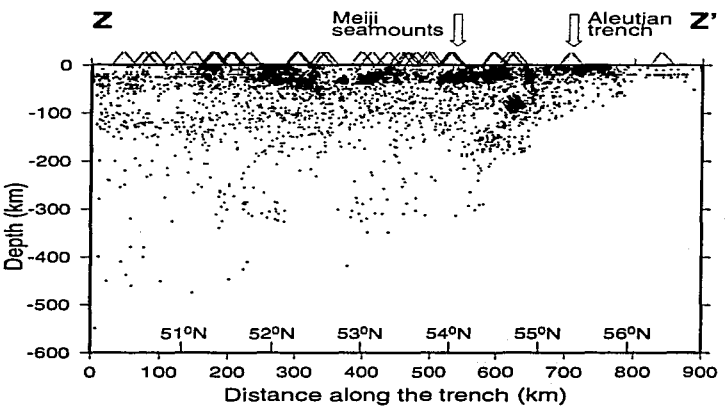
Z
Meiji seamounts
Aleutian trench
Z'
0
-100
-200
-300
-400
-500
-600
Depth (km)
51°N
52°N
53°N
54°N
55°N
56°N
0
100
200
300
400
500
600
700
800
900
Distance along the trench (km)

Figure 10.

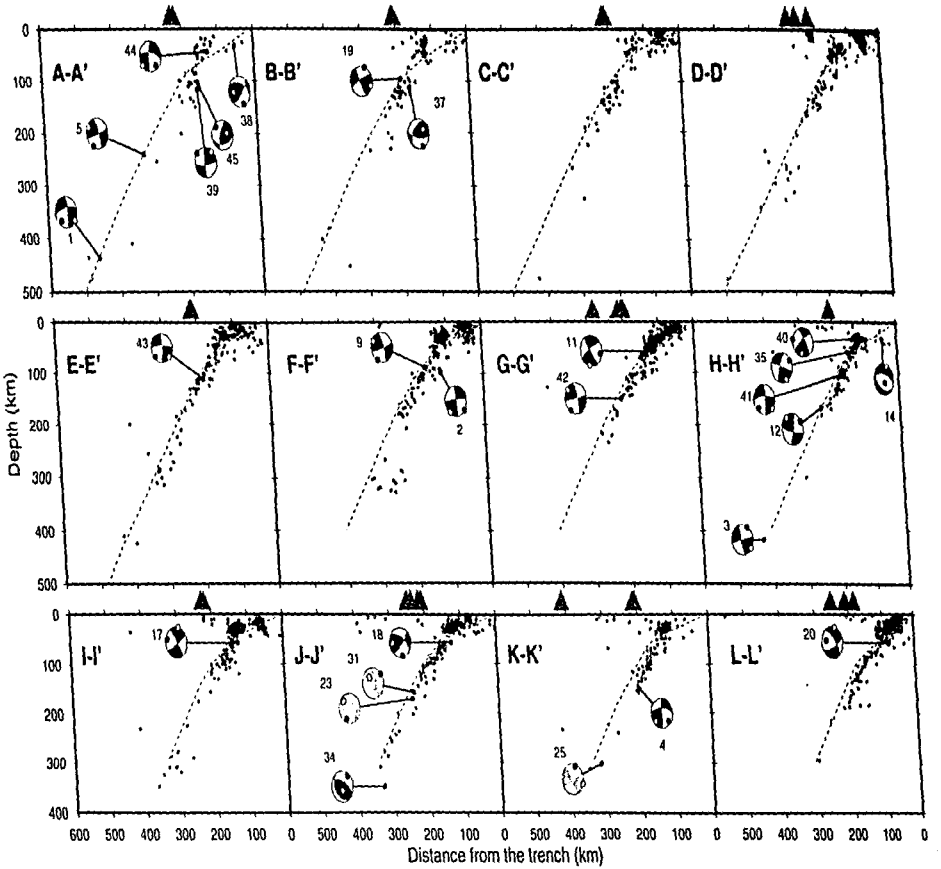
A-A'
B-B'
C-C'
D-D'
E-E'
F-F'
G-G'
H-H'
I-I'
J-J'
K-K'
L-L'
Depth (km)
Distance from the trench (km)

Figure 11.

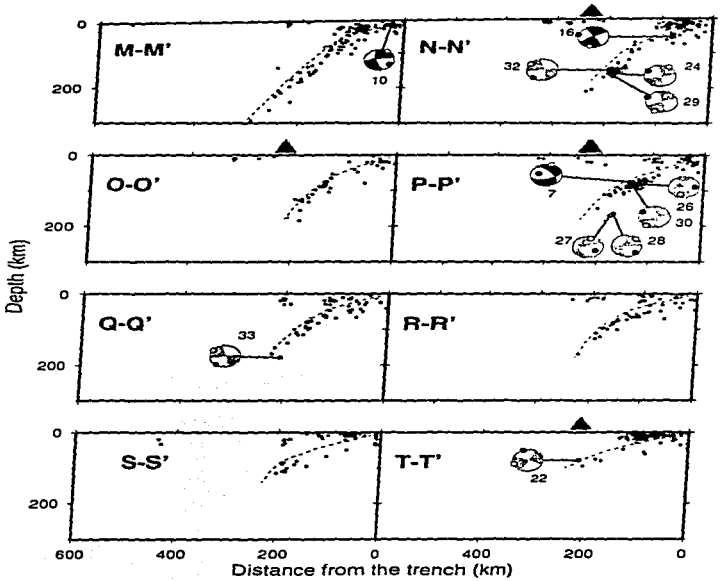

Figure 11 continued.

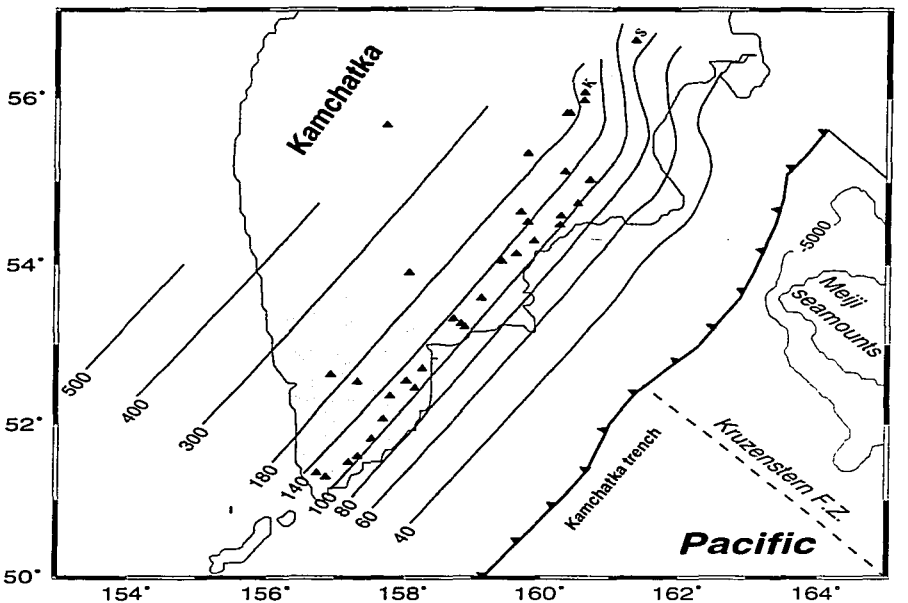
Kamchatka
56°
54°
52°
50°
154°
156°
158°
160°
162°
164°
500
400
300
180
140
100
80
60
40
3000
Meiji
seamounts
Kamchatka trench
Kruzenstern F.Z.
Pacific

Figure 12.

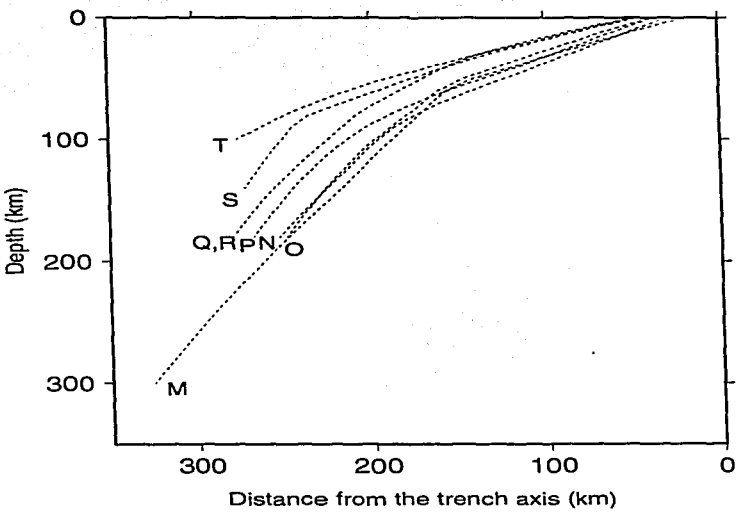
0
100
200
300
Depth (km)
T
S
Q,R
P
N
O
M
300
200
100
0
Distance from the trench axis (km)

Figure 13.

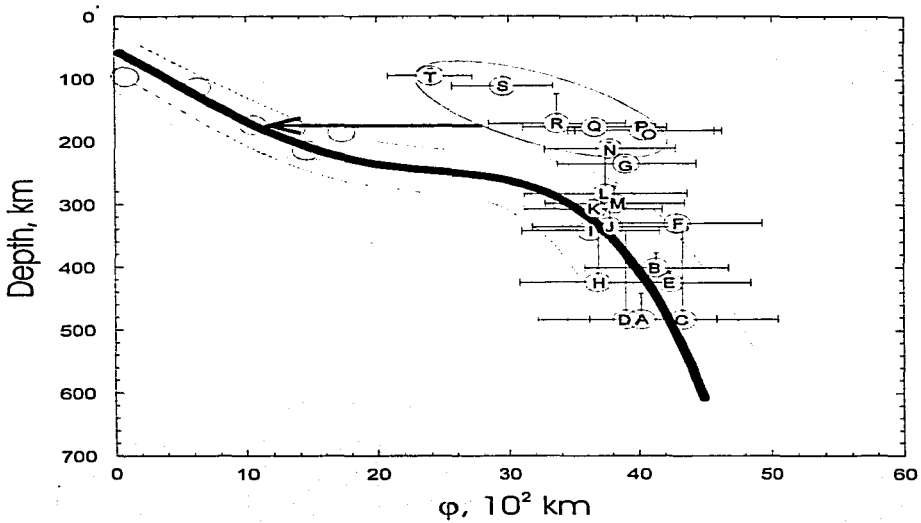
Depth, km
0
100
200
300
400
500
600
700
0
10
20
30
40
50
60
φ, 10² km
T
S
R
Q
P
O
N
G
L
M
K
J
I
F
B
E
H
D
A
C

Figure 14.

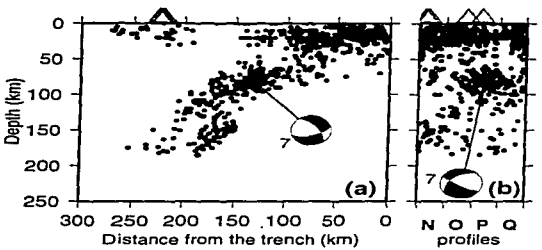
0
50
100
150
200
250
Depth (km)
300 250 200 150 100 50 0
Distance from the trench (km)
7
(a)
7
(b)
N O P Q
profiles

Figure 15.

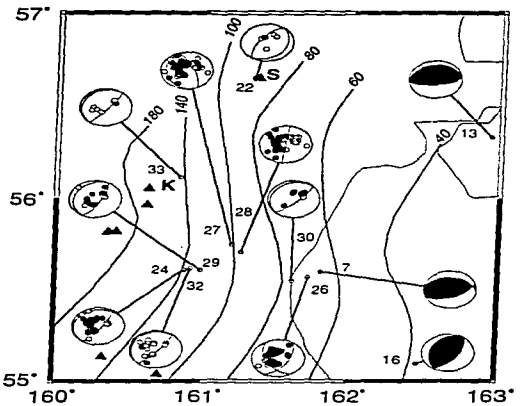
57°
56°
55°
160°
161°
162°
163°
100
80
60
40
22
S
180
140
33
K
28
27
30
29
24
32
26
7
13
16

Figure 16.

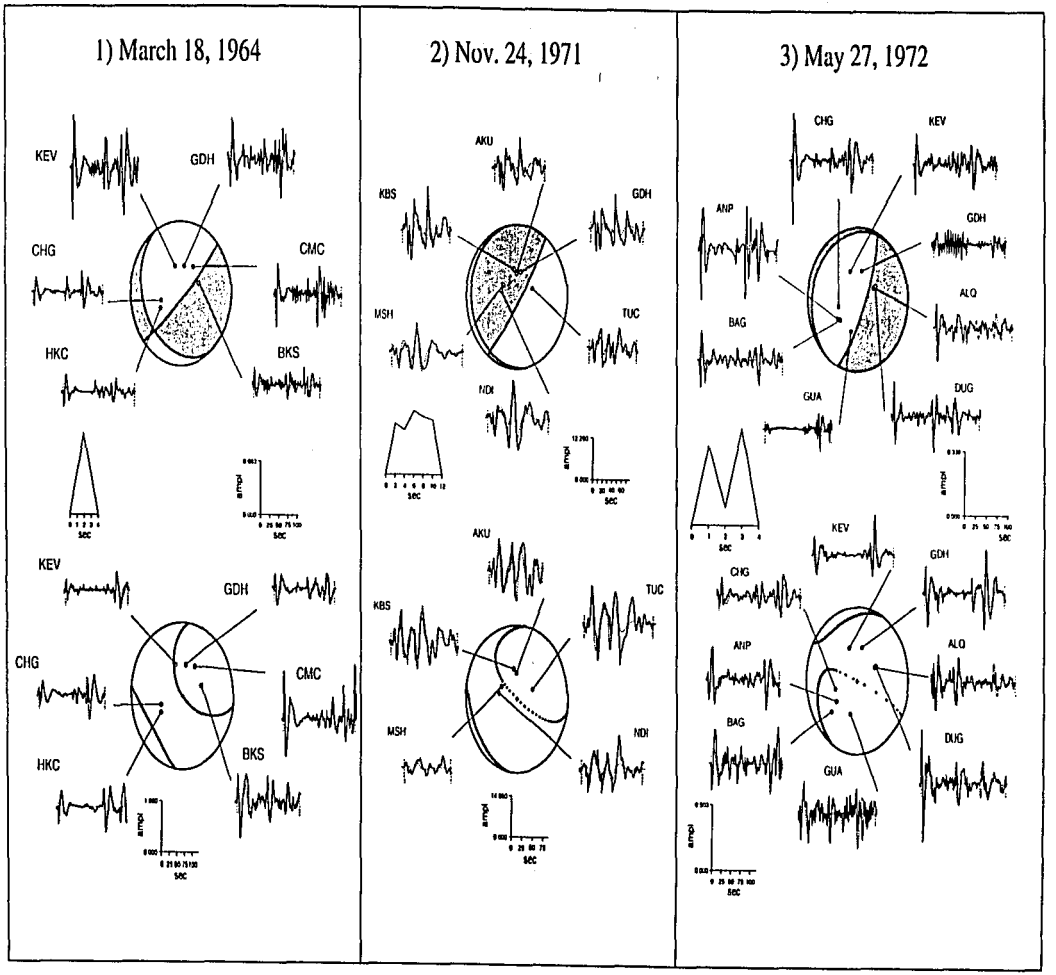

Electronic Supplement.

4) July 23, 1975

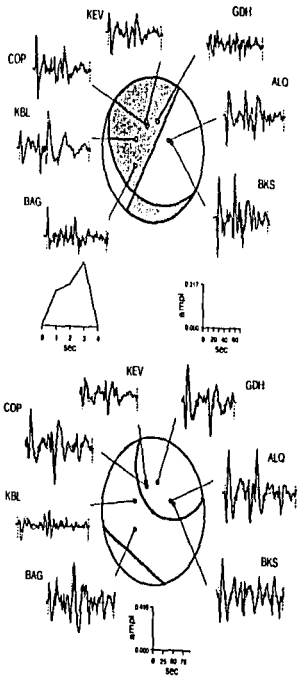

5) Sept. 21, 1977

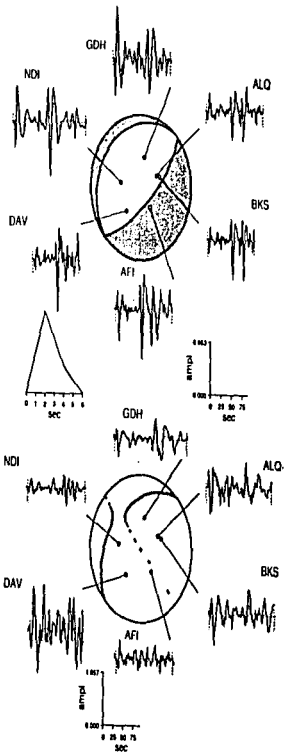

6) Nov. 9, 1979

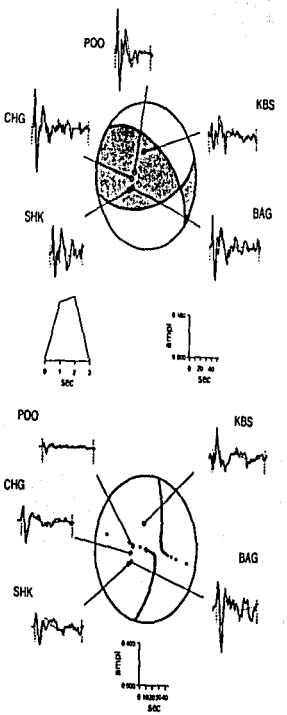

Electronic Supplement.

7) March 22, 1980

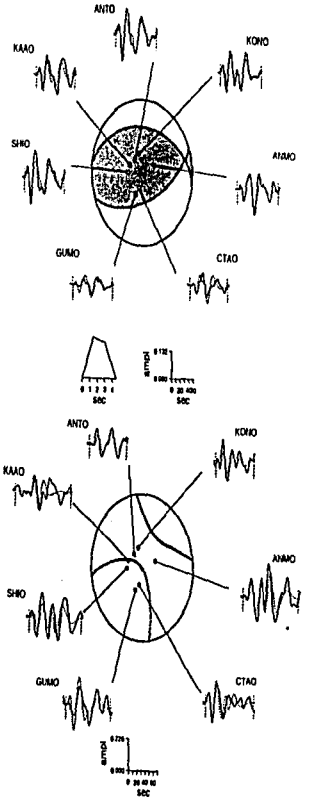

8) May 31, 1982

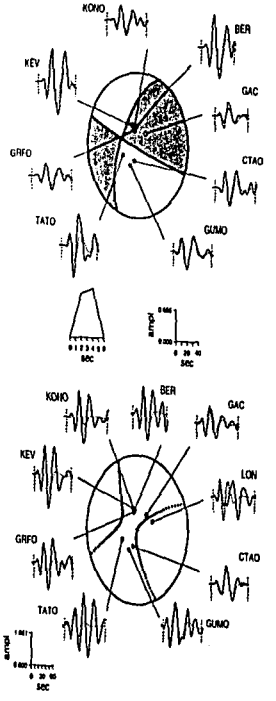

9) Nov. 14, 1982

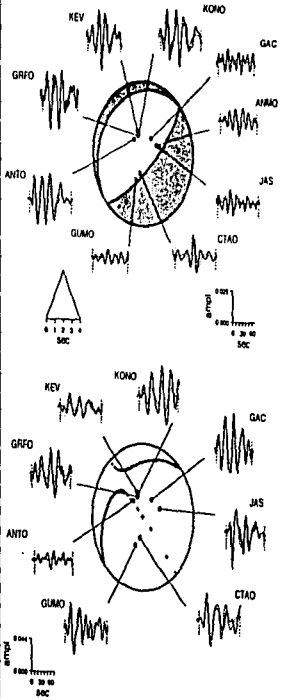

Electronic Supplement.

10) Jan. 5, 1983

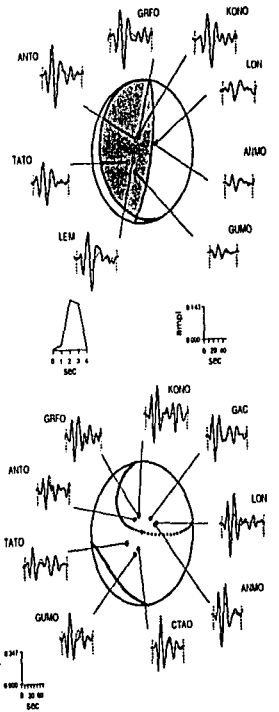

11) April 4, 1983

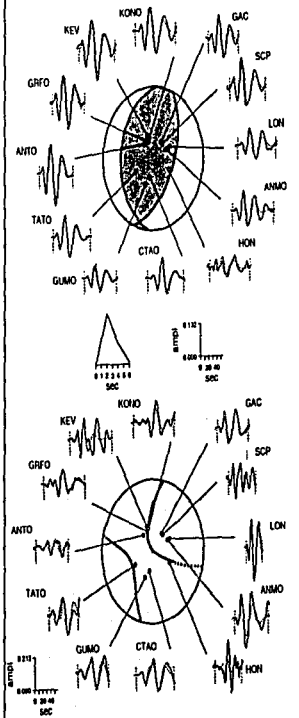

12) July 24, 1983

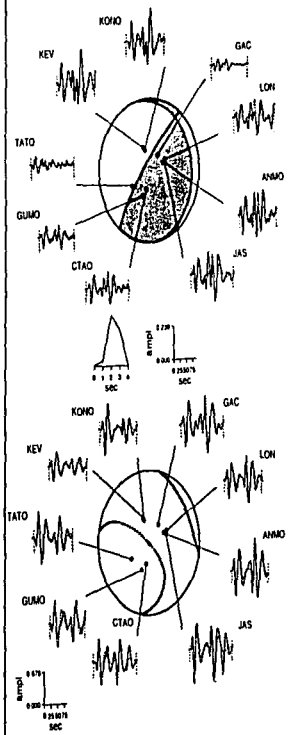

Electronic Supplement.

13) March 26, 1984

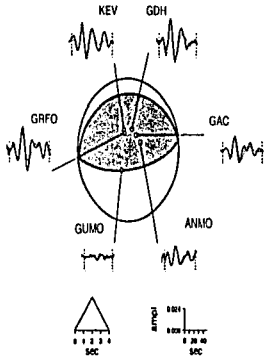

14) July 27, 1984

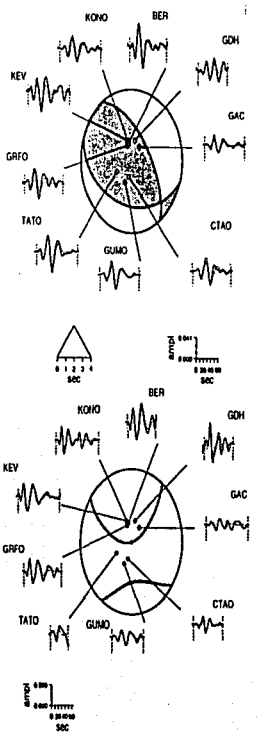

15) Dec. 28, 1984

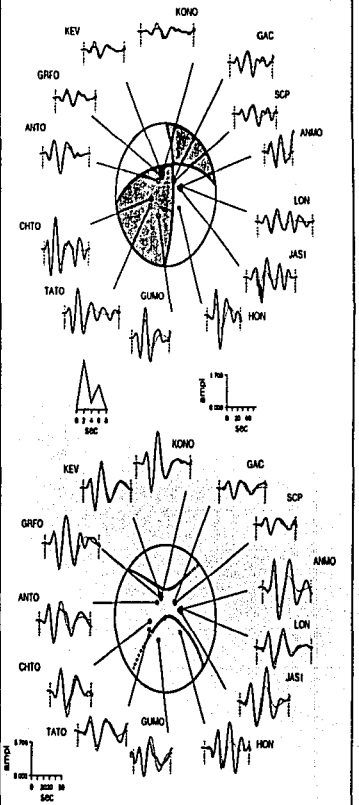

Electronic Supplement.

16) March 6, 1985

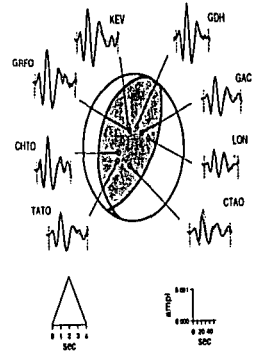

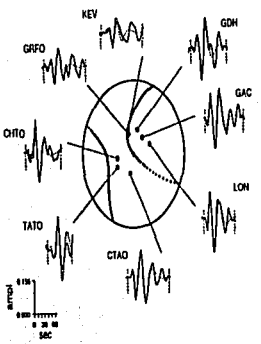

17) May 19, 1985

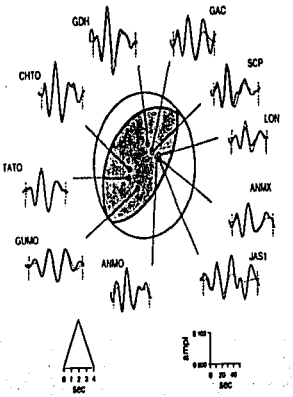

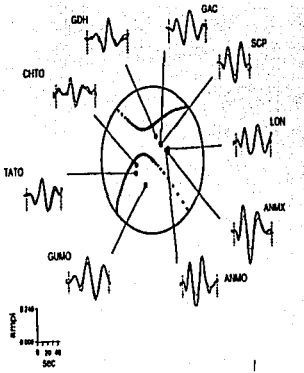

18) May 25, 1985

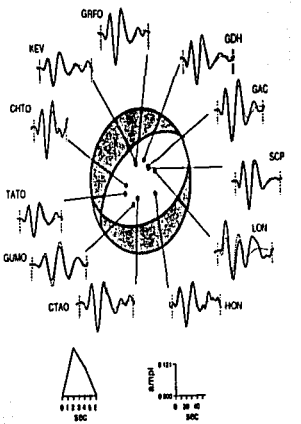

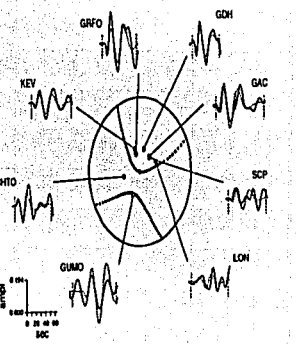

Electronic Supplement.

19) March 2, 1986

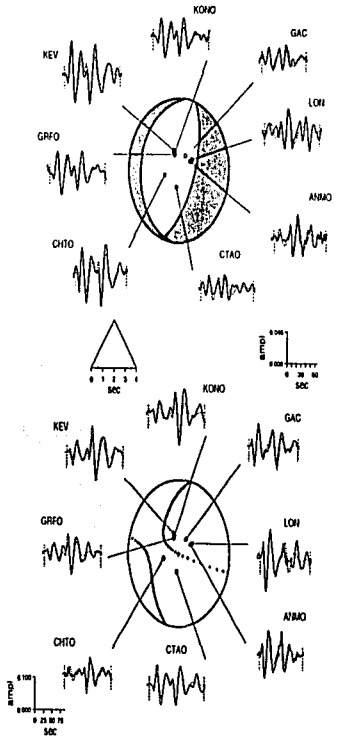

20) April 1, 1986

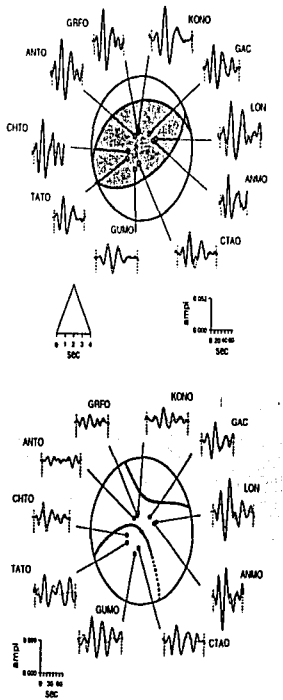

21) May 2, 1986

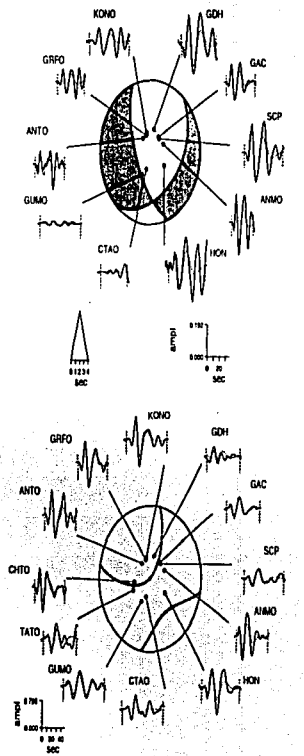

Electronic Supplement.

IV. Zona sísmica doble en Kamchatka determinada con datos regionales y telesísmicos

(Publicado en: *Gephys. Res. Lett., 21, 16,* 1675-1678, 1994)

A double-planed seismic zone in Kamchatka from local and teleseismic data

A. Gorbatov, G. Suárez and V. Kostoglodov

Instituto de Geofísica, Universidad Nacional Autónoma de México, México D.F., México.

E. Gordeev

Institute of Volcanology, Academy of Sciences of Russia, Petropavlovsk-Kamchatsky, Russia.

Abstract. The fine structure of a double-planed deep seismic zone is studied over a wide area of the Kamchatka peninsula. This prominent feature of deep seismic zone configuration is ascertained through the analysis of microearthquake hypocenters from the local seismic network of the Institute of Volcanology of Kamchatka and 22 focal mechanism solutions from the formal inversion of long-period P and SH waves for events with $m_b \geq 5.5$. Additionally, 11 focal mechanism solutions estimated from the first motion of P-waves and 12 centroid moment tensor solutions of Harvard University are used. The maximum depth of the double seismic zone is 170-180 km. The two planes of seismicity are separated by 40 km at a depth of 50 km, and by 10-15 km at 180 km depth. The focal mechanism solutions of shallow earthquakes show an abrupt change from the thrust events to down-dip compressional events at approximately 60 km depth at the upper boundary of the descending slab. Within the descending slab, the earthquakes with down-dip tensional axis form the lower plane of the double-planed deep seismic zone. Several earthquakes with down-dip tensional axis are discovered in a narrow area of the upper seismic zone at the depth of about 50 km. The double seismic zone is revealed clearly in the area between ~52°N to ~54°N and probably extends up to ~56°N.

Introduction

The first indication for the presence of a possible double seismic zone in Kamchatka was reported by *Fedotov* [1968]. Later, *Zobin* [1990] discussed the average stress distribution in Kamchatka based on focal mechanism solutions determined with P-wave first motion data from local earthquakes. Although

the results are not conclusive, his data suggest the presence of a double seismic zone. Recently *Kao and Chen* [1994] using the results of waveform inversion of teleseismic recorded events with $m_b \geq 5.5$ demonstrated that the double seismic zone can be traced in the central part of Kamchatka, and it turns into a regular Wadati-Benioff zone with down-dip compression in the northeastern part of Kamchatka trench. The purpose of this paper is to reexamine the seismicity beneath the Kamchatka peninsula in order to perform detailed analysis of the spatial distribution of earthquakes, both using the local catalog and focal mechanism solutions of accurately located hypocenters estimated from teleseismic data. Those data allow us to infer the fine morphology of a double seismic zone under the Kamchatka peninsula.

Hypocentral distribution

The seismic network of the Institute of Volcanology of Kamchatka (IVK) consists of twenty permanent, short-period (T_s=1.2s) seismic stations, and covers most of the Kamchatka peninsula (Figure 1). The catalog of local seismicity of Kamchatka includes epicenters, depths and magnitudes of the events and errors of their determination [*Fedotov et al.*, 1964; *Gusev*, 1979] from 1962 to 1990. For the analysis of hypocentral distribution, only the earthquakes with reported depth errors of less than 10 km were selected. The distribution of seismicity shows that the dip of the descending slab beneath the Kamchatka peninsula remains constant from ~51°N to ~55°N. Between ~55°N to ~56°N, it sharply changes and becomes shallower [*Gorbatov et al.*, 1993]. Cross-sections **A-A'** and **B-B'** (see insert in Figure 2) are selected according to the configuration of the descending slab to represent the general characteristics of the subduction process in Kamchatka.

The separation of the intermediate-depth seismicity into two planes is clearly seen on cross-section **A-A'** (Figure 3a). The hypocenter estimates for the region of this cross-section are more accurate because of the denser coverage of the seismic stations (Figure 1). The distance between two planes of seismicity is ~40 km at a depth of 50 km, and it decreases gradually to about 10-15 km at a depth of ~180 km. The dip of the upper plane is about 55°. The lower seismic sheet has a dip ~20° less than the upper sheet.

In cross-section **B-B'** (Figure 3b) the separation of the two planes of seismicity is not as clear as on **A-A'** (Figure 3a). This is probably because of a less dense distribution of seismic stations in northern Kamchatka resulting in less accurate hypocentral locations than in the central part of the peninsula (Figure 1).

Stress distribution from teleseismic data

The determination of focal mechanisms is based on a least square inversion of long-period P and SH waveforms [*Nábelek*, 1984]. In total, 22 teleseismicaly recorded events ($m_b \geq 5.5$) were modeled (Gorbatov et al., manuscript in preparation, 1994) (Figure 2), using the data from the National Earthquake Information Center (NEIC) World-Wide Standardized Seismograph Network (WWSSN) dataset. Additionally, twelve centroid moment tensor solutions reported by Harvard University (HCMTS) [*Dziewonski et al.*, 1981; *Dziewonski and Woodhouse*, 1983] were included together with eleven focal mechanism solutions (Gorbatov et al., manuscript in preparation, 1994) estimated from the P-wave first motion arrivals reported by the International Seismological Center (ISC) bulletin (Figure 2).

Some part of those focal mechanism solutions are presented in Table 1. It should be noticed that our set of the modelled events extends further to the north than the data set of *Kao and Chen* [1994] (which is limited by 54°N) and only four events are the same in the both sets. These mutual events have practically similar focal mechanisms but the hypocentral depth systematically differs by 10-20 km, probably because we used for the inversion the local velocity model of *Balesta et al.* [1985], while *Kao and Chen* [1994] applied an averaged modification of the whole Earth velocity model [*Kennett and Engdahl*, 1991].

The homogeneous structure of the Wadati-Benioff zone in Kamchatka between 51°N to 55°N assessed from the local seismicity data allows us to project most of the focal mechanisms on cross-section **A-A'** (Figure 3a and Table 1). These focal mechanisms show thrust faulting down to the depth of ~60 km, reflecting the seismogenic contact between the Pacific and North America plates. Below this depth, the focal mechanism solutions change to down-dip compression in the upper seismic plane (Figure 3a). A deeper sheet of seismicity, ranging in depth from ~50 km to about 180 km, shows focal mechanisms with down-dip tensional axis. At depths greater than 180 km, both seismic planes seem to merge into one, where the focal mechanisms show consistently down-dip compression (numbers 1, 3 and 37 in Table 1).

Two relatively shallow events in the upper part of the Wadati-Benioff zone (numbers 19 and 44 in Figure 3a and Table 1) show tensional mechanisms. Those tensional events are located at a depth of ~50 km, near the lower edge of the interplate contact.

Four focal mechanisms are presented on cross-section **B-B'** (Figure 3b). Although the distribution of the local seismicity does not reveal the double seismic zone as clearly as on cross-section **A-A'**, those

four focal mechanisms certainly suggest a double-planed distribution of stresses (Figure 3b and Table 1). Unfortunately, a dearth of teleseismicaly recorded earthquakes and the diffuse distribution of local seismic stations give us no opportunity to study this area in more detail.

Discussion

It is interesting to compare the structure of the double seismic zone of Kamchatka obtained in this study with the results for other double seismic zones. The shape of the double seismic zone of Kamchatka is similar to that of Tohoku (Japan) in both the maximum depth and spatial separation of the two seismic bands [*Hasegawa et al.*, 1978a, b]. Assuming that the thermoelastic stress regime of the subducting lithosphere, as defined by the subduction parameters, controls the existence and structure of double seismic zones [*Fujita and Kanamori*, 1981; *Goto et al.*, 1985; *Kawakatsu*, 1986], this similarity is surprising considering that the subduction parameters: age (**A**), convergence velocity (**V**), and dip angle (**a**), are different in Tohoku (**A** = 130 m.a., **V** = 9.5 cm/yr, α= 33°) and in Kamchatka (**A** = 77 m.a., **V** = 7.7 cm/yr, α = 55°) [*Cande et al.*, 1989; *DeMets et al.*, 1990; *Hasegawa et al.*, 1978 a, b]. Probably each one of these parameters itself does not affect significantly the shape of the double seismic zones but somehow their combination might be of the same order of influence on both seismic zones that produces this similarity of shapes.

Kao and Chen [1994] concluded that the double seismic zone in the central Kamchatka alters to a single seismic sheet of down-dip compression near 53°N. However our local seismicity data and focal mechanism solutions suggest that double seismic zone extends at 56°N. It is evident that the down-dip tensional events exist along the whole subduction zone of Kamchatka (Figure 2), in particular, the events numbered 4, 29 and 31 (Figure 2 and Table 1) lay to the north of 53°N and indicate the authenticity of the double seismic zone (Figure 3b).

A correlation between the changing in time coupling at the interplate thrust zone and the occurence of normal faulting earthquakes, immediately down-dip from the coupled interface was proposed by *Astiz et al.* [1988]. The location of tensional events numbered 19 and 44 in the upper plane of seismicity may be in favor of that model. However further study is required to understand the spatial and temporal variations in the stress regime of the Kamchatka subduction zone.

Conclusion

Our results show that a double-planed seismic zone with a dip angle of ~55° exists along most of the subduction of Kamchatka up to ~55°N, and probably 55°-56°N. The stress distribution within the Pacific plate descending beneath the Kamchatka peninsula is similar to that observed in the Tohoku (Japan) subduction zone farther south, where a sheet of tensional events lies beneath one showing down-dip compression, from ~50 km to ~200 km depth.

The maximum depth of seismogenic coupling is confirmed by the presence of thrust events down to a depth of ~60 km. Below this depth, the focal mechanisms show an abrupt change to down-dip compressional events in the upper sheet of seismicity. The lower seismic plane is represented by the down-dip tensional events at depths between ~50 km and ~180 km.

Two tensional events were discovered at the upper seismic plane, located just near the deeper edge of the interplate contact zone at a depth of ~50 km. The origin of these events do not have a clear explanation and requires further detailed studies.

Acknowledgments. The authors would like to thank J. Pacheco and A. Gusev for useful discussions and suggestions. Valuable critical comments and recommendations were made by Kazuya Fujita and two anonymous reviewers.

References

Astiz, L., T. Lay and H. Kanamori, Large intermediate-depth earthquakes and the subduction process, *Phys. Earth Planet. Int., 53*, 80-166, 1988.

Balesta, S. T., and L. I. Gontovaya, The seismic model of the Earth's crust in the Asiatic-Pacific transition zone (in Russian), *Volcanology and Seismology, 4*, 83-90, 1985.

Cande, S. C., J. L. LaBrecque, R. L. Larson, W. C. Pitman III, X. Golovchenco, and W. F. Haxby, Magnetic Lineation of the World's Ocean Basins (map), *Am. Assoc. Petrol. Geol.*, 1989.

DeMets, C., R. G. Gordon, D. F. Argus, and S. Stein, Current plate motions, *Geophys. J. Int., 101*, 425-478, 1990.

Dziewonski, A. M., T.-A. Chou, and J. H. Woodhouse, Determination of earthquake source parameters from waveform data for studies of global and regional seismicity, *J. Geophys. Res., 86*, 2825-2825, 1981.

Dziewonski, A. M., and J. H. Woodhouse, An experiment in the systematic study of global seismicity: Centroid-moment tensor solutions for 201 moderate and large earthquake of 1981, *J. Geophys. Res., 88*, 3247-3271, 1983.

Fedotov, S. A., I. P. Kuzin, and M. F. Bobkov, Detailed seismological studies in Kamchatka in 1961-1962 (in Russian), *Izv. Acad. Sci. USSR Geophys., 3*, 102-111, 1964.

Fedotov, S. A., On deep structure, properties of the upper mantle, and volcanism of the Kuril-Kamchatka island arc according to seismic data, *Am. Geophys. Un., Geophys. Monogr., 12*, 131-139, 1968.

Fujita, K. and H. Kanamori, Double seismic zones and stresses of intermediate depth earthquakes, *Geophys. J. R. Astr. Soc., 66*, 131-156, 1981.

Gorbatov, A., G. Suárez, V. Kostoglodov, and E. Gordeev, Kamchatka subduction zone: configuration of the slab from telemetric and local seismicity data (abstract), *Eos Trans. AGU, 74, 43*, 96, 1993.

Goto, K., H. Hamaguchi, and Z. Suzuki, Earthquake generating stresses in a descending slab, *Tectonophysics, 112*, 111-128, 1985.

Gusev, A. A., Computer determination of hypocenters of near earthquakes in Kamchatka (in Russian), *Volcanology and Seismology, 1*, 74-81, 1979.

Hasegawa, A., N. Umino, and A. Takagi, Double-planed structure of the deep seismic zone in the northeastern Japan arc, *Tectonophysics, 47*, 43-58, 1978a.

Hasegawa, A., N. Umino, and A. Takagi, Double-planed deep seismic zone and upper-mantle structure in the northeastern Japan arc, *Geophys. J. R. Astr. Soc., 54*, 281-296, 1978b.

Kao, H., and W.-P. Chen, The double seismic zone in Kuril-Kamchatka: The tale of two overlapping single zones, *J. Geophys. Res., 99, B4*, 6913-6930, 1994.

Kawakatsu, H., Double seismic zones: kinematics, *J. Geophys. Res., 91, B5*, 4811-4825, 1986.

Kennett, B. L. N., and E. R. Engdahl, Traveltimes for global earthquake location and phase identification, *Geophys. J. Int., 105*, 429-465, 1991.

Nábelek, J. L., Determination of earthquake source parameters from inversion of body waves, Ph. D. thesis, 361 pp., Mass. Inst. of Tech., Cambridge, 1984.

Zobin, V.M., Earthquake focal mechanism and seismotectonic deformation in the Kamchatka-Commander region, *J. Geodynamics, 12*, 1-19, 1990.

Table 1. Summary of Source Parameters

Event[1]	Date[2] YMD	Latitude[3] °N	Longitude[3] °E	Depth[4] km	Strike deg	Dip deg	Rake deg	M[5]
1^{m}	640318	52.43	153.79	437	47	84	-63	6.1
2^{m*}	711124	52.77	159.66	95	165	10	40	7.1
3^{m}	720527	54.87	156.48	418	23	78	-93	5.7
4^{m}	750823	54.53	160.35	151	122	30	1	5.8
5^{m}	770921	51.63	155.37	241	47	71	-89	6.1
7^{m}	800322	55.60	161.82	77	69	58	74	5.8
10^{m*}	821114	52.84	158.98	88	47	73	-91	5.3
11^{m}	830105	54.66	163.01	13	9	75	99	5.7
12^{m}	830404	52.95	160.02	57	23	56	101	5.7
13^{m*}	830724	53.77	158.62	168	217	81	103	6.0
18^{m}	850519	53.54	160.65	55	40	58	85	5.6
19^{m*}	850525	53.95	161.14	56	232	51	-105	5.6
21^{m}	860401	54.44	161.96	56	60	56	79	5.4
29^{f}	820417	55.71	161.27	165	7	90	90	5.3
31^{f}	831001	55.55	161.62	104	45	76	90	5.0
34^{f}	860423	56.12	160.83	179	37	79	-90	4.5
36^{h}	771106	53.50	159.96	60	36	18	109	5.1
37^{h}	791230	52.37	152.52	550	245	16	-41	5.4
38^{h}	811013	51.35	157.76	101	318	27	-117	5.3
39^{h}	820808	50.69	157.20	117	279	14	164	5.1
40^{h}	830415	53.30	160.64	30	184	38	47	5.8
41^{h}	840601	53.49	159.69	102	134	21	-176	5.2
42^{h}	870706	53.32	158.69	150	225	12	-93	5.2
43^{h}	880219	52.78	158.25	112	132	13	-175	5.2
44^{h}	880725	50.92	158.00	42	101	24	-9	5.6
45^{h}	880728	50.80	157.35	104	297	53	-160	5.1

[1]Identification number of events in Figure 2 and Figure 3. Indices mark the type of events: m - focal mechanism obtained from long-period wave form inversion: f - first arrivals: h - centroid moment tensor solutions of Harvard University (HCMTS) [*Dziewonski et al.*, 1981; *Dziewonski and Woodhouse*, 1983]; * - also analyzed by *Kao and Chen* [1994].

[2]Y: year; M: month; D: day.

[3]Estimates reported by the IVK.

[4]For modeled events the depths are from analysis of long-period wave form inversion and for the rest of events the depth are assigned as reported by the IVK.

[5]Magnitude M_w for the modeled events and m_b for the rest of events.

Figure Captions

Figure 1. Location of earthquakes (1962-1990) registered by the local seismic network of the Institute of Volcanology of Kamchatka (IVK).

Figure 2. Lower hemisphere earthquake mechanisms. From wave form inversion (black compressional quadrant); centroid moment tensor solutions reported by Harvard University (HCMTS) [*Dziewonski et al.*, 1981; *Dziewonski and Woodhouse*, 1983] (dark gray compressional quadrant); from first arrivals (light gray compressional quadrant). The numbers identify the events in Figure 3 and Table 1. Black triangles are active volcanos. Insert shows the location of cross-sections **A-A'** and **B-B'**.

Figure 3. (a) Cross-section **A-A'**. All events recorded by the local seismic network within a band of 20 km on each side of the cross-section are selected. (b) Cross-section **B-B'**. All events within a band of 5 km on each side of the cross-section are selected. Focal mechanism solutions are shown on a side-looking lower hemispheric projection (symbols as in Figure 2). The black and white dots on the focal mechanisms are the locations of the **P** and **T** axes respectively. Numbers identify the events in Figure 2 and Table 1. Gray triangles are active volcanos. Crosses are seismic stations.

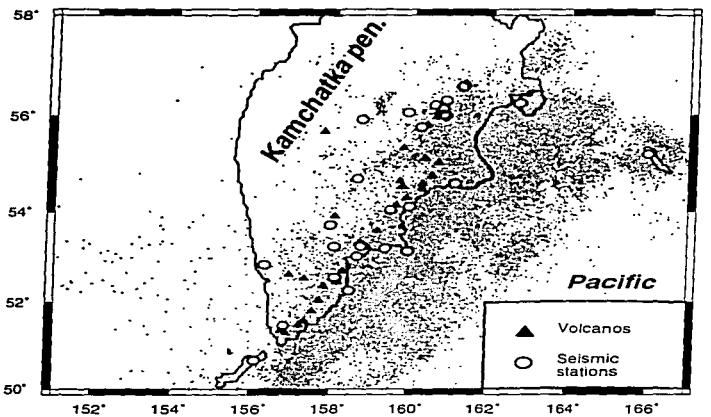
58°
56°
54°
52°
50°
152°
154°
156°
158°
160°
162°
164°
166°
Kamchatka pen.
Pacific
Volcanos
Seismic stations

Figure 1.

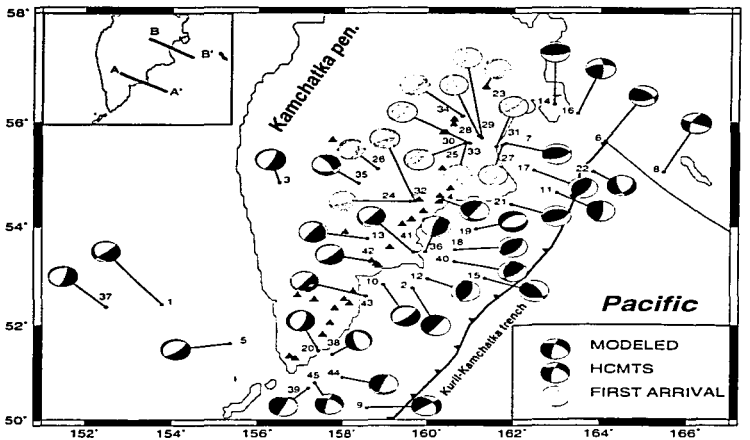
Kamchatka pen.
Pacific
Kuril-Kamchatka trench
MODELED
HCMTS
FIRST ARRIVAL
58°
56°
54°
52°
50°
152°
154°
156°
158°
160°
162°
164°
166°
A
A'
B
B'

Figure 2.

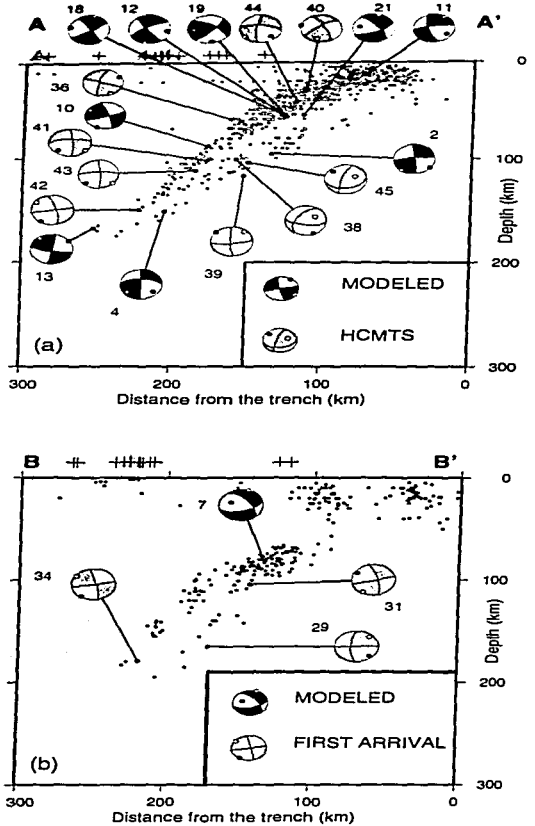
A
A'
18
12
19
44
40
21
11
36
10
41
43
42
13
4
39
38
45
2
MODELED
HCMTS
(a)
Depth (km)
0
100
200
300
Distance from the trench (km)
B
B'
7
34
31
29
MODELED
FIRST ARRIVAL
(b)
Depth (km)
0
100
200
300
Distance from the trench (km)

Figure 3.

V. Imágen tomográfica de onda P bajo la Peninsula de Kamchatka

(Enviado en: *J. Geophys. Res.*, 1997)

Tomographic imaging of the P-wave velocity structure beneath the Kamchatka peninsula.

A. Gorbatov, J. Domínguez, G. Suárez, and V. Kostoglodov

Instituto de Geofisica, Universidad Nacional Autónoma de México, México D.F., México.

E. Gordeev

Geophysical Service, Academy of Sciences of Russia, Petropavlovsk-Kamchatsky, Russia.

Abstract. A total of 5270 shallow and intermediate-depth earthquakes registered by the 32 stations of the regional seismic network of the Institute of Volcanology of Kamchatka were used to assess the P-wave velocity structure beneath the Kamchatka peninsula in the western Pacific. The tomographic inversion was carried out in three steps. First, a one-dimensional (1D) tomographic problem was solved in order to obtain an initial velocity model. Based on that 1D velocity model, 3D tomographic inversions with homogeneous and heterogeneous starting models were obtained. The Conrad (15 km depth) and the Moho (35 km depth) discontinuities determined from 1D tomographic inversion, and the upper boundary of the subducting slab are taken into account in the heterogeneous starting model for the travel times and ray path determinations. Both, the velocity structure and the hypocentral locations are determined simultaneously in the inversion. The spacing of the grid nodes is one half of a degree in the horizontal direction and 20 to 50 km in depth. A detailed P-wave tomographic image was determined down to a depth of 200 km. The resulting tomographic image presents a prominent low-velocity anomaly that shows a maximum decrease in P-wave velocity of ~6% at 30 km depth beneath the chain of active volcanoes. At depth, low-velocity anomalies are also observed in the mantle wedge extending down to a depth of ~150 km. These anomalies apparently are associated with the volcanic activity. The sedimentary basin of the Central Kamchatsky graben, to the west of the volcanic front, and the accretionary prism at the trench correlate with shallow, low-velocity anomalies. High-velocity anomalies observed at a depth of 10 km may be associated with the location of metamorphic basements in the Ganalsky-Valaginskoe uplift and upper crust of Shipunsky cape. The results also suggest that the subducted PAC has P-wave velocities ~2-7% higher than that of the surrounding mantle and a thickness of ~70 km.

Introduction

The Pacific plate subducts westward beneath the Kamchatka peninsula at a rate of ~8 cm/yr, with a dip angle of about 55° from ~50°N to ~54°N. A Wadati-Benioff seismic zone defines the downgoing slab to a maximum depth of ~500 km in the southern part of the Kamchatka subduction zone (KSZ) that shallows gradually to ~300 km toward the north. North of ~54°N, the subducted lithosphere is sharply deformed and the subducted slab becomes shallower. These drastic changes in dip angle are reminiscent of those occurring in younger subduction environments like Peru [*Cahill and Isacks*, 1992] and Mexico [*Pardo and Suárez*, 1995]. In Kamchatka, however, they take place in one of the oldest (~80 m.a.) [*Rea et al.*, 1993] subducted slabs in the world. This abrupt shallowing of the subducted slab produces a sudden offset of the volcanic front (volcanoes Kliuchevskoi and Sheveluch) to the northwest. That complexity of the subducted slab and the sharp offset of the volcanic front prompted several authors [*e.g., Tatsumi et al.*, 1994] to suggest that Kliuchevskoi and Sheveluch are not typical subduction-related volcanoes, but that instead they are originated by back-arc volcanic activity and are part of a second volcanic arc.

The seismic velocity structure of the Kamchatka subduction zone is very complex due to the presence of an active volcanic belt, a deep trench, and thick sedimentary basins (Figure 1). Also, the subducted lithosphere and the abundant volcanic activity cause large seismic velocity heterogeneities within the crust and upper mantle. Many of these tectonic features of the Kamchatka subduction zone should be visible as seismic velocity anomalies. Unfortunately, detailed regional studies of the seismic velocity structure, such as a three-dimensional tomographic inversion for the whole Kamchatka subduction zone including inland and offshore regions, has not been carried out to date.

Several studies have proposed two-dimensional, crustal velocity models beneath Kamchatka using arrival times observed from seismic explosions on land and in the ocean [*e.g. Anosov et al.*, 1978; *Selivestrov*, 1983; *Balesta et al.*, 1985]. These studies suggest that the oceanic lithosphere has higher P-wave velocities (~7%) than the continental crust located near the trench. At these shallow depths, the value of P-wave velocity decreases up to ~4% beneath the volcanic front in the central part of the Kamchatka peninsula.

Arrival times from regional earthquakes were also used to study the crustal structure of Kamchatka by *Gorshkov* [1958] and *Slavina and Fedotov* [1974]. Although studies using refraction methods exist for limited zones, such as several individual volcanoes [*Gorshkov*, 1958] or the crust covered by the regional seismic network [*Slavina and Fedotov*, 1974], their results consistently show relatively low seismic velocities beneath the volcanic front at the apparent crust-mantle boundary (~7.5 km/s), and relatively high velocities (~7.9 km/s) related to the subducted slab.

A three-dimensional tomographic inversion for the area between the coast and trench was performed by *Slavina and Pivovarova* [1992]. Although the results are restricted due to the limited area of their study, the data suggest that the P-wave velocity values are ~8.2 km/s in the oceanic plate and ~7.6 km/s in the lower continental crust.

The wide Kamchatka Regional Seismic Network (KRSN) has operated since 1962 reporting about six hundred earthquakes each year. The abundant seismic activity and the relatively dense seismic station coverage (Figure 2) provide the opportunity to determine in detail the tomographic images of the crust and upper mantle beneath the Kamchatka peninsula. The purpose of the present study is to infer the 3D velocity structure of the crust and upper mantle in the Kamchatka subduction zone (KSZ), applying a 3D tomographic inversion to the regional seismic data. That information may help to improve our understanding of the dynamic processes that control the subduction regime and the complex volcanic activity in the region.

Data and methods of analysis

Regional earthquake data

The arrival times recorded by the KRSN from January 1985 to December 1992 were used in this study (Figure 2). The network consists of thirty two, three-component seismic stations covering most of the Kamchatka peninsula. The majority of the stations are located in the central part of Kamchatka and along the coast (Figure 2). A total of 5270 events, occurring in the area limited by 50°N to 60°N and 150°E to 165°E, which were registered by more than four seismic stations with a formal error of hypocentral determination of less than 10 km [*Gorbatov et al.*, 1997], were selected for the analysis. The distribution of the number of earthquakes versus focal depth shows that most earthquakes occurred at depths shallower than ~200 km and a relatively small number of events are deeper than ~200 km (Figure 3).

To obtain a tomographic image of the Kamchatka subduction zone three inversions were carried out sequentially. First, a one-dimensional (1D) tomographic inversion [*Roecker*, 1981; 1982] was applied in order to obtain a starting 1D velocity model for the subsequent 3D inversions. Then, a 3D tomographic problem with a homogeneous starting model was resolved using the technique developed by *Zhao* [1991] and *Zhao et al.* [1992]. Finally, using the same method, a 3D inversion with a heterogeneous starting model was estimated.

The 1D inversion

Although there are several studies suggesting velocity models for the KSZ [*e.g. Gorshkov*, 1958; *Slavina and Fedotov*, 1974; *Anosov et al.*, 1978; *Selivestrov*, 1983; *Balesta et al.*, 1985; *Slavina and Pivovarova*, 1992], these velocity models show differences among themselves. In order to obtain the initial 1D velocity model the method proposed by *Roecker* [1981, 1982] was used. The initial homogeneous medium was divided into nineteen flat layers (each 5 km thick) down to a depth of 95 km. Layers with a thickness of 25 km were then used for the depth range between 95 to 300 km. For the final inversion, only 1657 events with errors in hypocentral determination of less than 5 km were used. The thickness of the layers down to a depth of 40 km was changed slightly (in 1 km steps) in order to refine the resulting model. After six iterations, the velocity variance in the inversion scheme reached 0.1 %. Neighboring layers with differences between velocity values smaller than 0.15 km/s were merged into thicker layers and the inversion performed again. The resulting 1D velocity model was accepted as the initial model for future iterations.

Table 1 shows the final 1D velocity model consisting of 8 layers where the average Poisson ratio is 1.71. The resolution coefficient is ~1 for the depth range between 15 and 200 km; however, the resolution coefficient is not good for the first two shallow layers for which it is 0.28 (0-5 km) and 0.56 (5-15 km) respectively. The layers deeper than 200 km do not have sufficient resolution (resolution coefficient is ~0.1) due to limited number of earthquakes located beneath that depth. Three layers are distinguished in the crust (Table 1). The upper (5 km) low-velocity layer is apparently associated with large sedimentary basins and volcanic ash deposits. Although the resolution is relatively poor for that layer (Table 1), the presence of the low-velocity upper layer in the 1D model gives more stable final results in comparison with the model without that layer. The velocity discontinuity at depth of ~15 and ~35 km correspond apparently to the Conrad and Moho discontinuities respectively.

The 3D inversion with homogeneous starting model

The inversion scheme of *Zhao et al.* [1991, 1992] differs from other 3D velocity inversion schemes that are normally used. The main reasons are: a) a 3D inhomogeneous velocity model with several velocity discontinuities of complex shape (such as the Conrad and Moho discontinuities, or the upper boundary of the subducted slab, for example) can be included in the inversion as initial, a priori, information; b) the velocities at any point in the model are calculated by the linear interpolation of the velocities at eight grid nodes surrounding that point; c) the ray tracing method of *Zhao* [1991], and *Zhao et al.* [1992] iteratively uses the

pseudobending technique of *Um and Thurber* [1987] and Snell's law to determine the ray path; **d)** converted and refracted phases (such as Pn, P*, PS, SP, SmP) can also be included in the inversion.

Firstly, the 3D tomographic inversion with homogeneous initial velocity model was carried out. The starting 1D velocity model was defined by the 1D model obtained previously, from which we assume the crustal thickness and structure, and the iasp91 earth model [*Kennett and Engdahl*, 1991]. Thus the 1D velocity model determined with method of *Roecker* [1981; 1982] was used down to a depth of 35 km and the iasp91 earth model [*Kennett and Engdahl*, 1991] is used for depths greater than 35 km.

In order to conduct the 3D tomographic inversion with the initial homogeneous starting model, the studied area is gridded in a half-degree-spaced steps in the horizontal direction and at depth steps of 10, 30, 60, 100, 150, 200 and 350 km. The velocity structure and hypocentral location are simultaneously determined. The root-mean-square (RMS), travel time residual which was 0.625 s before the inversion is reduced to 0.517 s after the inversion. Only grid nodes with more than 10 rays passing near each grid node (hit counts) were used in inversion. A cross-section of the 3D, P-wave velocity perturbations in percentages determined by the inversion are shown on Figure 4. The perturbation variance changes from approximately -7% to 7%. A low-velocity perturbation is observed mainly beneath the active volcanoes. An inclined high-velocity zone dipping to the west is clearly observed in the upper mantle. This high-velocity zone has a P-wave velocity which is 2 to 7% higher than "normal" mantle velocities. This high-velocity structure reflects the high-velocity subducted slab.

The 3D inversion with inhomogeneous starting model

The Conrad, Moho and upper boundary of subducted slab are sharp seismic velocity discontinuities [*e.g. Fisher et al.*, 1983] which should be taken into account in the ray tracing scheme in order to improve the final tomographic image. When these discontinuities are included in the model, the hypocenters are better located and ray coverage can be refined because ray trajectories are more accurately traced than under the assumption of a simple medium without the crustal reflectors and the subducted slab [*Zhao*, 1991; *Zhao et al.*, 1992; *Zhao and Hasegawa*, 1993; 1994].

To refine the results obtained with the homogeneous starting model, a tomographic inversion with an inhomogeneous starting model was carried out. The study area was divided into three layers separated by the Conrad (15 km depth) and the Moho (35 km depth) discontinuities; these three layers correspond to the upper crust (V_p=5.74 km/s), lower crust (V_p=6.74 km/s), and upper mantle respectively. The starting 1D velocity model is the same as that used in the homogeneous tomographic inversion. The results of the

homogeneous 3D inversion suggest that the subducting Pacific plate has P-wave velocities 2-7% higher than the normal mantle. Therefore, a high-velocity zone with an average velocity 4% higher than surrounding mantle was introduced in the model to represent the subducted Pacific plate. The configuration of the upper boundary of the subducted slab is taken from *Gorbatov et al.* [1996] (Figure 5). The P-wave velocity structure of the upper mantle beneath the subducted plate is the same as that beneath the continental crust.

The hypocentral location of the earthquakes and the P-wave velocity structure are solved simultaneously. Several inversions were carried out changing the initial thickness and the P-wave velocity of the subducted slab. Although some variations occur in the inversion residuals (Figures 6 a and b) and in the magnitude of the velocity anomalies, the resulting tomographic image does not change appreciably when the initial slab thickness is changed from 10 to 110 km, and the initial slab velocity perturbation is varied from 1 to 7% (Figure 6). These tests indicate that the stability of the tomographic inversion does not depend strongly on the assumed initial model. However, the reduction in RMS residuals shown on Figure 6 indicate broad minima in both the definition of the slab thickness and average fractional velocity perturbations. Also these tests show that the inversion performed with an initial slab thickness of 70 km and slab velocity 4% higher than that of the normal mantle gives the minimum residuals in a root mean square sense (RMS). The average RMS travel time residual is 0.602 s before the inversion and is reduced to 0.419 after three iterations.

Although the RMS residual of the inversion with a priori assumed information is reduced by 19% compared to that of the inversion with a homogeneous starting model, an *f*-test [*Draper and Smith*, 1966; *Zhao et al.*, 1995] is done in order to evaluate the statistical significance of the RMS residual reduction. The F ratio is defined as $F=((SSR_1-SSR_2)*DF_2)/((DF_1-DF_2)*SSR_2)$, where SSR is the summa of the squared residuals and DF is the number of degrees of freedom for the inversion with homogeneous (subscript 1) and inhomogeneous (subscript 2) starting models. Taking into account that the number of P-wave arrivals is 60,935 and that the number of nodes with hit counts greater than 10 is 697 for the inversion with homogeneous starting model, $DF_1=60935-(697+4*5270)=39158$. In the case of the inversion with an inhomogeneous starting model $DF_2=60952-(985+4*5270)=38887$. Other values are $SSR_1=12911.14$ and $SSR_2=12153.73$. The resulting F ratio is 8.94. Considering that DF_2 is a very large number, the value of infinity is used to select the F ratio from the tables. The corresponding F ratio for the decrease of 271 degrees of freedom (DF_1-DF_2) is $F(271, \infty, 0.99)<1.32$ [*Beyer*, 1991]. The results of the *f*-test show that the F ratio obtained in the test is larger than the value given by the F probability distribution at the 1% level. Therefore, the inversion with inhomogeneous starting model significantly improve the final results at a 99% confidence level.

Resolution test

A checkerboard resolution test (CRT) [*Humphreys and Clayton*, 1988; *Zhao et al.*, 1992] was applied to evaluate the resolution of the tomographic results. A simple, checkerboard synthetic structure with positive and negative perturbations of 3% and -3% was applied to the starting 1D model. The grid interval of the medium is the same as that in the tomographic inversion and a set of travel time delays resulting from ray tracing through the synthetic test structure were determined. Random errors corresponding to a normal distribution with a standard deviation of 0.1 s were added to the arrival times calculated for the synthetic model. Finally, the synthetic travel time delays were used in the tomographic inversion in order to recover the initial synthetic structure. A comparison of the synthetic inversion image and source synthetic structure allows us to recognize the areas where good resolution exists for the spatial distribution of available earthquakes and seismic stations in Kamchatka. The resolution is good where inversion results have the same velocity amplitude and checkerboard pattern as those of the original synthetic structure. Conversely, in areas where the initial pattern and amplitude are distorted the resolution is poor.

The checkerboard tests show that adequate resolution is obtained when the node separation in plan view is greater than 50 km. The resolution is good for most of the study area down to a depth of 60 km (Figure 7). In the case of the 100 km deep slice, the resolution is acceptable inland and only near the area where the subducted Pacific plate is located, decreasing to the north and south of the seismic network. For depths beneath the 150 km deep slice the resolution is poor and a correct test pattern is retrieved only in the central part of the study area. In conclusion, the resolution of the 3D inversion is good for most of the study area and it is best in the central part of the Kamchatka peninsula where the correct test pattern is recovered down to a depth of 200 km.

Discussion

The results of the 3D tomographic inversions (Figures 8 and 9) show a prominent continuous high-velocity zone in the upper mantle dipping landward which may be associated with the subducted Pacific plate. The introduction of a subducted Pacific plate as a priori information in the initial model gives a final RMS travel time residual smaller than that of the inversion with homogeneous starting model. Therefore, the tomographic image obtained with the 3D tomographic inversion using an inhomogeneous starting model was taken as the final result. The inversion suggests that the subducting Pacific plate has an average thickness of about 70 km

and a P-wave velocity which is 2 to 7% higher than that of normal mantle. The obtained average thickness of the subducted slab fits the results obtained from studies of Rayleigh wave dispersion data [*e.g., Leeds et al.*, 1974] of an oceanic lithosphere with an age of ~80 m.a., similar to that of the Pacific plate in the KSZ [*Rea et al.*, 1993]. The Wadati-Benioff seismic zone is located near the upper surface of the subducted slab (Figure 9). The lower plane of a double-planned seismic zone, which can be seen clearly in the profiles **a** and **b** (Figure 9), is traced approximately in the central part of the subducted slab. The Wadati-Benioff zone extends down to a maximum depth of ~500 km in southern Kamchatka, and ~300 km in the northern part of the peninsula [*Gorbatov et al*, 1997]. Unfortunately, the regional seismic data used in the study allows us to determine only the structures that are shallower than of ~200 km. Regional and teleseismic data that trace rays to depths greater than 200 km are necessary in the tomographic inversion in order to determine the deeper structures in the KSZ.

A sharply defined feature is the broad low-velocity anomaly located beneath the volcanoes and apparently associated with the present volcanic activity in the peninsula (Figure 8). The low-velocity zone is clearly defined beneath the volcanic front of Kamchatka, from the upper crust down to a depth of ~100 to ~150 km (Figure 9). The largest negative velocity perturbations (~-6%) occur at a depth of ~30 km and are observed along the whole volcanic front (Figure 8). These low-velocity perturbations form a continuous belt that is almost linear beneath the volcanic front between 51°N and 55°N. North of 55°N, the low-velocity anomaly is sharply shifted to the northwest following the location of Kliuchevskoi and Sheveluch volcanoes. These results show that Sheveluch and Kliuchevskoi volcanoes are part of the same subduction-induced volcanic process and not back-arc volcanoes as suggested by *Tatsumi et al.* [1994].

Figure 9 shows that the low-velocity anomalies extend down to a depth of ~50 km in the southern part of KSZ (profile **a**). To the north, the extension of the low-velocity anomalies increases reaching a depth of ~150 km. Although the volcanic front coincides approximately throughout the KSZ with a depth of the subducted slab of ~100 km (Figure 5), the low-velocity zones related to the active volcanoes extend to depths of ~150 km (Figure 9). Unfortunately, the lack of resolution in the northern part of the KSZ (profiles **e** and **f** on Figure 9) limits our observation to a depth of ~100 km.

The good resolution of the inversion for most of the study area down to a depth of 60 km (Figure 7) gives the opportunity to correlate the resulting velocity heterogeneities, located down at depths of about 10 km, to the upper crust geology of the KSZ. For example, a low-velocity band is spatially correlated with the Kamchatka trench (Figure 8). Apparently, this low-velocity band is associated with the accretionary prism. In particular, the low-velocity zone (~-4%) in the Kamchatsky bay correlates with the large sediment deposits located in that area [*e.g. Dickinson*, 1978; *Selivestrov*, 1983].

Other prominent and shallow low-velocity zones are observed in the Central Kamchatsky graben that probably corresponds to the large sedimentary basins that reach a thickness of up to ~5 km [*e.g. Moroz*, 1984; *Zinkevich*, 1993]. Several local high-velocity structures exist in the upper continental crust (10 km layer on Figure 8). Most of these zones are located close to the volcanoes and probably correspond to intrusive bodies. On the other hand, one of those zones can be seen clearly about 25 km east of Bakening volcano on profile **b** on Figure 9. Apparently, this high-velocity zone is associated with the Ganalsky-Valaginskoe uplift formed by metamorphic rocks and uplifted Cretaceous basement [*Rikhter*, 1993; *Konstantinovskaya et al.*, 1993; *Zinkevich*, 1993]. Shipunsky cape (Figure 1) is characterized also by the presence of high-velocity zones in the upper crust (Figures 8 and 9). That cape is composed by uplifted exotic Cretaceous basement [*Zinkevich*, 1993] which is apparently responsible for the high-velocity structures of that area.

The final three-dimensional velocity model shows the existence of large lateral heterogeneities (~±7%) in P-wave velocity in the Kamchatka subduction zone, due to the high level of volcanic activity and to the subduction of the Pacific plate (Figures 8 and 9). To evaluate the differences between using a simple 1D model and our final 3D velocity structure, the hypocenters relocated during inversion are compared with those determined with a 1D velocity model (Figure 10). The hypocenters of the events relocated using the inversion results show that a laterally varying velocity structure gives more accurate hypocentral location. For example, the double-planned seismic zone on cross-section of Figure 10a, that corresponds to cross-section **b** on Figure 1, is more distinct using the hypocenters relocated in the 3D inversion (Figure 10a) than that using the hypocenters determined with the initial flat 1D velocity model (Figure 10b). This difference is probably due to the fact that the flat 1D velocity model does not include an inclined high-velocity subducted slab. Seismic rays from earthquakes located in the lower sheet of the double-planned seismic zone go through this high-velocity zone which is not included in the flat 1D velocity model. Therefore, some of the hypocenters determined with a simple 1D model are located shallower than their real location.

Conclusions

The 3D, body wave tomography method was used to study the seismic velocity structure beneath the Kamchatka peninsula. A total of 5270 regional earthquakes and 32 seismic stations were used to infer the detailed P-wave tomographic images down to a depth of 200 km. The obtained results suggest that the subducting Pacific plate has an average thickness of about 70 km. The P-wave velocities in the subducted plate are ~2-7% higher than that of normal mantle. A prominent low-velocity zones exist in the crust and in the upper mantle beneath the active volcanoes down to a depth of ~150 km. The lowest values of these

velocity anomalies lie at a depth of ~30 km beneath the volcanic front. High-velocity zones were found in the upper crust that apparently correlate with the intrusive bodies, uplifts of metamorphic rocks and Cretaceous basements that are observed in the local geology. The low-velocity zones in the upper crust are associated with the thick sedimentary basins of the Central Kamchatsky graben and to the accretionary prism of the Kamchatka trench.

Acknowledgments. We thank D. Zhao for a copy of his inversion codes, useful discussions and suggestions. We benefited from discussion with Yu. Taran, A. Gusev, and N. Shapiro.

References

Anosov, G. I., S. K. Bikkenina, A. A. Popov, K. F. Sergeev, V. K. Utnasin, and V. I. Fedorchenko, *Deep seismic sounding of Kamchatka* (in Russian), 129 pp., Nauka, Moscow, 1978.

Balesta, S. T., and L. I. Gontovaya, The seismic model of the Earth's crust in the Asiatic-Pacific transition zone (in Russian), *Volcanology and Seismology*, *4*, 83-90, 1985.

Beyer, W. H., *Standard Mathematical Tables and Formulae*, CRC Press, Boca Raton, Fla., 1991.

Cahill, T., and B. L. Isacks, Seismicity and Shape of the subducted Nazca plate, *J. Geophys. Res.*, *97*, 17503-17529, 1992.

Dickinson, W. R., Plate tectonic evolution of north Pacific rim, in *Geodynamics of the western Pacific*, edited by S. Ueda, R. W. Murphy, and K. Kobayashi, pp. 1-19, Japan Scientific Societies Press, Tokyo, Japan, 1978.

Fisher, M. A., R. van Huene, G. L. Smith, and T. R. Bruns, Possible seismic reflection from the downgoing Pacific plate, 275 kilometers arcward from the eastern Aleutian trench, *J. Geophys. Res.*, *88*, 5835-5849, 1983.

Gorbatov, A., V. Kostoglodov, G. Suárez, and E. Gordeev, Seismicity and structure of the Kamchatka subduction zone, *J. Geophys. Res.*, 1997 (in press).

Gorshkov, G. S., Some questions of theory of volcanology, *Izv. Acad. Sci. USSR GeoL.*, in Russian, *11*, 23-35, 1958.

Humphreys, E., and R. W. Clayton, Adaptation of back projection tomography to seismic travel time problems, *J. Geophys. Res.*, *93*, 1073-1085, 1988.

Kennett, B. L. N., and E. R. Engdahl, Traveltimes for global earthquake location and phase identification, *Geophys. J. Int.*, *105*, 429-465, 1991.

Konstantinovskaya, Ye. A., V. P. Zinkevich, N. V. Tsukanov, and S. A. Garanina, Composition and structure of the upper Cretaceous to lower Paleogene lithostructural complexes in the eastern ranges of Kamchatka and their belonging to certain formations (in Russian), in *Accretional tectonics of eastern Kamchatka*, edited by Yu. M. Pusharovsky, pp. 59-114, Nauka, Moscow, 1993.

Leeds, A. R., L. Knopoff, and E. G. Kausel, Variations of upper mantle structure under the Pacific Ocean, *Science*, *186*, 141-143, 1974.

Moroz, Yu. F., On deep structure of east Kamchatka according to magnetotelluric sounding (in Russian), *Volcanology and Seismology*, *5*, 85-90, 1984.

Pardo, M., and G. Suárez, Shape of subducted Rivera and Cocos plates in southern Mexico: seismic and tectonic implications, *J. Geophys. Res., 100*, 12357-12373, 1995.

Rea, D., I. Basov, T. Janecek, E. Arnold, J. Barron, L. Beaufort, J. Bristow, P. de Menocal, G. Dubuisson, A. Gladenkov, T. Hamilton, L. Ingram, L. Keigwin, R. Keller, A. Kotilainen, L. Krissek, B. McKelvie, J. Morley, M. Okada, G. Olafson, R. Owen, D. Pak, T. Pedersen, J. Roberts, A. Rutledge, V. Shilov, H. Snoeckx, R. Stax, R. Tiedemann, and R. Weeks, Paleoceanographic record of north Pacific quantified, *EOS, Am. Geoph. Un. Transactions, 74, 36*, 406-411, 1993.

Rikhter, A. V., Metamorphic formations of eastern Kamchatka, in *Accretional tectonics of eastern Kamchatka*, edited by Yu. M. Pusharovsky, pp. 28-58, Nauka, Moscow, 1993.

Roecker, S. W., Seismicity and tectonics of Pamir-Hindu Kush region of central Asia; Ph. D. thesis, 256 pp., MIT, Cambridge, 1981.

Roecker, S. W., Velocity structure of Pamir-Hindu Kush region: possibly evidence of subducted crust, *J. Geophys. Res.*, 87, B2, 945-959, 1982.

Selivestrov, N. I., Structure of the junction zone of the Kurile-Kamchatka and Aleutian island arcs according to data from continuous seismic profiling (in Russian), *Volcanology and Seismology, 2*, 53-67, 1983.

Slavina, L. B., and S. A. Fedotov, The velocities of longitudinal waves in the upper mantle beneath Kamchatka (in Russian), in *Seismicity and earthquake prediction, the properties of the upper mantle and their relation to volcanism in Kamchatka*, edited by S. A. Fedotov, pp. 188-200, Nauka, Moscow, 1974.

Slavina L. B., and N. B. Pivovarova, Three-dimensional velocity models of focal zones and refinement of hypocentral parameters, *Phys. Earth and Planetary Int.*, 75, 77-88, 1992.

Um, J., and C. H. Thurber, A fast algorithm for two-point seismic ray tracing, *Bull. Seismol. Soc. Am., 77*, 972-986, 1987.

Zhao, D., A tomographic study of seismic velocity structure in the Japan Islands, Ph.D. thesis, 301 pp., Tohoku Univ., Sendai, Japan, 1991.

Zhao, D., A. Hasegawa, and S. Horiuchi, Tomographic imaging of P and S wave velocity structure beneath northeastern Japan, *J. Geophys. Res., 97*, 19,909-19,928, 1992.

Zhao, D., and A. Hasegawa, P-wave tomographic imaging of the crust and upper mantle beneath the Japan Islands, *J. Geophys. Res., 98*, 4333-4353, 1993.

Zhao, D., A. Hasegawa, and H. Kanamori, Deep structure of Japan subduction zone as derived from local, regional, and teleseismic events, *J. Geophys. Res., 99*, 22,313-22,329, 1994.

Zinkevich, V. P., Structural zonation of eastern Kamchatka and characteristic features of its deep-seated structure (in Russian), in *Accretional tectonics of eastern Kamchatka*, edited by Yu. M. Pusharovsky, pp. 16-27, Nauka, Moscow, 1993.

Table 1. 1D P-wave velocity model.

Depth km.	V_P km/s	Error km/s	Resolution
0	3.65	0.13	0.28
5	5.74	0.24	0.59
15	6.74	0.05	0.99
35	7.37	0.02	1.00
60	7.64	0.03	1.00
75	7.84	0.03	1.00
100	8.00	0.06	0.99
160	8.22	0.25	0.90
200	8.30	0.79	0.08

Figure Captions

Figure 1. Tectonic framework of the Kamchatka subduction zone. Triangles are volcanoes and the arrows represent the relative plate motion in mm/yr. The Meiji seamounts are delineated by the -4000 and -5000 m bathymetric contours. Lower case bold letters denote the location of the 40 km wide cross-sections used in this study. Characters *B*, *K* and *S* are the Bakening, Kliuchevskoi, and Sheveluch volcanoes respectively.

Figure 2. Distribution of earthquakes located by the KRSN from 1985 to 1992 (black dots). Squares are seismic stations.

Figure 3. Number of earthquakes as a function of focal depth. Notice that most of the events are located at depths shallower than 50 km.

Figure 4. Cross-section **b** (Figure 1) of the fractional P-wave velocity perturbations resulting from the homogeneous 3D velocity inversion. The scale relating the size of the symbols to the velocity perturbations is shown in the insert. Solid triangles are volcanoes.

Figure 5. Isodepth contours in kilometers approximating the upper surface of the Pacific subducted slab (from *Gorbatov et al.* [1997]). Other symbols are the same as on Figure 1.

Figure 6. (a) Travel time residuals of the inhomogeneous 3D inversion in a root mean squares sense (RMS) versus initial slab thickness taken as a priori information in the inversion. P-wave velocity of the slab is assumed to be 4% higher than that of normal mantle. (b) RMS travel time residuals versus initial fractional P-wave velocity perturbation for a 70 km thick subducted slab.

Figure 7. Result of the checkerboard resolution test. The depth of each layer is shown in the lower right corner of each map frame. Solid triangles are volcanoes. Solid and open circles denote fast and slow velocities respectively. The scale relating the size of the symbols to the velocity perturbations is shown at the bottom.

Figure 8. Tomographic image of Kamchatka shown as fractional P-wave velocity perturbations for various depth slices. Red and blue shading shows slow and fast velocities respectively, according to the scale shown at the right. The depth of the each layer is shown in the lower right corner of each map frame. White triangles are volcanoes.

Figure 9. Tomographic image of Kamchatka shown as fractional P-wave velocity perturbations projected on 40 km wide cross-sections (Figure 1). Red and blue shading reflect the slow and fast velocities respectively, according to the scale shown at the bottom. Red triangles are volcanoes and white dots are the earthquakes used in the inversion. A light-colored mask covers the area where resolution is considered to be poor. Vertical black bars mark the location of the coastline and arrows point the location of the trench.

Figure 10. Hypocentral projection of the events on cross-section **b** (40 km wide) (see Figure 1 for location). **(a)** Events relocated with the resulting 3D velocity structure from the inhomogeneous tomographic inversion. **(b)** The same earthquakes located with a 1D velocity model. Notice that the scatter is reduced and the double-planned seismic zone is more clearly defined when the more realistic 3D inversion results are used.

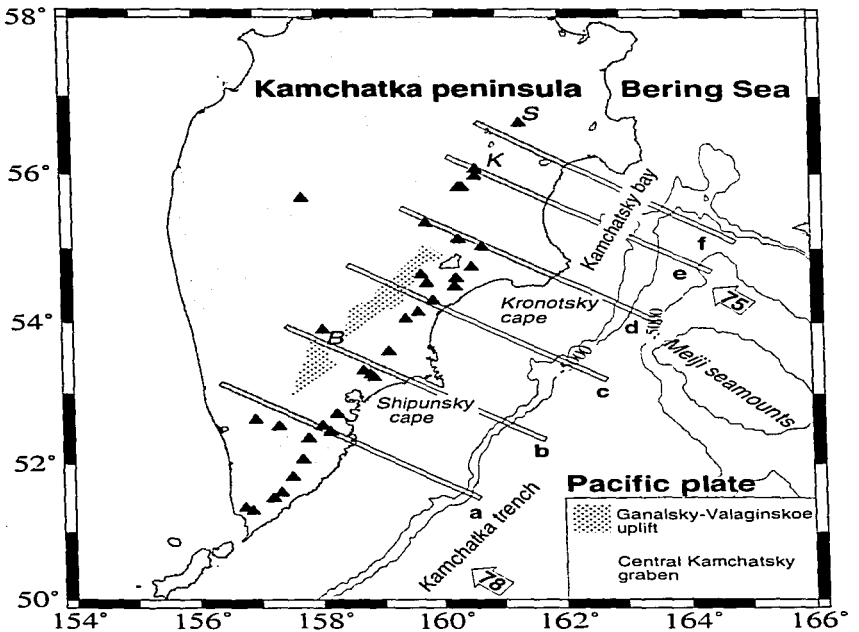
Kamchatka peninsula
Bering Sea
S
K
B
Kamchatsky bay
Kronotsky cape
Shipunsky cape
Meiji seamounts
a
b
c
d
e
f
15
78
Pacific plate
Ganalsky-Valaginskoe uplift
Central Kamchatsky graben
Kamchatka trench
58°
56°
54°
52°
50°
154°
156°
158°
160°
162°
164°
166°

Figure 1.

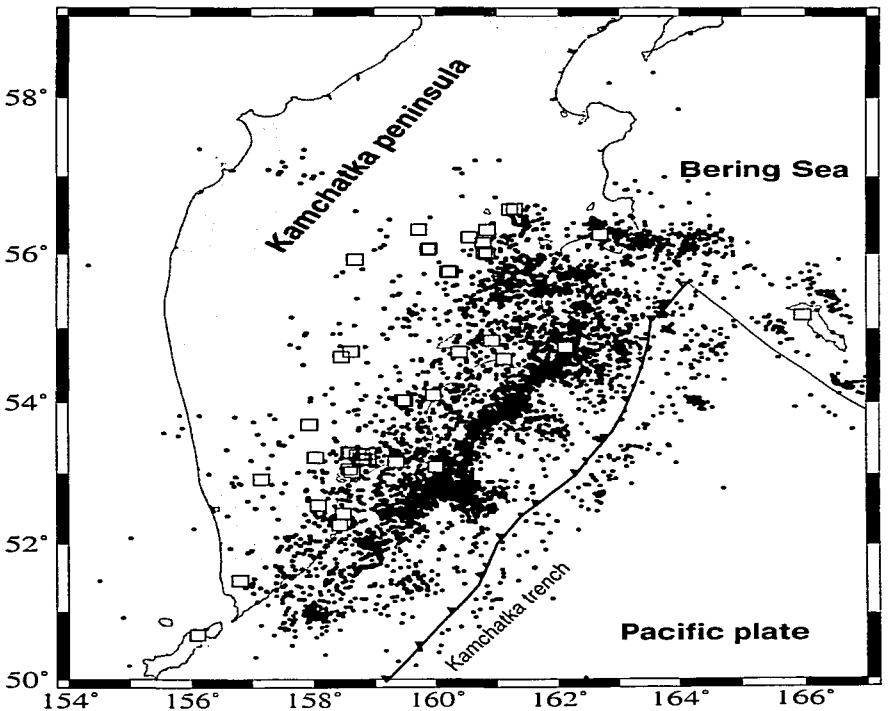
58°
56°
54°
52°
50°
154°
156°
158°
160°
162°
164°
166°
Kamchatka peninsula
Bering Sea
Kamchatka trench
Pacific plate

Figure 2.

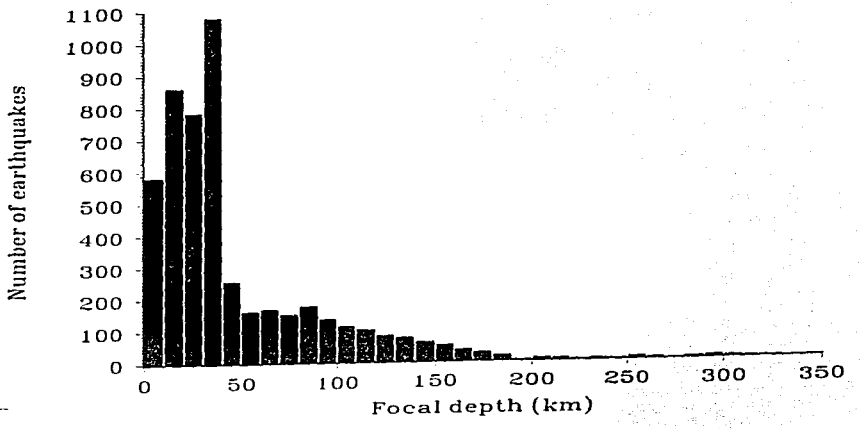
Number of earthquakes
1100
1000
900
800
700
600
500
400
300
200
100
0
0
50
100
150
200
250
300
350
Focal depth (km)

Figure 3.

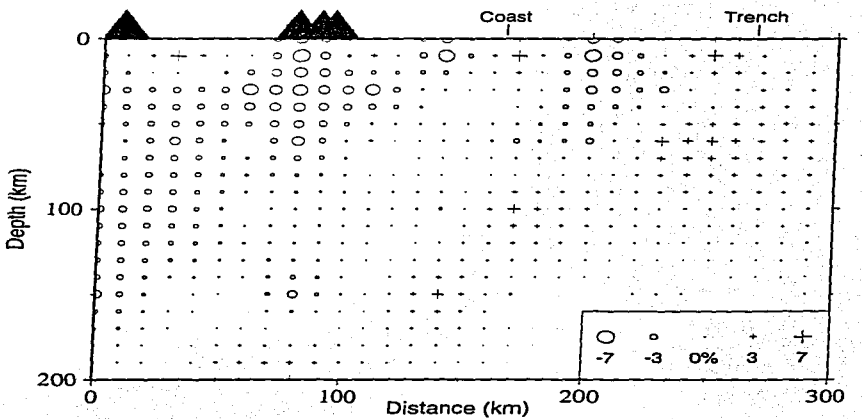
Coast
Trench
0
100
200
Depth (km)
0
100
200
300
Distance (km)
-7
-3
0%
3
7

Figure 4.

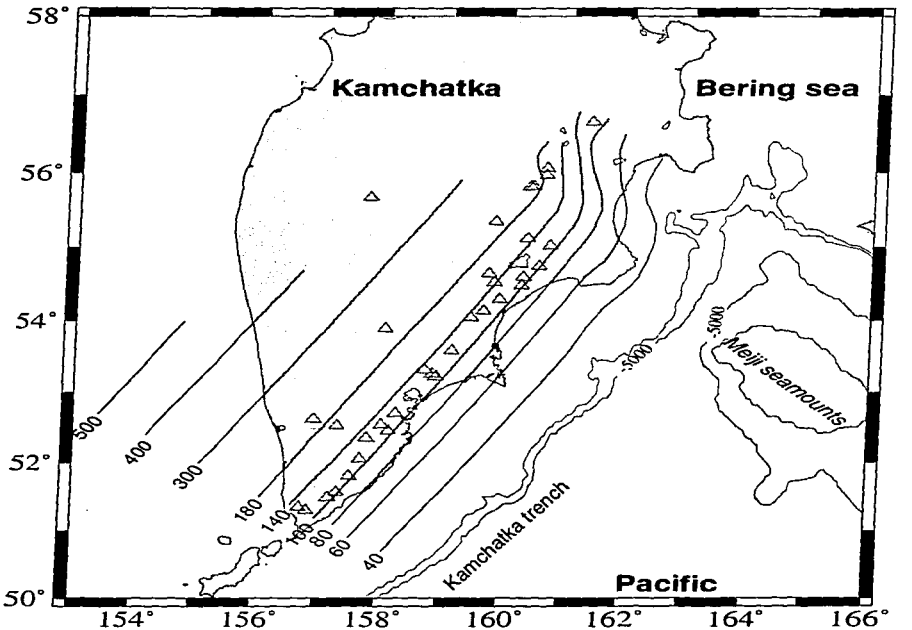
58°
56°
54°
52°
50°
154°
156°
158°
160°
162°
164°
166°
Kamchatka
Bering sea
Pacific
Kamchatka trench
Meiji seamounts
-5000
-5000
500
400
300
180
140
100
80
60
40
0

Figure 5.

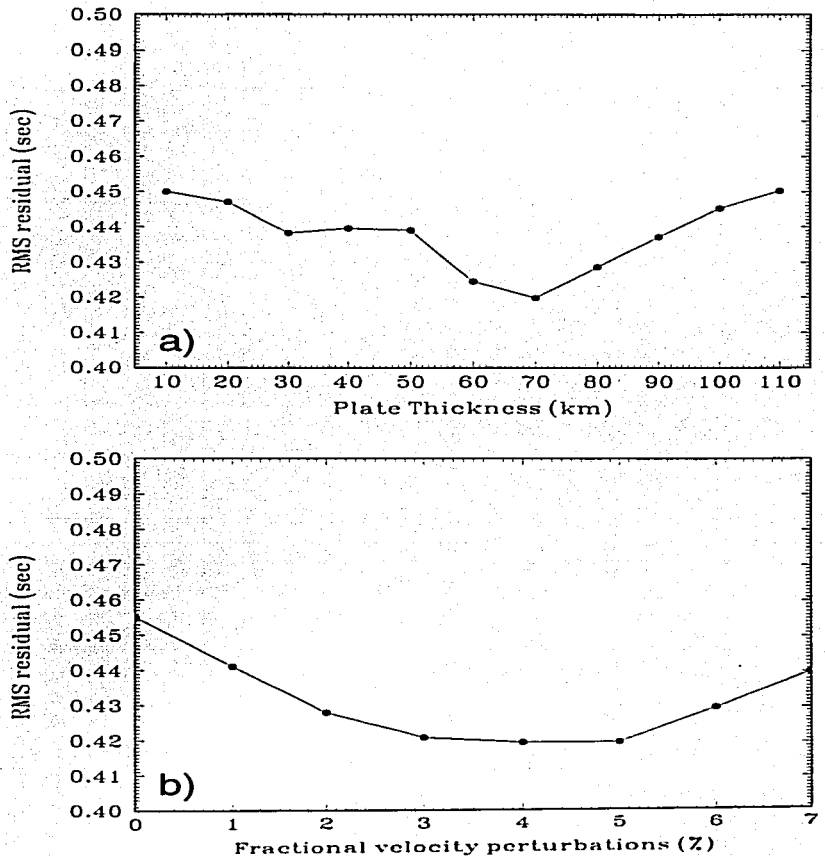
RMS residual (sec)
0.50
0.49
0.48
0.47
0.46
0.45
0.44
0.43
0.42
0.41
0.40
a)
10 20 30 40 50 60 70 80 90 100 110
Plate Thickness (km)
RMS residual (sec)
0.50
0.49
0.48
0.47
0.46
0.45
0.44
0.43
0.42
0.41
0.40
b)
0 1 2 3 4 5 6 7
Fractional velocity perturbations (%)

Figure 6.

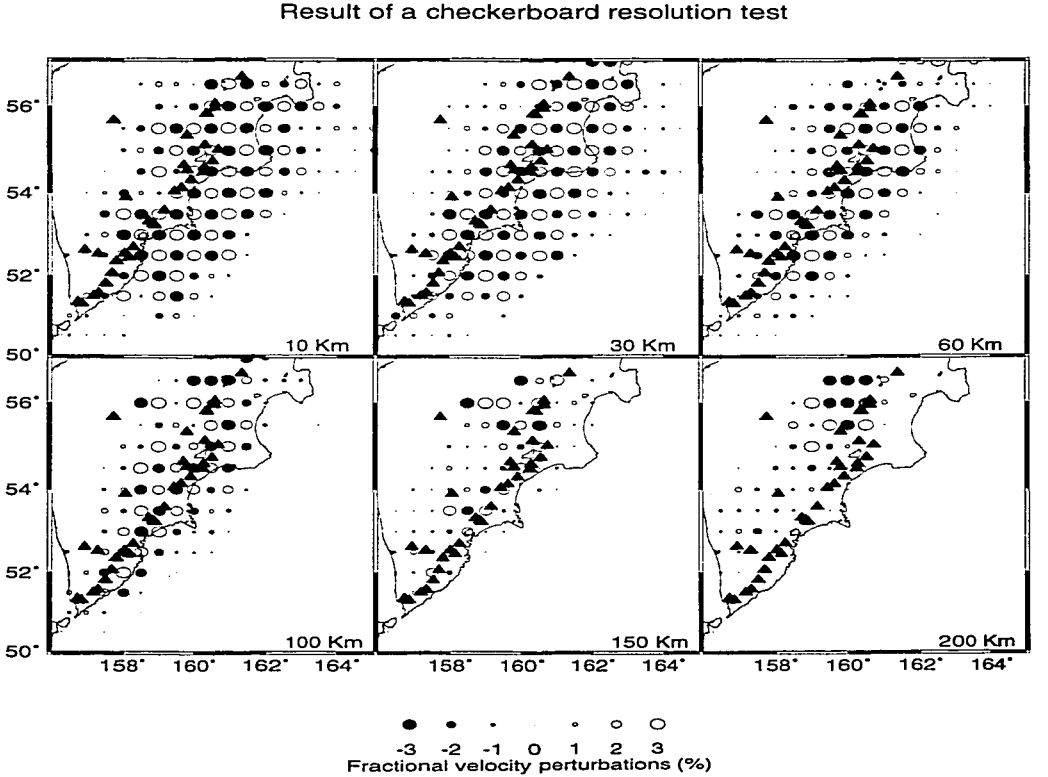
Result of a checkerboard resolution test
56°
54°
52°
50°
10 Km
30 Km
60 Km
100 Km
150 Km
200 Km
158°
160°
162°
164°
-3 -2 -1 0 1 2 3
Fractional velocity perturbations (%)

Figure 7.

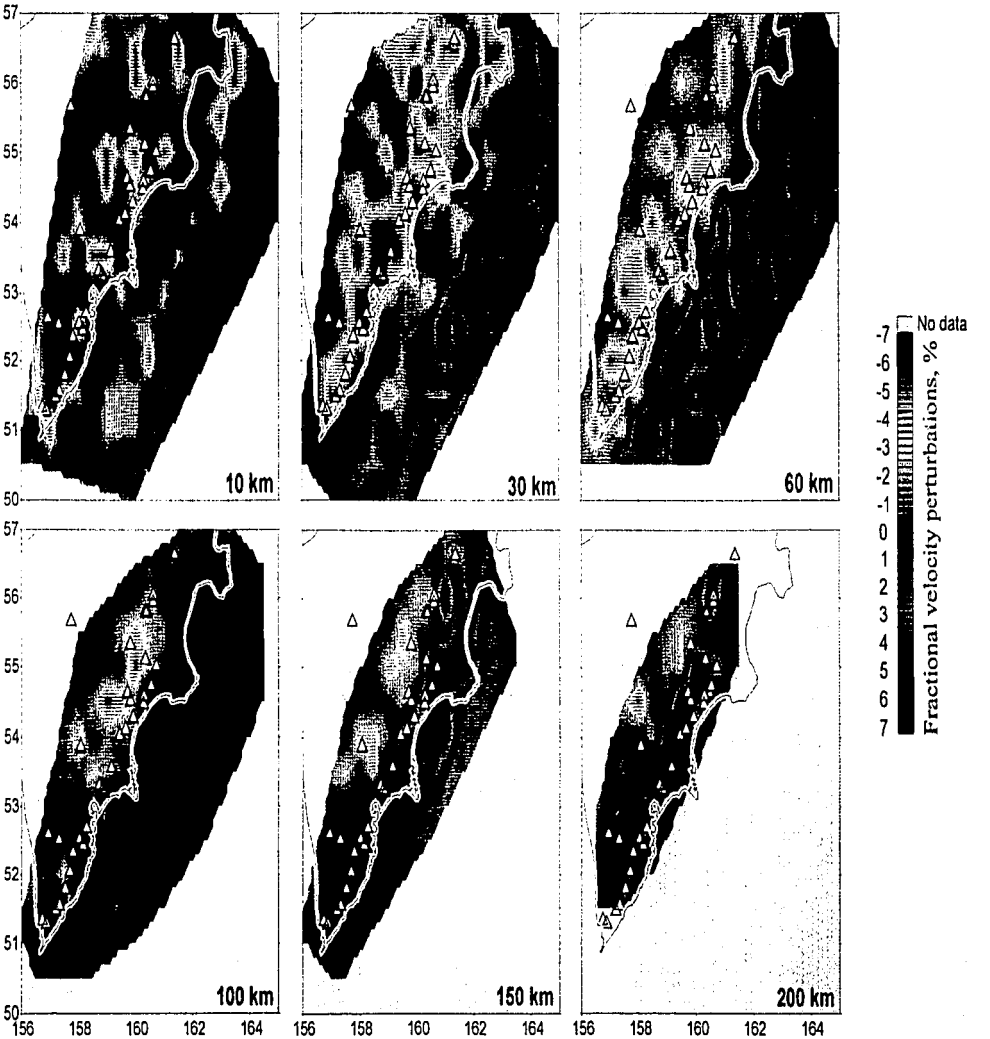
10 km
30 km
60 km
100 km
150 km
200 km
No data
Fractional velocity perturbations, %
-7
-6
-5
-4
-3
-2
-1
0
1
2
3
4
5
6
7
57
56
55
54
53
52
51
50
156
158
160
162
164

Figure 8.

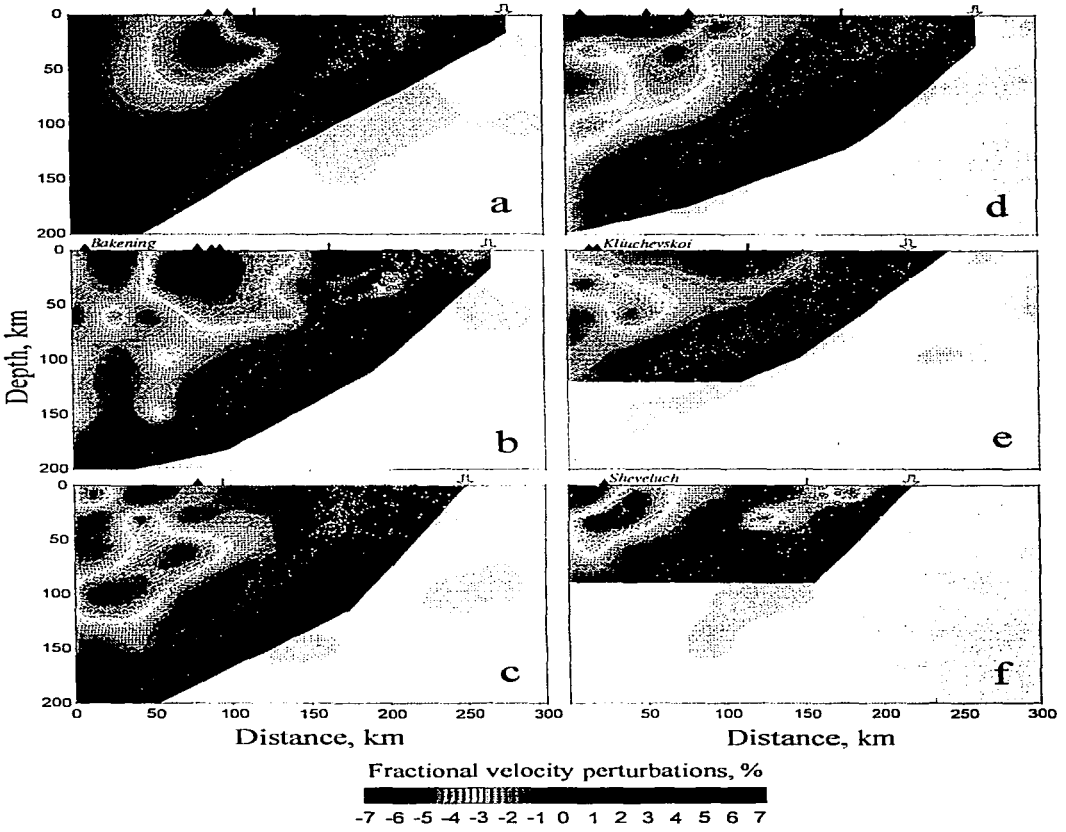
Bakening
Klüchevskoi
Shiveluch
a
b
c
d
e
f
Depth, km
0
50
100
150
200
0
50
100
150
200
250
300
Distance, km
Distance, km
Fractional velocity perturbations, %
-7 -6 -5 -4 -3 -2 -1 0 1 2 3 4 5 6 7

Figure 9.

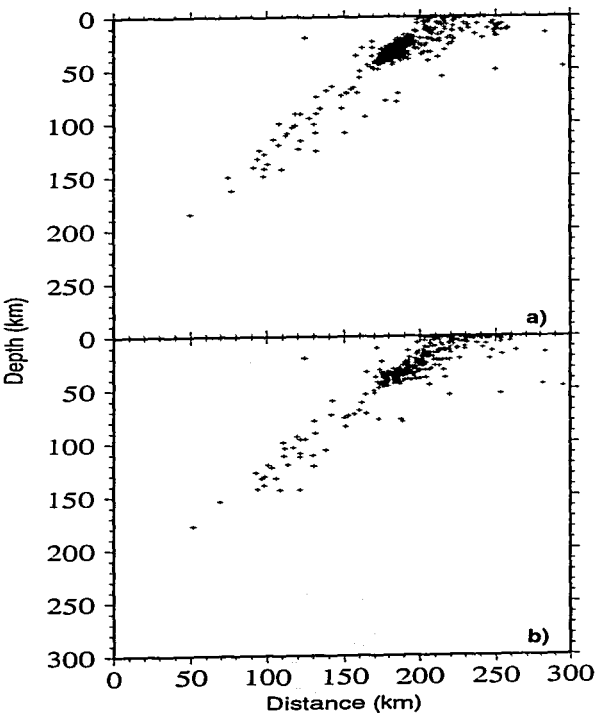
0
50
100
150
200
250
0
50
100
150
200
250
300
Depth (km)
a)
b)
0
50
100
150
200
250
300
Distance (km)

Figure 10.

VI. Conclusiones

Las características de la subducción de la placa del Pacifico bajo la placa Norteamericana en la zona de la península Kamchatka han sido estudiadas utilizando los datos registrados por las redes regionales y telesísmicas. Las principales conclusiones de este estudio son las siguientes:

El ángulo de subducción es de ~55° en la parte sur de ZSK entre ~50°N y ~55°N. Al norte de ~55°N, la placa se deforma en una zona de ~30 km de ancho y el ángulo de subducción disminuye drásticamente a ~35°.

Los mecanismos focales y la distribución de la sismicidad en la zona de deformación sugieren que la contorsión de la placa puede ocurrir por una falla de tipo tijera.

La profundidad máxima de la sismicidad, D_m, varia de ~500 km (~50°N) a ~300 km (~55°N). Al norte de la zona de deformación, D_m disminuye a solo ~100 km de profundidad.

El frente volcánico corresponde con la línea de isoprofundidad de ~90-140 km de la placa subducida. El frente volcánico es lineal en la parte principal de ZSK y en la parte norte se desvía abruptamente hacia el noroeste siguiendo las líneas de isoprofundidad de ~90-140 de la placa subducida. Por lo anterior, los volcanes Sheveluch y probablemente Klychevskoy, ubicados en la parte norte, pertenecen al frente volcánico.

La distribución de la sismicidad y la orientación de los mecanismos focales indican la presencia de una zona sísmica doble entre ~50°N y ~55°N, la cual se extiende probablemente hasta ~56°N. La separación de los planos es de ~50 km a una profundidad de ~50 km y de ~20 km a una profundidad de ~180 km. Los mecanismos focales localizados en la parte superior de la zona sísmica doble cambian su orientación de tipo cabalgadura al de compresión a lo largo de la placa subducida a una profundidad de ~60 km. Esto marca probablemente la profundidad máxima de la zona del contacto seismogénico entre las placas.

La relación empírica general $D_m=f(\varphi)$, obtenida mediante la recopilación de los parámetros de subducción de numerosas zonas de subducción de todo el mundo, permite usarla como una curva estándar para estudiar la relación entre los parámetros de subducción en la zona de Kamchatka.

El cambio de D_m (de ~50°N a ~55°N) en ZSK es consistente con la relación empírica general. Al norte de ~55°N, D_m tiene una profundidad anormalmente somera que interpreta como una disminución de entre dos o tres veces del espesor térmico de la placa subducida en esta área.

La subducción de los montes marinos Meiji provocan aparentemente un impacto significativo en el régimen de subducción de la placa del Pacifico. Debido a ello, la placa oceánica se deforma en la parte norte de ZSK con una consecuente disminución de D_m y del ángulo de subducción.

La imagen tomográfica en tres dimensiones muestra una zona inclinada de alta velocidad, que está probablemente asociada con la placa subducida del Pacífico. El ajuste de los parámetros iniciales sugieren que el ancho de la placa es de ~70 km y la velocidad de la onda P es 7% mayor que en el manto superior.

La perturbación mínima absoluta (~-6%) de la onda P se encuentra bajo el frente volcánico a una profundidad de ~30 km. Esta anomalía forma una banda continua que es lineal en la parte principal de ZSK y se desvía hacia al noroeste en la parte norte siguiendo el frente volcánico. Esta anomalía se relaciona aparentemente con la presencia de magma inmediatamente bajo el arco volcánico.

Las anomalías de baja velocidad se observan hasta una profundidad de ~150-200 km debajo de los volcanes y se asocian con la generación de magma.

Los resultados de la inversión tomográfica se correlacionan bien con la geología superficial de la península de Kamchatka. Las zonas de baja velocidad coinciden especialmente con el prisma de acreción y los depósitos de material sedimentario en el graben central de Kamchatka. Las zonas de alta velocidad se correlacionan con los levantamiento Ganalsky-Valaginskoe constituidos por rocas metamórficas y el levantamiento de rocas del basamento de la península Shipunsky. Las zonas de alta velocidad cerca de los volcanes probablemente se correlacionan con cuerpos intrusivos.